

Effect of Inlet Swirl on Flow Separation in Diffuser

A Thesis submitted to

Delhi Technological University

For the Award of the Degree of

Doctor of Philosophy

In

Mechanical Engineering

By

Hardial Singh

(2K16/PhD/ME/38)

Under the Supervision of

Prof. B.B. Arora

Professor, Department of Mechanical Engineering



DEPARTMENT OF MECHANICAL ENGINEERING

Delhi Technological University

(Formerly Delhi College of Engineering)

Delhi-110042, India

October 2021

Dedicated to

My Parents

My Wife, Satwinder Kaur

My Daughter, Hargun Kaur

and

My Son, Nishan Singh

Declaration

I hereby declare that the thesis entitled “**Effect of Inlet Swirl on flow separation in Diffuser**” is an original work carried out by me under the supervision of Prof. B. B. Arora, Professor, Department of Mechanical Engineering, Delhi Technological University, Delhi. This thesis has been prepared in conformity with the rules and regulations of Delhi Technological University, Delhi. The research work reported and results presented in the thesis have not been submitted either in part or full to any other university or institute for the award of any other degree or diploma.

Hardial Singh

Reg. No. 2K16/PhD/ME/38

Department of Mechanical Engineering

Delhi Technological University

Delhi – 110042, India.

Certificate

This is to certify that the thesis entitled “**Effect of Inlet Swirl on flow separation in Diffuser**” being submitted by **Hardial Singh (Roll No. 2K16/PhD/ME/38)** to the Delhi Technological University Delhi for the award of the degree of **Doctor of Philosophy**, is a record of the bonafide research carried out by him which has been prepared under my supervision in conformity with the rules and regulations of the Delhi Technological University, Delhi. The research reports and results presented in the thesis have not been submitted for any degree or diploma at any other university or institute.

Prof. B. B. Arora

Professor

Department of Mechanical Engineering

Delhi Technological University

Delhi – 110042, India.

Acknowledgements

It is my great pleasure to record profound gratitude to my research supervisor, Prof. B.B. Arora, Professor, Department of Mechanical Engineering, Delhi Technological University, Delhi, for his constant inspiration and invaluable guidance throughout this research. His vast knowledge and research expertise have helped me to understand, appreciate, evolve, and gain deeper insights into my topic. The long and regular discussions helped me to get a better idea of the current research, which is the real reason for the present work outcome. I gratefully acknowledge his painstaking efforts in thoroughly going through and improving the manuscript, without which this work would not have been completed. Further, throughout my tenure, he has regularly emphasized and helped me become an independent researcher along with a good human being. The numerous discussions I had with Dr. A.K Raghava always helped me to remove the ambiguities and brought a sense of clarity to my work.

I am grateful to Dr. S. K. Garg, Head and DRC chairman, Department of Mechanical Engineering, Delhi Technological University, Delhi, for their administrative support during the execution and completion of this thesis. Thanks are also due to Prof. Vipin, Dr. Akhilesh Arora, and all the staff members for their kind cooperation.

I extend special gratitude to all the esteemed seniors as well as other colleagues in my department, who were so easily approachable, helpful, and a source of encouragement during this span of work. I am thankful to all the close friends and relatives, especially Omprakash, Ashutosh, Dr. Gopal Krishan, Dr. Prakahar Jindal, and Dr. S.B. Gupta, whose never-ending support and wholehearted help were the real impetus that continuously motivated me to do my best.

My gratefulness, hearty and special measure of thanks is due to my wife, Satwinder Kaur, for her patience, love, encouragement during this course of work, and my daughter Hargun Kaur and son Nishan Singh, just for being themselves. I also express deep gratitude to my parents for their moral support. Finally, I owe all of my academic achievements to my parents, who have tremendously encouraged me throughout my academic career as well as my whole life.

(Hardial Singh)

Abstract

The diffuser is a critical component of turbomachinery, such as the inlet portion of jet engines, gas turbines, axial compressors, etc. The annular diffuser is employed to efficiently convert kinetic energy into pressure energy within the shortest possible length. When the fluid passes through the diffuser, it is retarded, and diffusion comes into the picture. The diffusion process in the diffuser is very complex. There is a chance of developing an unfavorable adverse pressure gradient that may lead to flow separation due to severe loss of the gas turbine performance. A good diffuser design increases the efficiency of the power plant and minimizes the requirement for fuel, which leads to the benefit of society. The performance of an annular diffuser depends upon a large number of geometrical and dynamical parameters. Despite knowing the importance of an annular diffuser for turbomachinery, the literature present in the open forum is scanty due to the confidential nature of the application. Based on the available literature survey, the effect of inlet swirl on the performance of an annular diffuser has been studied. In addition, the effect of geometrical parameters has also been reported. The emphasis of the current work is to systematically investigate the various geometrical configurations such that higher performance can be achieved.

In the present research work, experimental and numerical investigations have been carried out to study the effect of fully developed swirling and non-swirling flow to characterize the flow behavior and performance of the annular diffuser. The geometric design of the annular diffuser is calculated on different area ratios (i.e. 2 to 4) and varying casing angles. The flow conditions at the inlet are varied with different inlet swirl angles (0° - 25°) to evaluate the effect of flow development inside the diffuser. The flow behavior of the annular diffuser is analyzed at Reynolds number 2.5×10^5 .

The performance characteristics are assessed based on longitudinal velocity profiles, swirl velocity profiles, static pressure recovery coefficient, total pressure loss coefficient, and effectiveness. The velocity profiles were measured at several locations along the length of the diffusers.

The numerical investigations were carried out using Fluent, a commercial Computational Fluid Dynamics code. The obtained simulated outcomes using steady-state Reynolds-averaged Navier-Stokes equations with a two-equation turbulence model were validated with the experimental data. The RNG $k-\epsilon$ model was used to capture the turbulence effects. The obtained results are analyzed, and it reveals that at a lower swirl angle, the separation is near the casing, whereas at a higher swirl, the point of separation shifts towards the hub side. Further, the introduction of adequate swirl intensity at the inlet is found to provide a substantial improvement in static pressure at the casing wall. The point of flow separation tends to shift away from the casing wall and can be completely vanished with a high degree of inlet swirl. However, it may appear at the hub. The maximum static pressure recovery coefficient and minimum total pressure loss coefficient are observed at the optimum value of the inlet swirl angle.

Table of Contents

Declaration	i
Certificate	ii
Acknowledgement	iii
Abstract	v
Table of Contents	vii
List of Figures	xi
List of Tables	xv
Nomenclature	xvi
Chapter-1.....	1
1 Introduction	1
1.1 Axial Diffuser.....	3
1.1.1 Channel Diffuser	3
1.1.2 Conical Diffuser	5
1.1.3 Annular Diffuser	5
1.2 Radial Diffuser	8
1.3 Curved Wall Diffuser	8
1.4 Performance Parameters for an Annular Diffuser	9
1.4.1 Static Pressure Recovery Coefficient (C_p).....	9
1.4.2 Diffuser Effectiveness (η).....	10
1.4.3 Total Pressure Loss Coefficient (C_L).....	10
1.5 Swirl Flow.....	11
1.5.1 Physics of Swirling and Rotating Flows: -	11
1.6 Principle for Diffuser Design	12
1.7 The organization of the Thesis	13
Chapter-2.....	15
2 Literature Review.....	15
2.1 Studies of Geometric Parameters- Passage Divergence, Length and Area Ratio.....	16
2.2 Inlet Velocity Profile and Distortions.....	19
2.3 Inlet Blockage Factor.....	21
2.4 Inlet Reynolds Number and Mach Number	23
2.5 Inlet Turbulence Level.....	25

2.6	Inlet Swirl.....	26
2.7	Analytical and Computational Studies	29
2.8	Gaps in Literature	31
2.9	Motivation.....	31
2.10	Scope of the Present Work.....	32
Chapter -3.....		35
3	Experimental Methodology	35
3.1	Experimental Setup	36
3.2	Geometrical Specification of the Test Diffuser	38
3.3	Swirl Generation Technique and Specification.....	38
3.4	Diffuser Inlet Location	41
3.5	Instrumentation.....	41
3.5.1	Three Hole Cobra Probe	41
3.5.2	Manometers.....	44
3.6	Traversing Mechanism	45
3.7	Initial Conditions	46
3.8	Experimental Procedure.....	47
3.8.1	Static Pressure Measurement on the Wall	47
3.8.2	Velocity Profile Measurement	47
3.8.3	Flow Visualization	48
3.9	Uncertainty in Measurements	49
Chapter-4.....		51
4	Computational and Mathematical Formulation	51
4.1	Mathematical Formulation.....	52
4.2	Turbulence Modelling	54
4.2.1	Standard $k-\varepsilon$ Turbulence Model	55
4.2.2	RNG $K-\varepsilon$ Turbulence Model.....	56
4.2.3	Realizable $k-\varepsilon$ Turbulence Model.....	58
4.2.4	Standard $k-\omega$ Model	59
4.2.5	Shear-Stress Transport (SST) $k-\omega$ Model.....	59
4.3	CFD Analysis Procedure	60
4.3.1	Pre-processor.....	60
4.3.2	Solver.....	64
4.3.3	Post-processor	67
4.4	Procedure of Simulation	68

Chapter-5.....	70
5 Validation	70
5.1 Grid Independence Study.....	70
5.2 Validation of the CFD Methodology.....	72
5.3 Validation of Static Pressure Recovery Coefficient Profile	74
Chapter-6.....	77
6 Computational Investigation: Effects of Casing Angle on the Performance of Parallel Hub Annular Diffusers	77
6.1 Range of Parameters	77
6.2 Parallel Hub Axial Annular Diffuser	78
6.2.1 Turbulence Intensity.....	79
6.2.2 Velocity Vector	80
6.2.3 Velocity Profiles.....	81
6.2.4 Static Pressure Recovery Coefficient	85
6.2.5 Total Pressure Loss Coefficient	88
6.3 Concluding Remarks	88
Chapter-7.....	89
7 Computational Investigation: Effect of Swirl Flow on the Performance of Axial Annular Diffusers	89
7.1 Study of Parallel Hub Diverging Casing Annular Diffuser having Different Equivalent Cone Angle.....	89
7.1.1 Physical Model.....	90
7.1.2 Velocity Vector	91
7.1.3 Velocity Profiles.....	92
7.1.4 Static Pressure Recovery Coefficient	97
7.1.5 Total Pressure Loss Coefficient	100
7.1.6 Effectiveness	101
7.2 Inlet Swirl Optimization for Flow Separation in PHDC Annular Diffuser	102
7.2.1 Streamline Contours	103
7.2.2 Velocity Profiles.....	104
7.2.3 Static Pressure Recovery Coefficient	106
7.3 Effect of Swirling Flow on the Characteristics of the UHDC Annular Diffuser	106
7.3.1 Velocity Distribution Analysis.....	107
7.3.2 Static Pressure Recovery Coefficient	109
7.4 Concluding Remarks	110

Chapter-8.....	112
8 Computational investigation: Performance Characteristics of Flow in Annular Diffusers	112
8.1 Computational Domain.....	112
8.2 Computational Analysis of Different Types of Annular Diffuser.....	112
8.2.1 Streamline Traces over Velocity Contours.....	114
8.2.2 Velocity profiles.....	116
8.2.3 Static Pressure Recovery Coefficient	119
8.2.4 Total Pressure Loss Coefficient	121
8.3 Concluding Remarks	122
Chapter-9.....	124
9 Conclusion and Scope for Future Work.....	124
9.1 Conclusion	124
9.2 Scope for Future Work	126
Bibliography.....	128

List of Figures

Figure 1.1: Planer diffuser (Source: Applied Fluid Dynamics Handbook by R.D. Blevins (1984)).	4
Figure 1.2: Conical diffuser (Source: Applied Fluid Dynamics Handbook by R.D. Blevins (1984)).	5
Figure 1.3: Annular diffuser (Source: Applied Fluid Dynamics Handbook by R.D. Blevins (1984)).	6
Figure 1.4: Geometrical design of annular diffusers.	7
Figure 1.5: Vanned diffuser (Source: Applied Fluid Dynamics Handbook by R.D. Blevins (1984)).	8
Figure 1.6: Curved diffuser (Source: Chong et al. (2008)).	9
Figure 1.7: Free vortex flow of ω in the radial direction (Source: <i>Fluent</i> user's guide (2014)).	11
Figure 2.1: Frequency of articles on the diffusers.	16
Figure 2.2: Relationship between diffuser effectiveness and cone angle.	17
Figure 2.3: C_p with area ratio (Kumar & Kumar (1980)).	18
Figure 2.4: Graph plotted between diffuser effectiveness and area ratio (Japikse, 2002).	21
Figure 2.5: Static pressure recovery with Mach number (Dean & Runstadler (1969)).	23
Figure 2.6: Static pressure recovery with Reynolds number (Mcmillan & Johnston (1973)).	24
Figure 2.7: C_p with inlet swirl angle of the annular diffusers (Japikse, 2002).	27
Figure 3.1: Actual experimental setup of the diffuser.	37
Figure 3.2: Centrifugal blower used for the experimental setup.	37
Figure 3.3: (i) Schematic of experimental test rig; (ii) location of actual measuring stations.	38
Figure 3.4: Traversing mechanism for the experimental setup.	46
Figure 3.5: Inlet velocity profiles with an equivalent cone angle of 15° , AR = 2.	48
Figure 4.1: The annular diffuser's two-dimensional geometry.	61
Figure 4.2: Near wall region (Source: ANSYS Academic Research <i>Fluent</i> (Release 15.0)).	62
Figure 4.3: Meshed computational domain.	63
Figure 4.4: 2D axisymmetric annular diffuser.	64
Figure 4.5: Iteration process for a convergence.	67

Figure 5.1: Grid refinement study of the longitudinal velocity profile with an inlet swirl angle of 0° at $x/L = 0.3$ for PHDC diffuser equivalent cone angle of 15° and $AR = 2$	71
Figure 5.2: (i-v) Comparison of longitudinal velocity profiles with experimental results along the passage ($x/L = 0.3, 0.5, 0.7,$ and 0.9) for the PHDC diffuser with an equivalent cone angle of 15° at an inlet swirl angle of 0° ($AR = 2$)... 73	73
Figure 5.3: (i-v) Comparison of longitudinal velocity profiles with experimental results along the passage ($x/L = 0.3, 0.5, 0.7,$ and 0.9) for the PHDC diffuser with an equivalent cone angle of 15° at an inlet swirl angle of 12° ($AR = 2$).. 74	74
Figure 5.4: (i-v) Comparison of swirl velocity profiles with experimental results along the passage ($x/L = 0.3, 0.5, 0.7,$ and 0.9) for the PHDC diffuser with an equivalent cone angle of 15° at an inlet swirl angle of 12° ($AR = 2$)..... 75	75
Figure 5.5: comparison of different turbulence models with experimental data of static pressure recovery coefficient at the casing wall of the PHDC diffuser with a cone angle of 15° at an inlet swirl angle of 12° ($AR = 2$)..... 76	76
Figure 6.1: Design of an annular diffuser with its components. 78	78
Figure 6.2: Turbulence intensity at the inlet. 79	79
Figure 6.3: (i-ix) Velocity vector contours of diffusers A, B, and C at swirl angles of $0^\circ, 12^\circ,$ and 25° 80	80
Figure 6.4: (i-ii) Longitudinal velocity distribution of diffuser A at 0° and 12° swirl angles; (iii) Swirl velocity distribution of diffuser A at a 12° swirl angle. 82	82
Figure 6.5: (i) Longitudinal velocity distribution of diffuser A at a 25° swirl angle; (ii) Swirl velocity distribution of diffuser A at a 25° swirl angle..... 82	82
Figure 6.6: (i-ii) Longitudinal velocity distribution of diffuser B at 0° and 12° swirl angles; (iii) Swirl velocity distribution of diffuser B at a 12° swirl angle. 83	83
Figure 6.7: (i) Longitudinal velocity distribution of diffuser B at a 25° swirl angle; (ii) Swirl velocity distribution of diffuser B at a 25° swirl angle. 83	83
Figure 6.8: (i-ii) Longitudinal velocity distribution of diffuser C at 0° and 12° swirl angles; (iii) Swirl velocity distribution of diffuser C at a 12° swirl angle. 84	84
Figure 6.9: (i) Longitudinal velocity distribution of diffuser C at a 25° swirl angle; (ii) Swirl velocity distribution of diffuser C at a 25° swirl angle. 84	84
Figure 6.10: (i) Static pressure recovery coefficient (C_p) at the casing of diffuser A; (ii) Total pressure loss coefficient (C_L) of diffuser A. 86	86
Figure 6.11: (i) Static pressure recovery coefficient (C_p) at the casing of diffuser B; (ii) Total pressure loss coefficient (C_L) of diffuser B. 86	86
Figure 6.12: (i) Static pressure recovery coefficient (C_p) at the casing of diffuser C; (ii) Total pressure loss coefficient (C_L) of diffuser C. 86	86
Figure 6.13: (i) C_p with the area ratio of diffusers A, B, and C; (ii) C_p with the non-dimensional length of diffusers A, B, and C. 87	87

Figure 7.1: Geometrical design of the annular diffuser.....	91
Figure 7.2: (i-ix) Velocity vector contours at swirl angles of 0°, 12°, and 25° for the equivalent cone angles of 10°, 15°, and 20°.....	92
Figure 7.3: (i-iii) Longitudinal velocity distribution at inlet swirl angles of 0°, 12°, and 25° for an equivalent cone angle of 10°.....	93
Figure 7.4: (i-ii) Swirl velocity distribution at inlet swirl angles of 12° and 25° for an equivalent cone angle of 10°.....	94
Figure 7.5: (i-iii) Longitudinal velocity distribution at inlet swirl angles of 0°, 12°, and 25° for an equivalent cone angle of 15°.....	95
Figure 7.6: (i-ii) Swirl velocity distribution at inlet swirl angles of 12° and 25° for an equivalent cone angle of 15°.....	95
Figure 7.7: (i-iii) Longitudinal velocity distribution at inlet swirl angles of 0°, 12°, and 25° for an equivalent cone angle of 20°.....	96
Figure 7.8: (i-ii) Swirl velocity distribution at inlet swirl angles of 12° and 25° for an equivalent cone angle of 20°.....	96
Figure 7.9: (i) Static pressure recovery coefficient at the casing wall with a cone angle of 10°; (ii) Total pressure loss coefficient with a cone angle of 10°.....	99
Figure 7.10: (i) Static pressure recovery coefficient at the casing wall with a cone angle of 15°; (ii) Total pressure loss coefficient with a cone angle of 15°.....	99
Figure 7.11: (i) Static pressure recovery coefficient at the casing wall with a cone angle of 20°; (ii) Total pressure loss coefficient with a cone angle of 20°.....	100
Figure 7.12: (i) Static pressure coefficient at the exit with inlet swirl of diffusers A, B, and C; (ii) Static pressure recovery coefficient (C_p) with the variation of the area ratio of diffusers A, B, and C along the length.....	101
Figure 7.13: (i) Effectiveness with inlet swirl of diffuser A, B, and C; (ii) Total pressure loss coefficient with inlet swirl of diffuser A, B, and C.....	101
Figure 7.14: Streamline contours for the two-dimensional axisymmetric annular diffuser with and without swirl flow.....	103
Figure 7.15: Longitudinal velocity distributions of an equivalent cone angle of 15° with inlet swirl angles (7.5°-25°).....	104
Figure 7.16: Swirl velocity distributions of an equivalent cone angle of 15° with inlet swirl angles (7.5°-25°).	105
Figure 7.17: Static pressure recovery coefficient at the casing wall with an equivalent cone angle of 15°.....	106
Figure 7.18: Streamline contours of UHDC diffuser at inlet swirl angles (i) 0°, (ii) 7.5°, (iii) 12°, (iv) 17°, and (v) 25°.....	107
Figure 7.19: Longitudinal velocity profiles at the different axial locations of UHDC diffuser (i) Swirl angle 0°; (ii) Swirl angle 12°; (iii) Swirl angle 25°....	108

Figure 7.20: Swirl velocity profiles at the different axial locations of UHDC diffuser (i) Swirl angle 12°; (ii) Swirl angle 25°	108
Figure 7.21: Static pressure recovery coefficient at the casing wall of the UHDC diffuser.....	109
Figure 8.1: Geometrical configuration of the annular diffuser.	113
Figure 8.2: Geometrical designs of annular diffusers.....	114
Figure 8.3: Streamline traces over velocity contours for different diffusers at inlet swirl angles (i) 12° and (ii) 25°	115
Figure 8.4: (i) Longitudinal velocity profiles at the exit of EHDC and UHDC diffusers; (ii) swirl velocity profiles at the exit of EHDC and UHDC diffusers....	117
Figure 8.5: (i) Longitudinal velocity profiles at the exit of PHDC and CHDC diffusers; (ii) swirl velocity profiles at the exit of PHDC and CHDC diffusers. ...	118
Figure 8.6: Pressure recovery coefficient at the casing wall of EHDC, UHDC, PHDC, and CHDC diffusers.....	120
Figure 8.7: Total pressure loss coefficient of the EHDC, UHDC, PHDC, and CHDC diffusers.	122

List of Tables

Table 3.1: Geometrical parameters of the PHDC annular diffuser with an equivalent cone angle of 15° , $AR = 2$	38
Table 3.2: Uncertainties associated with measurement	50
Table 6.1: Geometrical parameters of the annular diffuser.	78
Table 7.1: Geometrical parameters of straight hub axial annular diffusers.	90
Table 7.2: Value of the geometric parameters of the annular diffuser.	102
Table 7.3: Geometrical dimensions of the Unequal Hub and Diverging Casing (UHDC) annular diffuser.	107
Table 8.1: Geometrical specifications of annular diffusers.	113

Nomenclature

Notations

C_p	static pressure recovery coefficient
C_L	total pressure loss coefficient
η	effectiveness
S	swirl number
B	blockage factor
T_u	turbulence intensity
Re	Reynolds number
R	hydraulic radius
u	longitudinal velocity
w	swirl velocity
φ	yaw angle
Θ	divergence angle
y	transverse distance from the hub surface
Y_m	maximum transverse distance from the hub surface
R_h	hub radius
R_c	casing radius
Θ_e	equivalent cone angle
L	axial length
ΔR	diffuser height
x/L	non-dimensional axial length
y/Y_m	non-dimensional radial length
F	force

ρ	density
S_m	mass added to continuous phase
k	turbulent kinetic energy
ε	turbulent dissipation energy
ω	specific dissipation rate
μ	molecular viscosity
μ_t	turbulent viscosity
u_T	wall shear stress
y^+	dimensionless distance of the first cell height from the wall

Subscripts

c	casing
h	hub
i	inlet
o	outlet
e	equivalent
x	axial
r	radial
z	tangential or swirl

Abbreviation

AR	area ratio
CFD	computational fluid dynamics
RANS	Reynolds-Averaged Navier-Stokes
SIMPLE	semi-implicit method for pressure linked equation
EHDC	equal hub and diverging casing
UHDC	unequal hub and diverging casing

PHDC parallel hub and diverging casing
CHDC convergent hub and diverging casing

Chapter-1

1 Introduction

The diffuser is an expanding cross-section that recovers the fluid's highest possible static pressure by reducing its flow velocity. The flow is decelerated when it passes across the diffuser, as part of the fluid's kinetic energy, is converted into an increase in static pressure due to diffusing action. The effective diffuser changes maximum kinetic energy into pressure energy in the shortest distance. The annular diffuser's primary function is to achieve maximum pressure recovery and uniform fluid flow at the outlet.

The formation of eddies near the wall as the boundary layer develops and its thickness increases rapidly, resulting in flow obstruction. The fluid flow is decelerated because of the adverse pressure gradient on the surfaces. The flow separation from the surfaces is known as stall, and its presence always reduces the static pressure rise. Therefore, the diffuser's performance depends upon the boundary layer development and shape of the stall. When the wall angle is very large, eddies form in the flow and there is less energy conversion from kinetic energy into pressure energy. Diffuser length increases when the cone angle is small. Skin friction on the walls causes the reduction in static pressure rise in the long diffuser (Kumar et al. 2011, 2012).

Diffusers are important components in numerous fluid handling systems, for example, inlet portions of jet engines, gas turbines, ramjets, power plants, centrifugal compressors, axial flow compressors, combustion chambers, wind tunnels, noise suppressors, carburetors, and flow meters, etc.

The diffuser flow is characterized by irregularities in the flow pattern, non-uniform velocity distribution, unstableness, total pressure loss, and separation zone due to the boundary layer development from the surfaces. The experimental observation

optimizes the static pressure rise; it helps to remove unnecessary effects. The diffuser performance is enhanced by experimental studies with the help of the empirical relationships derived from analytical studies. The transformation of the kinetic energy into static pressure rises at a significant level in the turbomachine is to accomplish the power plant's intended needs (Kumar et al. 2011). The efficiency of the system improved significantly with a small change in pressure recovery. Therefore, it is concluded that the diffuser is an essential part of the good performance of turbomachinery.

Annular diffuser performance depends upon numerous geometric and dynamic parameters. The geometric parameters that govern a diffuser's performance, i.e., area ratio, divergence angle, inlet length, aspect ratio, axial length, the duct's shape, and the duct's size, etc. The dynamic parameters such as inlet velocity distribution, Reynolds number, boundary layer parameters, and Mach number, etc. It has been found that the flow in the diffusers depends upon the geometrical parameters, i.e., inlet and outlet. The geometry of the annular diffuser is defined by the wall angle, area ratio, non-dimensional length, and inlet radius ratio.

The effective diffuser is that which changes maximum pressure energy from kinetic energy. In the gas turbine, the central core shaft is required, and the necessity is fulfilled by the annular diffuser. Annular diffusers are commonly used in conjunction with turbomachine systems such as turbines, pumps, and compressors, etc. The annular diffuser is located downstream of the compressor in aircraft applications. In turbomachinery, the diffuser operates under the existence of swirl flow. Guide vanes and struts generate the swirling flow. It is also created by fluid flow around the central shaft and bearing, passing through the diffuser and compressor. The swirl effect changes the flow velocity because the performance of the system is improved (Arora,

2014; Singh & Arora, 2019). Many researchers evaluate swirl flow through the diffuser in terms of flow behavior. The swirling flow improves the diffuser's effectiveness. The swirl flow plays a significant role in controlling the reversal flow in the diffuser (Goebel & Japikse, 1981). Total pressure loss was reduced in the combustor by using an effective annular diffuser. The geometry of the annular diffuser is known to be very complex due to the presence of an inner wall that guides the flow in an outward direction.

The experimental method for evaluating annular diffuser performance is tedious and time-consuming due to the complexity of the parameters. If we change the parameters, then the setup will be reformed. So, evaluation of the performance of annular diffusers through experimentation is not reasonable. Therefore, the computational fluid dynamics methodology is adopted to examine the analysis of diffusers.

1.1 Axial Diffuser

The flow of fluid is parallel to the axis and along the axial diffuser direction, and there is incessant retardation of the flow. The axial diffuser is classified into the following categories:

- (i). Channel diffuser
- (ii). Conical diffuser
- (iii). Annular diffuser

1.1.1 Channel Diffuser

The two-dimensional diffuser can be specified by its parameters. In this type of diffuser, width is changed by the respective change in area ratio (AR). Its axial length and width

ratio, N/W_1 , and either included angle 2θ or area ratio A_2/A_1 as shown in Figure 1.1.

From the geometry of the diffuser, it can be shown that (Equation 1.1):

$$\tan \theta = \frac{W_2 - W_1}{2N} = \frac{W_1}{2N} \left(\frac{W_2}{W_1} - 1 \right) = \frac{W_1}{2N} \left(\frac{A_2}{A_1} - 1 \right) \quad (1.1)$$

Where: -

- W_1 = Inlet Width
- W_2 = Outlet Width
- N = Diffuser Length

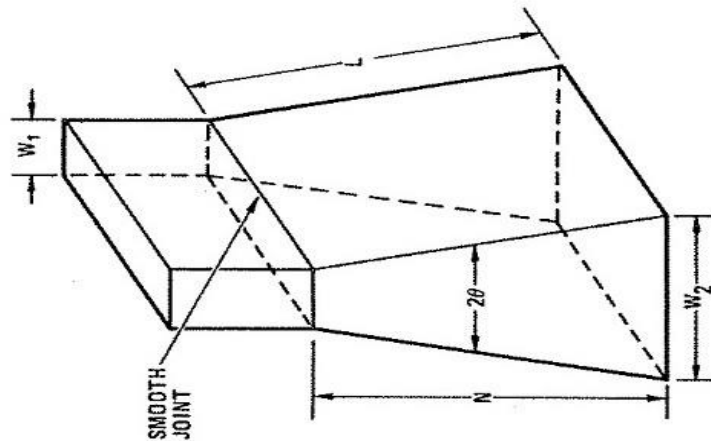


Figure 1.1: Planer diffuser (Source: Applied Fluid Dynamics Handbook by R.D. Blevins (1984)).

This indicates that optimized two-dimensional diffusers will be marginally stable. The stability of a two-dimensional diffuser can be obtained only at the cost of a performance penalty by either

1. Decreasing the diffuser angle or area ratio to place the diffuser well within the range of no appreciable stall
2. Increasing diffuser angle or area ratio to the point where the diffuser lies well within the fixed stall or jet flow regime
3. Vaning the diffuser.

The first and third options require the smallest performance penalty.

1.1.2 Conical Diffuser

This type of diffuser is shaped like a cone (Figure 1.2). It provides a likely efficient improvement in a centrifugal compressor (Equation 1.2).

$$\tan \theta = \frac{R_2 - R_1}{N} = \frac{R_1}{N} \left(\frac{R_2}{R_1} - 1 \right) = \frac{R_1}{N} \left[\left(\frac{A_2}{A_1} \right)^{1/2} - 1 \right] \quad (1.2)$$

Where: -

- R_1 = Inlet Radius
- R_2 = Outlet Radius
- N = Length of Diffuser

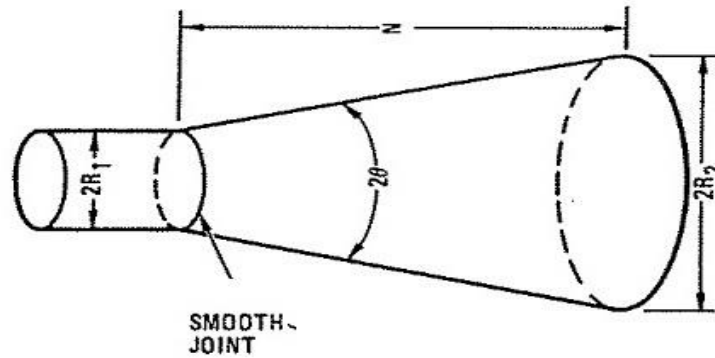


Figure 1.2: Conical diffuser (Source: Applied Fluid Dynamics Handbook by R.D. Blevins (1984)).

1.1.3 Annular Diffuser

This type of diffuser is shaped like a ring. The non-dimensional diffuser length and radius $\bar{L}/\Delta R_1$ as shown in Figure 1.3. The standard diffuser wall length and the inlet differential radius are described as (Equations 1.3-1.4):

$$\bar{L} = \frac{(L_i + L_o)}{2} \quad (1.3)$$

$$\Delta R_1 = R_o - R_i \quad (1.4)$$

$$\text{Area ratio (AR)} = A_2/A_1$$

Common annular diffusers have wall angles in the 5° to 30° range and radius ratios of R_i/R_o between 0.55 and 0.70. These two parameters correlate with the majority of experimental data.

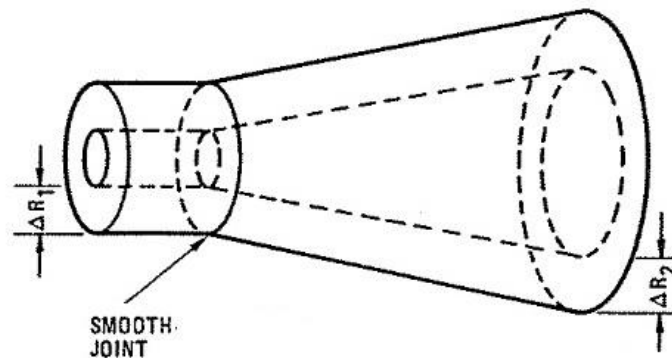


Figure 1.3: Annular diffuser (Source: Applied Fluid Dynamics Handbook by R.D. Blevins (1984)).

For decades, researchers have paid more attention to the conical diffuser and channel diffuser than to annular diffusers. The practical application of the annular diffuser is in turbomachinery, which has become more prevalent in recent times. Such types of diffusers are widely used in aircraft applications. The maximum performance is achieved with the annular diffuser having a shorter length. The different geometric combination of wall angles in the annular diffuser has been maintained to attain the maximum performance as per requirement. The large outer wall angle can also be used and obtain good performance since the inner wall angle moves the flow radially in the outside direction. The annular diffuser affords the probability of various types of geometrical configurations. There is an inside wall that may be set independently of the outside wall.

It is very tedious to explain the specification of the annular diffuser with various geometric parameters. The important parameters to explain the annular diffuser's geometry are cone angle, area ratio, axial length, and inlet radius ratio. The geometry becomes more complex as the geometric variables increase. The geometrical design of the annular diffusers is depicted in Figure 1.4.

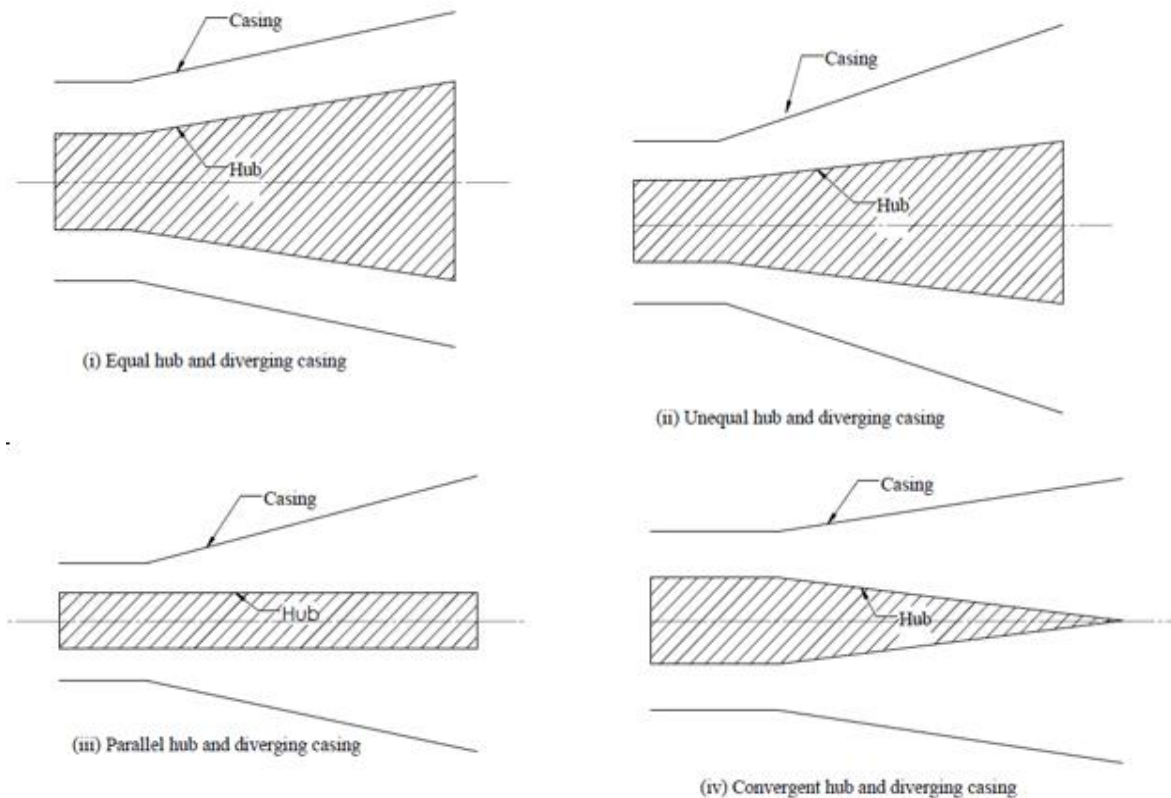


Figure 1.4: Geometrical design of annular diffusers.

Types of annular diffusers

- (1). Equal hub and diverging casing (EHDC)
- (2). Unequal hub and diverging casing (UHDC)
- (3). Parallel hub and diverging casing (PHDC)
- (4). Convergent hub and diverging casing (CHDC)

In the current study, swirling and non-swirling flows were used to evaluate the diffuser's performance with different geometrical parameters and inlet conditions.

1.2 Radial Diffuser

In this type of diffuser, fluid flows in a narrow space between the boundaries and moves out in the radial direction (Figure 1.5). The diffuser used in radial turbo machinery comes under this group. They may be vane less or vane types. This type of diffuser may change kinetic energy into static pressure rise via one or two methods: 1) A decrease in average velocity caused by increasing the size of the flow passage. 2) Change the mean flow path radius to recover angular velocity using the law of angular momentum conservation.

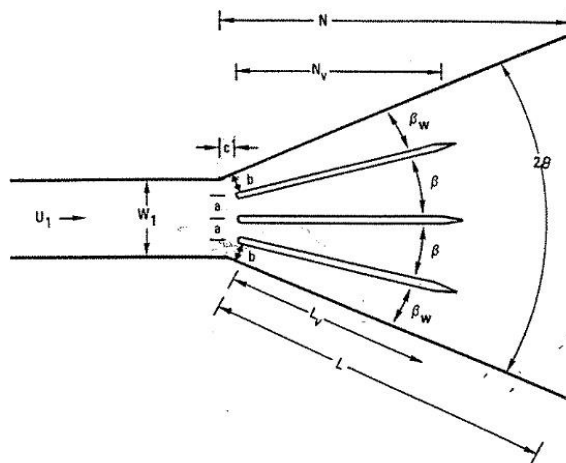


Figure 1.5: Vanned diffuser (Source: Applied Fluid Dynamics Handbook by R.D. Blevins (1984)).

1.3 Curved Wall Diffuser

In modern times, most aircraft use curved wall diffusers. In aircraft engines, several modifications may bring in non-uniformities and higher levels of turbulence in the flow field of curved geometry. The curved diffuser has more losses than the straight diffuser. But a small space is required to adjust the length of passage as compared to other diffusers. The curved wall diffuser is shown in Figure 1.6.

Curved diffusers are broadly classified as:

- 90 or part turn diffuser or half diffuser.

- 180 or U-diffuser.
- S-diffuser.
- Y-diffuser.

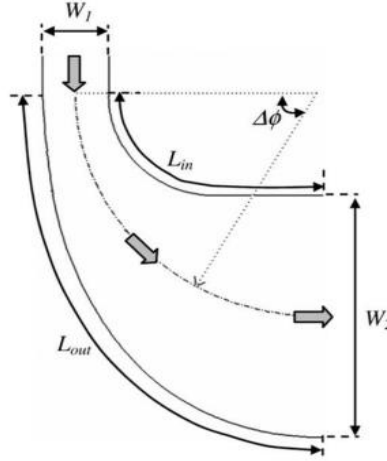


Figure 1.6: Curved diffuser (Source: Chong et al. (2008)).

1.4 Performance Parameters for an Annular Diffuser

The performance parameters are quite useful in the design modification of the diffusers. The annular diffuser's performance in terms of static pressure recovery coefficient (C_p), and total pressure loss coefficient (C_L) has been evaluated for swirling and non-swirling flow. These parameters show whether the designed diffuser geometry gives an optimum result or not.

1.4.1 Static Pressure Recovery Coefficient (C_p)

It describes the amount of kinetic energy transformed into pressure energy as a result of diffusing action in terms of static pressure rise from the diffuser's exit to the inlet section (Dunn et al.2009) and is given by Equation 1.5:

$$C_p = \frac{P_{ex} - P_{in}}{0.5\rho u_{avg}^2} \quad (1.5)$$

Where P_{ex} and P_{in} represent the static pressures at the diffuser's exit and inlet sections, respectively. u denotes the average velocity of a flowing fluid.

1.4.2 Diffuser Effectiveness (η)

It describes the actual recovery of the diffuser's pressure to the ideal recovery of the diffuser's pressure for the same area ratio, and it is given by Equation 1.6:

$$\eta = \frac{C_p}{C_{pi}} \quad (1.6)$$

$$C_{pi} = 1 - \frac{1}{AR^2}$$

Where AR represents the area ratio.

1.4.3 Total Pressure Loss Coefficient (C_L)

It describes the amount of total pressure drop caused by the turbulent intermixing of fluid and viscous forces to the inlet dynamic head (Equations 1.7-1.8).

$$C_L = \frac{P_{in} - P_{tex}}{0.5\rho u_{avg}^2} \quad (1.7)$$

$$k = \left(\overline{u_1^2} - \overline{u_2^2} \right) / U_i^2 - C_p = \left(\alpha_1 - \alpha_2 / AR^2 \right) - C_p \quad (1.8)$$

Where P_{in} and P_{tex} represent the total pressures at the diffuser's inlet and exit sections, respectively. α_1 and α_2 are the kinetic energy parameters at the diffuser's inlet and exit sections. If the velocity profile at the diffuser's inlet section is flat with a thin wall boundary layer, $\alpha \approx 1$. However, because the diffuser thickens the boundary layer, α_2 is generally greater than unity. Nonetheless, the kinetic energy coefficient is frequently assumed to be equal to unity, then

$$K = C_{pi} - C_p$$

The flow in the diffuser is subjected to an adverse pressure gradient because of reversal flow, and the separation zone occurs near the walls. The flow separation deteriorates

the performance of diffusers and destroys the downside apparatus. The primary goal of the diffuser design is to keep the adverse pressure gradient as high as possible while staying below the critical limit by controlling the area ratio versus the non-dimensionalized axial length.

1.5 Swirl Flow

The existence of a tangential velocity component characterizes swirl flow. Practically, this tangential component is often created using guiding vanes. The separation on the diffuser surface is delayed by inlet swirl flow because the flow is forced towards the wall by centrifugal force.

1.5.1 Physics of Swirling and Rotating Flows: -

The swirler creates a free vortex flow at the inlet of the annulus region with the principle of angular momentum conservation. The circumferential velocity in a swirling flow increases as the radius r decreases. A free vortex flow example is a cyclone. The figure represents the free vortex with the radial distribution of ω (Figure 1.7).

$$\frac{\partial p}{\partial r} = \frac{\rho \omega^2}{r} \quad (1.9)$$



Figure 1.7: Free vortex flow of ω in the radial direction (Source: *Fluent* user's guide (2014)).

The diffuser model is prepared in the *Fluent* module, then applies the boundary conditions as per swirl flow. The computed result shows that the static pressure distribution change corresponds to the axial and radial flow velocities. The modelling of swirling flows is very complex due to the combination of swirl and pressure fields.

Application of swirl flows comes out in numerous fields of engineering and the natural world. Examples of swirl flow in natural phenomena are tornadoes, whirlpools, and hurricanes. The swirling flow has been used very widely in industrial applications. Some of the practical applications of swirling flow are in non-reacting cases, such as heat exchangers, cyclone separators, vortex amplifiers, etc. In reacting cases, swirlers are generally used in the combustion system, e.g. gas turbines, industrial furnaces, ramjet engines, gasoline and diesel engines, and many more practical heating devices. The significant effect of swirl flow on combustion and various concerns are aerodynamics, mixing, the intensity of combustion, pollutant emissions, and flame stability.

1.6 Principle for Diffuser Design

The basic requirements for a good diffuser design are as follows: -

1. It must agree with the numerous inlet conditions such as extreme swirl, Mach number, and blockage.
2. The fluid is not separated across the length and delivered with a reasonable velocity.
3. The curvature of the wall must not harm passage performance.
4. Pressure recovery is achieved over a short axial length.

The best possible design of a diffuser is obtained by imposing some limitations on it.

1. Limited length
2. Specified cross-sectional shape
3. Specified area ratio
4. Maximum increase in static pressure
5. Minimum total pressure loss

The overall efficiency of the turbomachine depends upon the diffuser's direct and indirect output. The best performance phenomenon of turbomachinery is to be obtained by carefully studying and thoroughly optimizing the geometry of the diffusing portion of the diffuser.

1.7 The organization of the Thesis

The thesis is organized in the following manner:

Chapter 1 covers the diffuser's general introduction. Types of diffuser, performance parameters and swirl flow are introduced. The principle of diffuser design has been discussed.

Chapter 2 covers a comprehensive literature survey related to annular diffusers. The chapter highlights each parameter and its effect on performance. The research gap is mentioned, motivation, the scope of the present work, and research objectives have been listed.

Chapter 3 covers the details of the experimental setup, test diffuser, and instrumentation. The description of the annular diffuser, along with other important geometrical parameters, is presented. Details of instrumentation, their working principles, and their applications have been discussed. Uncertainty analysis is also presented.

Chapter 4 covers mathematical formulation and computational modelling procedures. The description of the turbulence model, residuals, solution procedure, and the geometry of the diffuser have been discussed.

Chapter 5 discusses the grid independence tests and validation of the computational results with the experimental data.

Chapter 6 presents the first part of the computational investigations. Results and discussion are presented on the effects of casing angle on the performance of the parallel hub annular diffusers.

Chapter 7 presents the second part of the computational investigations. Results and discussion are presented on the effect of swirl flow on the performance of axial annular diffusers.

Chapter 8 presents the third part of the computational investigations. Results and discussion are presented on the performance characteristics of flow in annular diffusers.

Chapter 9 lists the conclusions of the current thesis and briefly discusses the scope of future research work.

Chapter-2

2 Literature Review

This chapter gives the perceptiveness of the present state of science about the annular diffuser's flow behaviour by discovering the existing literature. To better understand the flow characteristics through these diffusers, investigators and researchers have analyzed the flow experimentally and numerically based on these prime review papers. The objectives and scope of the current study have been established.

Geometric parameters such as axial length, wall angle, area ratio, aspect ratio, and so on are required to define the optimal diffuser geometry. The fluid dynamic parameters, i.e. inlet velocity, velocity distribution, turbulence level, blockage factor, flow pulsation, Reynolds number, Mach number, and inlet swirl angle, assist in understanding the core flow phenomenon and diffuser's performance. The annular type diffuser exists particularly in turbo machines, where the fluid flows around and over a hub or a central shaft. The research of extensive nature has continued in progress since the previous decades by various researchers and giant manufacturers to carry out or define its optimum geometrical characteristics.

It is very well described that annular type diffusers are complex, and the parameters like the inner wall of the diffuser enhance the complexity. Annular diffusers are distinguished by boundary layer development, which causes various types of flow irregularities, instability, non-uniform velocity distribution, pressure loss coefficient, and flow separation. The experimental investigation assists the inventors in minimizing the unfavorable impact and thus optimizing the recovery of the static pressure increase. Analytical studies or empirical relationships united with the experimental investigation,

help in the improvement of diffuser performance. Figure 2.1 depicts the frequency of diffuser-related research articles published over the last seven decades.

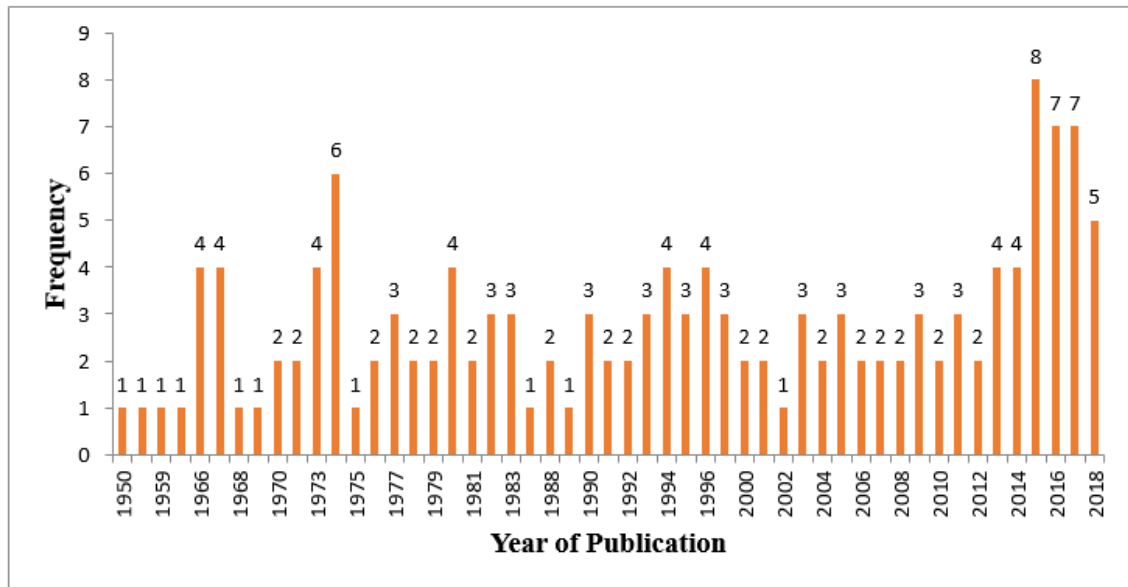


Figure 2.1: Frequency of articles on the diffusers.

2.1 Studies of Geometric Parameters- Passage Divergence, Length and Area Ratio

Duggins (1970); Azad (1996) demonstrated the effectiveness of conical diffusers with 8° - 12° wall angles and AR values ranging from 4 to 6 with an inlet radius of 5.5 cm. Within the AR range considered, the pressure recovery reaches a maximum at an area ratio of approximately 6:1 and remains constant with further increases in AR. Walker et al. (2003) found that raising the AR of the same axial length improved the C_p while decreasing the C_L in a hybrid diffuser when compared to a traditional diffuser. Sparrow et al. (2009); Salim (2013) examined the flow separation and diffuser performance in a diverging conical duct with different divergence angles. It has been seen that separation occurred at the 7° expansion angle of the diffuser having a $Re < 2000$. The length of flow separation diminishes with an escalation in the Reynolds number. Senoo et al. (1978) analyzed the impact of inlet swirling flow on pressure recovery coefficient in conical diffusers with different cone angles. Maximum pressure recovery was achieved

at an 8° cone angle. Figure 2.2 illustrates the diffuser effectiveness with the cone angle. It demonstrates that the maximum performance is obtained when the cone angle is 15° and the area ratio is 1.2.

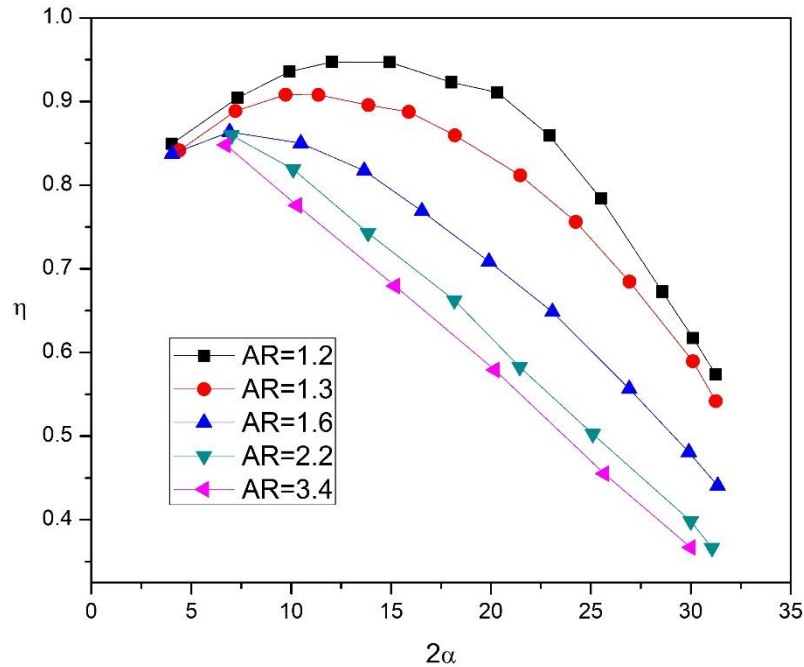


Figure 2.2: Relationship between diffuser effectiveness and cone angle.

Prakash et al. (2016) discovered that as the wall angles increased, the C_p decreased. There was a drop in performance due to the separation of flow in the diffuser. Keerthana & Jamuna (2012) examined the effectiveness of a set of annular diffusers with varying divergence angles. The static pressure and pressure recovery coefficient both increase and follow the same strategy as the flow proceeds up to the 21° divergence angle. After that, the diffuser performance deteriorates. Kibicho & Sayers (2008) observed flow reversal along the diffuser wall as a result of the two-dimensional geometry's adverse pressure gradient. The velocity increased from 12-22 m/s, then the static pressure increased by 9% for the given geometry of the 30° diffuser. Abdalla et al. (2006) investigated conical diffusers with different wall angles varying from 4° to 40° . The axial length of the diffusers is equal to 4.3 times the inlet diameter. The largest performance improvement was seen in wide-angle diffusers as compared to conical

diffusers having small divergence angles. Waitman et al. (1961) studied the flow characteristics of subsonic two-dimensional diffusers. The pressure recovery is observed to be dependent on the inlet-boundary conditions. When the thickness of the boundary layer increases, then the reduction in pressure recovery takes place. Pramod et al. (2014) investigated the effectiveness of a 13° divergence angle annular diffuser with a stabilizing diffusion length. At the inlet, the velocity varied from 80 m/s-160 m/s. Due to the high diffusion rate, pressure recovery rises as the AR increases. Johnston (1953) reported on annular diffusers with an AR value of 3 and divergence angles ranging from 6° to 15° . As the divergence angle increases, the efficiency decreases due to the inlet conditions being non-uniform. Figure 2.3 depicted the impact of the area ratio on the C_p .

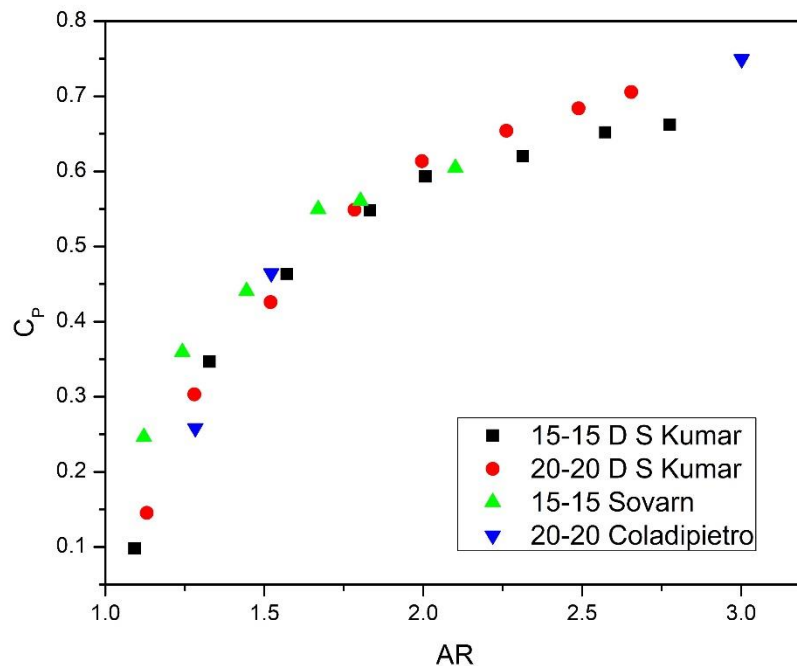


Figure 2.3: C_p with area ratio (Kumar & Kumar (1980)).

Shimizu et al. (1982) examined the conical diffuser performance with a divergence angle range from 5° to 18° and AR of the diffuser from 2.1 to 15.9. Good performance is achieved in the conical diffuser with an asymmetrical velocity profile at the inlet and

a one-directional swirling component. Cerantola & Birk (2015, 2015) predicted the effectiveness of short annular diffusers with and without swirl with area ratios ranging from 1.61 to 2.73. The highest diffuser performance is achieved with a 10° inlet swirl for an area ratio of 1.91. Ganesan (1980) reported on straight-core annular diffusers to predict the velocity profiles, momentum thickness, pressure recovery, effectiveness, and boundary layer development. The predicted pressure recovery coefficient agrees fairly well with the experimental data up to a cone angle of 15° . Kurokawa et al. (2010) studied J-groove's effect on a conical diffuser with a divergence wall angle of 20° . The velocity distribution result shows a 40% reduction in swirl intensity by installing the J-groove.

2.2 Inlet Velocity Profile and Distortions

The formation of a turbulent boundary layer on the diffuser wall causes the inlet velocity profile. The various methods were used to control the inlet velocity profile. It can be achieved by providing trip wires or center bodies or a sufficient length of constant area pipe ahead of the diffuser. The upstream pipe's approach length, displacement, momentum thickness, and profile 'peakiness,' among other parameters, define the inlet mean velocity profile. Inlet profile Peakiness is described as the maximum velocity divided by the mean velocity. As many researchers have discovered experimentally, the performance of a diffuser degrades as the boundary layer's thickness grows. The inlet boundary layer that has been thickened is equally important as the boundary layer's thickness in determining diffuser performance. Mehta (1979); Marsan et al. (2015) studied the diffuser performance depending upon the fluid flow's inlet velocity profile. The undisturbed profile in which fluid flow on the hub is stable while disturbed profile flow is separated from the hub and there is low shear stress on the surface. The inlet velocity distribution influences the static pressure recovery and

flow characteristics in the annular diffuser. Sajben et al. (1974) studied seven different inlet velocity profiles on the conical diffuser at a low subsonic speed. The performance is predicted using static pressure recovery and exit velocity distribution. Padilla et al. (2011) reported on three annular diffusers with different expansion ratios and four inlet situations. The distortion of the inlet velocity distribution in a two-dimensional diffuser has a considerable influence on the efficiency. The static pressure recovery is achieved at about 80% of the first-half part of the diffuser. The annular diffuser has an area ratio that ranges from 1.9:1 to 3.2:1, and different levels of Mach number. It is predicted that about 85 percent of pressure recovery is obtained in one-third of the diffuser length (Adkins 1975; Narayana et al.1984; Adkins & Wardle 1990). Lo et al. (2012) investigated the center body's effect on the conical diffuser. The Conada blowing method was employed to mitigate the central recirculation zone when the fluid's maximum momentum flows toward the center. Reneau et al. (1967) found that inlet settings have a much larger influence on diffuser performance than the flow regime. The integral turbulent boundary layer method was used to assess the C_p in the case of a two-dimensional diffuser. Their boundary layer was not too thick. Al-Mudhafar et al. (1982) predicted the static pressure in the two-dimensional diffuser. It was noticed that as the inlet velocity distribution is distorted, the pressure recovery of the diffuser decreases. Stevens (1967); Stevens & Fry (1973) analyzed the annular diffuser's performance; they discovered that the diffuser's effectiveness decreases as the outer wall momentum thickness increases. A reasonable compromise has been obtained between experimental and theoretical results for static pressure distribution, boundary layer development, and flow separation in the conical and annular diffusers.

2.3 Inlet Blockage Factor

The inlet boundary layer affects a diffuser's performance, which is generally investigated employing blockage factor B and the effective area-fraction E .

These terms are defined as (Equations 2.1-2.2):

$$B = 1 - E = \frac{1}{A} \int \left(1 - \frac{u}{u_m} \right) da \quad (2.1)$$

Here, A is the area of flow, u and u_m represent the local velocity and maximum velocity, respectively.

$$E = \frac{1}{A} \int \left(\frac{u}{u_m} \right) da \quad (2.2)$$

Kline et al. (1959); Kline (1981) examined the influence of inlet blockage, inlet turbulence intensity, and inlet shape factor on conical diffuser performance. The static pressure rises due to increases in the intensity of turbulence.

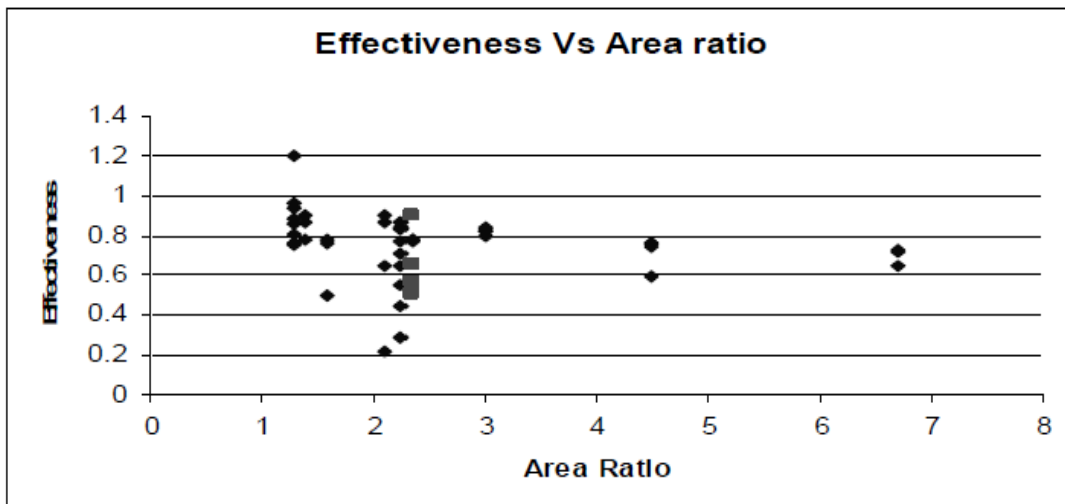


Figure 2.4: Graph plotted between diffuser effectiveness and area ratio (Japikse, 2002).

Figure 2.4 shows an annular diffuser's effectiveness, which depends upon the geometrical configuration, inlet swirl angle, and inlet blockage. The aerodynamic

blockage is a very important variable in determining the effectiveness of an annular diffuser. McMillan & Johnston (1973) investigated the potential of a low aspect ratio rectangular diffuser, considering the effect of fully developed, incompressible, and turbulent flow. In low aspect ratio, diffuser pressure recovery and effectiveness are very low compared to high aspect ratio diffusers. Overall, the low aspect ratio diffuser contributes 15% of total pressure drops to the pressure drops in the channel diffuser, which is equal to length. Senoo and Nishi (1977) used a boundary layer method to investigate flow separation in a conical diffuser. From the results, it was seen that more stable flow due to the large size of the blockage, very little flow separated from the boundaries. A relationship has developed between the shape factors and the blockage factors for the separation limit of fluid in the diffuser. The static pressure growth calculated from the experimental data is very satisfactory except for the separation point. Tyler & Williamson (1968, 1973) also showed experimentally that a continued increase in the inlet blockage resulted in the effectiveness rising again and eventually exceeding unity. The inlet distortion became severe enough, and the beneficial effect of mixing prevailed over the harmful effect of increased blockage. Experiments by Reneau et al. (1967) and the analysis presented by Sovran (1967); Sovran & Cocanower (1967) have indicated that diffusers of optimum geometry were only slightly affected by inlet distortion. Livesey & Odukewe (1973); Sharan (1976) studied the conical diffuser with the aerodynamic blockage as a function of approach length. The initial pressure recovery reduces and then increases as the length increases due to boundary layer growth. Noui et al. (2004) found the complicated effect of the different blockages, as seen by the diffuser's flow. Different screen configuration methods were used to achieve the uniform flow at the exit. Japikse (2002) reported the diffuser's effectiveness, which developed a correlation equation for the annular diffuser. The effects of

aerodynamic blockage and stall processes are reflected in velocity profiles and diffusers' overall performance.

2.4 Inlet Reynolds Number and Mach Number

Moller (1966); Adenubi (1976); Kibichov & Sayers (2008); Nordin et al. (2015) studied the impact of Reynolds number (R_e) on static pressure rise in the conical and radial diffusers, as the divergence angle was increased by some amount proportional to static pressure recovery. The proportion of pressure recovery increases as the Reynolds number increases. If the Reynolds numbers are below 10^5 for the radial diffuser, the pressure recovery decreases rapidly. Nordin et al. (2017) evaluated the flow behavior of 3D turning diffusers with numerous inlet conditions ($R_{e,in} = 5.79E4-1.78E5$) and geometrical parameters.

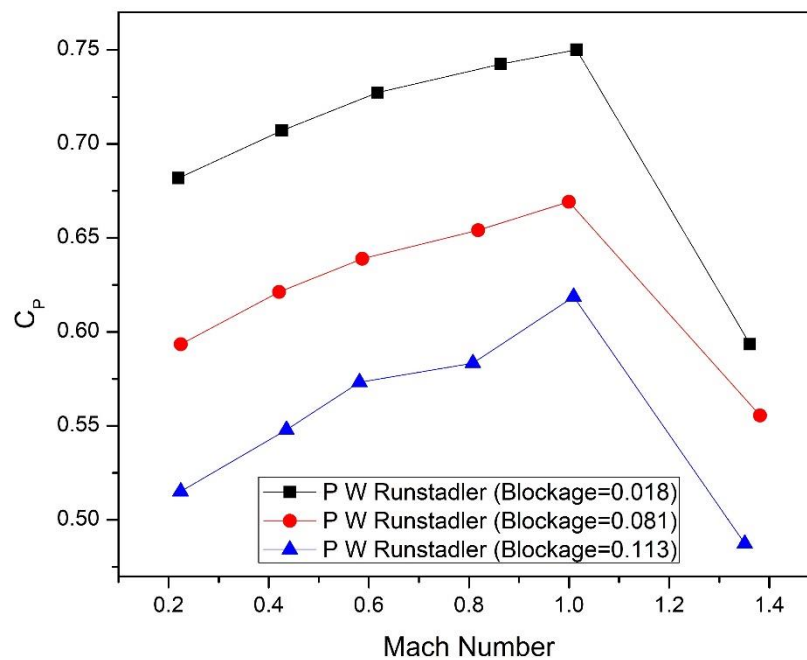


Figure 2.5: Static pressure recovery with Mach number (Dean & Runstadler (1969)). The function of inlet boundary conditions, the performance correlations are successfully developed via ACFD with approximately 7% experiment deviation. Gartner & Amitay (2016) analyzed the effectiveness of several passive and active

actuators of the rectangular diffuser. The efficacy of height, the array of passive vortex generators attached to the ramp's upstream, and vortex generator spacing on these parameter studies were conducted. Due to this, the AIP pressure recovery improved from 78.5% to 85.5%. The diffuser shock wave at the entrance occurred due to the Mach number, and total pressure reduced quickly as corresponding to the static pressure and static temperature increased rapidly by Wen et al. (2012).

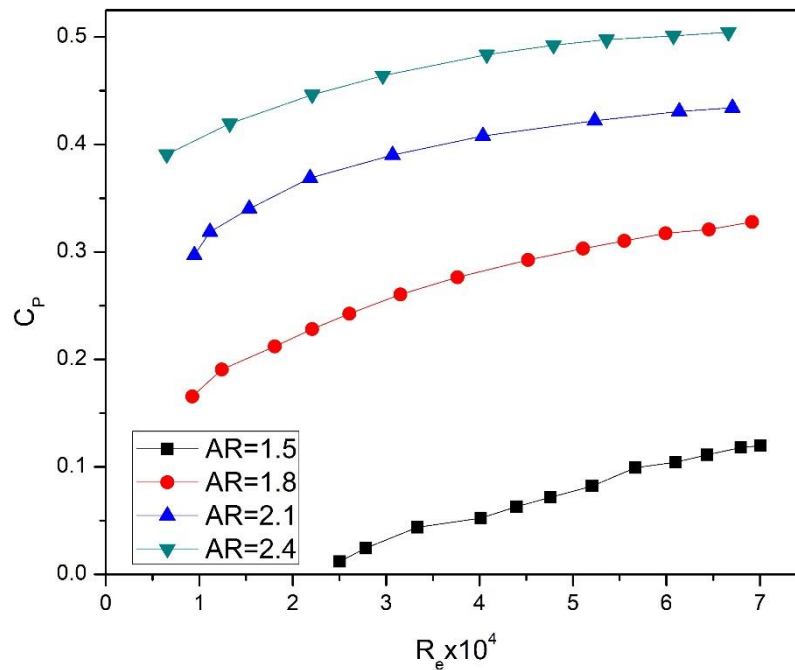


Figure 2.6: Static pressure recovery with Reynolds number (Mcmillan & Johnston (1973)).

Figure 2.5 shows the variation in Mach number with static pressure recovery for incompressible flow. Figure 2.6 depicts the static pressure recovery of diffusers increased by increasing the Reynolds number. Van & Fox (1966) discovered that the performance of an incompressible fluid in a conical diffuser depends on the Mach number. The diffuser's performance is independent of the divergence angle, which lies just below the first appreciable stall line at a specified Mach number and AR of the diffuser geometry. Little et al. (1950); Dean et al. (1969) studied the importance of geometrical parameters, Mach number, aspect ratio, and diffuser inlet blockage. The

diffuser's performance (pressure loss coefficient and effectiveness) is more influenced by the boundary layer size and wall angle. The performance of diffusers is reduced rapidly by increasing the value of these variables.

2.5 Inlet Turbulence Level

The turbulence intensity T_u is most frequently defined as an RMS value (Equation 2.3):

$$T_u = \frac{\left[\frac{1}{3} (u'^2 + v'^2 + w'^2) \right]^{1/2}}{U} \quad (2.3)$$

In this equation, u' , v' , and w' are the turbulent velocities in the x , y , and z directions, respectively, and U denotes the flow's mean velocity. Obi et al. (1993) used LDV measurements with different turbulence models to assess the performance of a turbulent separating fluid stream in a plane diffuser. The second-moment closure does not provide the appropriate level of shear stress component upstream of the flow separation. Redha et al. (2015) stated that diffusers reduce noise level and head loss in the largest wind tunnel configuration. The turbulence kinetic energy in the plane is analyzed to predict noise reduction. The results show that the same diffuser greatly reduces turbulence. Stevens & Williams (1980) conducted studies on outlet flow characteristics, static pressure rise, and loss of total pressure. The velocity profiles are assessed at numerous stations along the diffuser's length. The results show a gain in pressure recovery, outlet flow stability, and little gain in total pressure loss. Cho & Fletcher (1991) studied the conical diffuser with divergence angles of 8° - 20° to predict the complex turbulent flows. The velocity profile was accurately predicted using two turbulence models. The ASM Turbulence model predicted accurate results over the k - ϵ turbulence models when compared with the experimental value.

2.6 Inlet Swirl

Swirling flow indicates the presence of a tangential velocity component at the diffuser's inlet. The effect has been considered for conical and annular diffusers, even though it is important for two-dimensional diffusers as employed in various pumps and compressors. The common way of representing the swirl is in terms of the swirl's angle at the inlet.

Swirl flow has been generated by guide vanes located at the diffuser entry or by the rotation of a body placed within it. Dellenback et al. (1988); Ji-jun et al. (1992); Clausen et al. (1993) studied conical diffusers with a wall angle range of 12° to 20° , with a turbulent swirling flow with different swirl numbers. The flow separation is predicted by a two-layer wall function with algebraic Reynolds stress and k - ϵ turbulence models. The swirl tends to move the flow, which raises the velocity close to the boundary surface because there is a very small reversal flow from the surface. Singh et al. (1994, 2006) examined the behaviour of annular diffuser with various inlet swirl angles. The diffuser's best performance has been achieved by introducing a swirl; the optimal swirl angle lies between 20° - 30° . If the inlet swirl is increased further, a separation zone is observed on the inside wall, which degrades performance. Lohmann et al. (1979) studied the annular diffuser's performance with the conical wall of various lengths, area ratio, and divergence angle experimentally evaluated over a swirl angle range of up to 45° . The reversal flow takes place in the diffuser's inner wall; it can be encountered by raising the swirl angle at the lower AR . Mohan et al. (1998) analyzed three straight-walled annular diffusers with an equivalent cone angle of 25° , 30° , and 35° have been analyzed. The inlet swirls up to a certain level to increase pressure recovery but afterward has a harmful impact. The overall C_p is increased by around 40% for a swirl flow inlet in either a clockwise or anticlockwise direction.

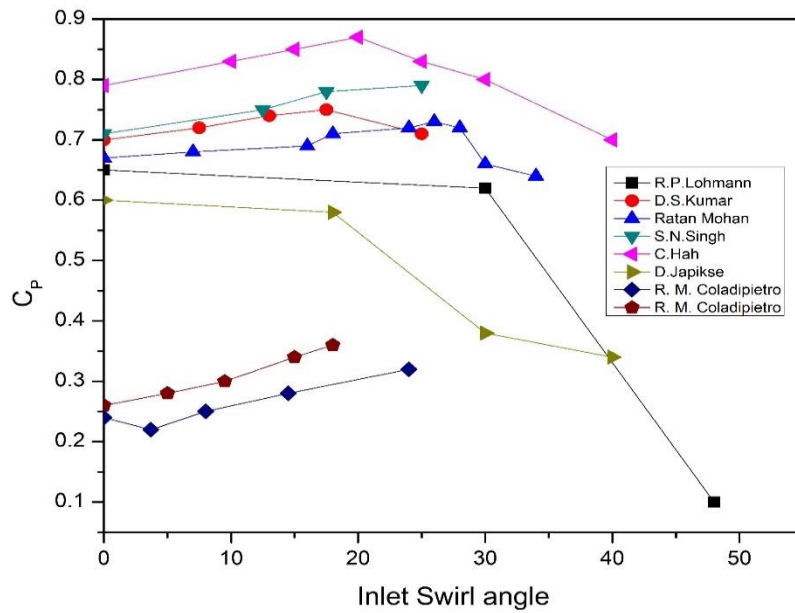


Figure 2.7: C_p with inlet swirl angle of the annular diffusers (Japikse, 2002).

Figure 2.7 indicates the optimum swirl angle for pressure recovery with different diffusers tested by plotting their performance against the swirl angle. When the swirl angle exceeded 30° , the velocity profile became distorted, reducing the diffuser's pressure recovery. Singh et al. (1994) worked on a wide-angled annular diffuser's performance with an equal hub and casing angle. The effect of the inlet swirl was evaluated regarding diffuser performance parameters and flow developments. Inlet swirl increases the C_p and suppresses the flow separation on the outer wall. The reduction in effective diffuser length is achieved by increasing the value of the inlet swirl angle. Kumar et al. (2011) examined the impact of various swirl angles ranging from 0° to 25° in the annular diffuser. It demonstrates that swirling improves the diffuser's performance with respect to the static pressure recovery coefficient. Kochevsky (2001) studied a hub's rotation with swirl flow in an annular diffuser installed at the hydraulic machine's exit. When the hub rotates in the flow direction, the swirl flow intensifies. The rotation of the hub in the reverse direction, then the swirl flow intensity decreased. Kumar (1977); Kumar & Kumar (1980) concluded that the annular diffusers have subsonic turbulent swirling flows in the diverging casing and

diverging hub geometries. The overall performance is increased because of the presence of swirling flow. The C_p in the diffuser increases as the flow proceeds, after that drops in C_p as the distance from the inlet increases correspondingly. Ghose et al. (2013) examined the impact of different dome shapes on pressure distribution and flow patterns along the walls over the various swirl number levels. Effectiveness and pressure recovery are achieved by considering the different levels of swirl angle in the range of 25°-30°. Kanemoto et al. (1982) investigated the thin and thick boundary layers in the annular diffuser with swirl flow. The best C_p is about 24° at the hub's best convergent angle, while the flow has no whirl component at the inlet. It is possible to prevent the flow separation by giving an adequate whirl flow component at the inlet. Crane & Burley (1974); Hah (1983) reported on the three diffusers for predicting the turbulent flow characteristics considering the effect of inlet swirl and distortion effects. The turbulence closure modelling is appropriately included in the outcome of streamline curvature. Fox & McDonald (1966, 1971) predicted the performance and effectiveness of twenty-four different conical diffusers, and wall angles varying from 5° to 32°, and area ratios varying from 1.2 to 9 were tested. It shows that swirling improves the overall performance of a complete flow system. Japikse & Pampreen (1979) found annular diffusers' performance with different parameters, i.e. inlet swirl, inlet blockage level, and Reynolds number. The maximum C_p in the exhaust diffuser is achieved at a 45° inlet swirl with a double collector. Coladipietro (1974) found the deviation of static pressure recovery with blockage in a short annular diffuser which was similar to the conical and channel diffusers. It also demonstrates that the C_p decreases as the blockage increases. However, for the long diffusers, higher performance is observed at the higher blockage levels.

2.7 Analytical and Computational Studies

Armfield et al. (1990) reported the turbulent swirl flow through the conical diffuser having a divergence angle of 12° - 20° . Swirl numbers were used to improve the recovery of pressure predicted by the two-layer treatment using the RSM turbulence model. To assess the accurate location, turbulence level, and variation of swirl flow in the axial direction. The turbulence quantity is evaluated with a two-layer wall function instead of a single-layer method. Dominy et al. (1998) used finite volume techniques to analyze the fluid flow using the standard k - ϵ turbulence model. The swirl affects flow characteristics such as the pass-through diffusing duct and redistribution of loss as present near the wall. Arora (2007), Arora & Pathak (2009, 2011), and Singh & Arora (2019) investigated annular diffusers with area ratios ranging from 2-4 and experimentally obtained inlet velocity profiles computed using computational fluid dynamics. The RNG k - ϵ model was used to validate experimental data and predict the performance of the annular diffusers. Gorman et al. (2016) evaluated five turbulence models using experimental results with swirl flow in numerous engineering practices. The most effective model for heat transfer applications was the SST κ - ω . Predictions of the velocities near the apparatus's wall were especially excellent compared to the other model's predictions. Barbosa et al. (2015) mathematical model was developed to work on internal velocity behavior for three conical diffusers. The velocity gradient is positive; the model matches the experimental data within the diffuser area with a maximum velocity value. At large angles of the diffuser, the velocity gradient is negative, and experimental data is incompatible with the theoretical results due to the separation of flow and viscous effects. El-Askary et al. (2015) numerically validate the two-different flow by using the Eulerian-Lagrangian approaches and the k - ϵ turbulence model. The problem was solved using two techniques: continuous phase and dispersed

phase. Vlahostergios & Yakinthos (2015) reported two different Mach numbers in a converging-diverging diffuser with the transonic flow. The nature of flow in a diffuser gives quite exact results using more complicated turbulence models. Selvakar thick et al. (2016) stated the highest possible static pressure rise with the shortest possible length in the gas turbine engine with a dump diffuser design. Lipeng et al. (2016) evaluated the turbulent flow in the rectangular asymmetric diffuser by CFD with seven turbulence models. When it comes to assessing static pressure, velocity, vortices, and flow characteristics, the RSM turbulence model outperforms the other turbulence models. Vassiliev et al. (2002) assessed several turbulence models: realizable $k-\epsilon$ and standard $k-\epsilon$ models, one-equation models, and wall function. Among these models, the $k-\epsilon$ realizable model with a two-layer wall function proved to be the most suitable for accurate flow simulation. Sheeba and Ganesan (2005) investigated the characteristics of an annular diffuser for various flows and made good predictions using the $k-\epsilon$ model rather than a satisfactory physical model. The flow was disturbed and spread in the diffuser due to the strut. The development of pressure recovery without strut in the diffuser was more than the strut's pressure recovery. Yongsan et al. (1992) investigated a conical diffuser with a cone angle of 6° and an AR of 3, simulated by the standard $k-\epsilon$ model and with Reynolds numbers ranging from 1.16×10^5 - 2.93×10^5 . The flow characteristics in the diffuser, turbulence energy, and mean flow velocity are predicted using the BFC technique inside conical diffusers. Kanemoto & Toyokura (1983); Mansour et al. (1987) examined the impact of eddy viscosity damping on Reynolds number and boundary layer growth close the surface. The analytical outcomes display that due to the spread of the free vortex flow region, very good flow behavior and axial flow increase near the inner wall.

2.8 Gaps in Literature

- The effect of inlet swirl on the flow separation is scantily studied.
- The study on the effect of separation on performance of the axial annular diffuser is scantily studied.
- The effect of inlet swirl in conjunction with area ratio is scant in the literature for annular diffuser.

2.9 Motivation

The motive of this work is to enhance the performance of annular diffusers by considering the gaps in the literature. The study was conducted by various researchers solely in the last five decades without careful consideration of how all the studies are interconnected. A systematic methodology has been developed by considering all database elements for the investigation of the annular diffusers.

The review has been carried out to re-examine different aspects of the diffuser's flow behavior and present them systematically and in proper perspective. The impacts of various geometric and dynamic specifications on a diffuser's performance have been described to draw a certain conclusion. The effects of the geometric variables regarding pressure recovery are fairly well-founded for two-dimensional diffusers, conical diffusers, and to a certain extent for annular diffusers. However, the effects of the flow variables have not been established yet to the same degree as the geometric parameters. The reason is complicated coupling among the various flow parameters involved, besides the boundary layer development and adverse pressure gradients. A variety of boundary layer control methods and devices that are normally employed to improve diffuser performance have been outlined. It is established from the literature survey that most of the investigations till now have been confined to two-dimensional and conical diffusers due to their simplicity. Annular diffusers that involve many geometric

parameters have received considerably less attention and need to be investigated further. Diffuser research till now has been primarily concerned with evaluating the overall diffuser's performance rather than assessing the flow process involved. The diffuser flow behavior can be achieved by conducting systematic investigations of diffuser performance in terms of boundary layer development. Further, a study of the development of flow with inlet introduced swirl is necessary to assess an annular diffuser's performance, which may receive the exit flow from a compressor with a certain degree of swirl. Furthermore, it is found that most of the studies on axial annular diffusers are confined to experimental results only (i.e., hub and casing diverging with equal and unequal angles). Studies need to interlink the various inlet conditions on the effectiveness of the straight hub diverging casing diffuser with inlet swirl, inlet turbulence intensity, and Reynolds number. The computation models for annular diffusers are scant. Computational studies which can produce results close to the experimental measurements need to be developed. Therefore, future research activities need little experimentation and computational studies.

2.10 Scope of the Present Work

The fluid flow in conical and channel diffusers has been well documented in published literature. The effectiveness of the diffuser is predominately influenced by the AR and passage length in which diffusion occurs. The curvature of the wall influences the local pressure gradients and boundary layer growth, which can have a significant impact on diffuser performance. A literature review on flow through diffusers shows that past research focused on the study of plane diffusers and conical diffusers rather than on annular diffusers. The current study is an attempt to investigate the performance of annular diffusers under the various inlet conditions listed above. The inlet conditions mentioned above, e.g. divergence angle, inlet swirl, area ratio, inlet velocity profile,

turbulence intensity, Reynolds number, etc., are expected to have a convincing influence on diffuser performance. The efficiency and performance of the annular diffuser depend upon various geometrical and flow parameters. Efforts have also been made to assess the flow separation in the annular diffuser. The experimental/analytical data about the C_p and C_L for an extensive range of inlet conditions and swirl intensity are scant. It may well be due to the complexity of swirling flow, both with regard to measurements and analysis. There have been very few experimental studies on the research activities in the region of annular diffusers. Experimental research requires precise instruments for measurement and it is a complicated and time-consuming process, so it is not economically viable. Therefore, the current work concentrates on experimentation combined with Computational Fluid Dynamics (CFD) modelling to reveal some aspects of flow behavior through annular diffusers with equivalent cone angles ranging from 10° to 20° and area ratios 2-4. The current study was carried out to evaluate the velocity profiles, static pressure recovery coefficient, and total pressure loss coefficients at numerous cross-sections of the annular diffuser coupled with inlet swirls of 7.5° , 12° , 17° , and 25° , as well as without swirl (0°). CFD modelling of the experimental diffusers was carried out for various configurations. The complex flow behavior of annular diffusers was studied and compared with experimental results. The model closely related to the experimental data was used for further investigations to predict other annular diffuser flow behavior. Based on the extensive literature review, the present study has the following main objectives:

1. To analyze the region of flow separation
2. To visualize the flow development and separation of flow at different passage heights along the length of the axial diffuser

3. To study the variation of static pressure recovery coefficient, total pressure loss coefficient, velocity profiles at different area ratios, and divergence angles
4. To evaluate the effect of inlet swirl on performance
5. To assess the performance of the annular diffuser configurations, experimentally and computationally.

Chapter -3

3 Experimental Methodology

The current experiment was designed to explore the influence of geometrical and dynamical parameters on the flow characteristics and a diffuser's performance. The primary goal of the test setup is to gain insight into such complexities of flow in the annular diffuser. The designed experiment was used in the perfect method, which shows the geometrical effects and flow parameters effects in terms of flow visualization in the diffuser. The designed setup was used for testing all diffusers which were used in this project.

As previously stated, the flow is extremely complex due to the presence of adverse pressure gradients on the surfaces and the non-uniform velocity profile in the annular diffuser. Swirl flow passes through the diffuser which further increases the fluid complexity. To better understand the flow behaviour, flow structure, and flow complexity in the annular diffuser is very important. The prediction techniques would help to produce the data for experimentation so that a better design of the diffuser can be made.

The current experimental setup has been designed to examine the flow performance data in the annular diffuser based on mean flow quantities. These flow quantities were measured in the PHDC annular diffuser in relation to the inlet condition of the two-dimensional axisymmetric swirl and non-swirl flow.

This chapter deals with the experimental setup, instrumentation, and uncertainty analysis of the measuring instruments. Further, it describes the velocity profile and pressure measurements made along the annular diffuser's longitudinal length at various

cross-sections of the flow passage. The produce data from the experimental measurements serve as the baseline of the diffuser design.

3.1 Experimental Setup

Figures 3.1 and 3.2 show the test rig used for experimentation on the annular diffuser. Figure 3.3 represents the main components of the setup, i.e., blower, settling chamber, swirl plate, annular passage, and diffuser. The centrifugal blower sucks air from the ambience and passes to the settling chamber with the help of a conical divergence section, which is precisely aligned with the settling chamber. The airflow rate is controlled by changing the rpm of the impeller and a throttling valve placed at the inlet. The settling chamber consists of a honeycomb and different mesh screen sizes to prevent flow fluctuation, reduce the level of turbulence, and make the flow uniform. The settling chamber's well-designed conical contraction zone is linked to the long annulus passage through which flow begins. To achieve the desired swirl flow at the diffuser's inlet section, swirl plates of various angles are installed turn by turn at the annular passage's entry. The swirl plate is located on the upside of the diffuser to avoid the wake effect at the test diffuser's entry to recover the pressure. The test diffuser is made of transparent Perspex and the hub is the cast of aluminum material, which is perfectly machined to get a smooth surface and is fabricated with a precision of ± 1 percent tolerance. The measurement was made of the incompressible flow with steady-state conditions achieved prior to recording the data. A number of static pressure taps are mounted on the test diffuser's casing and hub walls, and static pressure is assessed using manometers. To increase the sensitivity of the reading, the manometers were tilted at an angle of 10° to the horizontal surface.



Figure 3.1: Actual experimental setup of the diffuser.

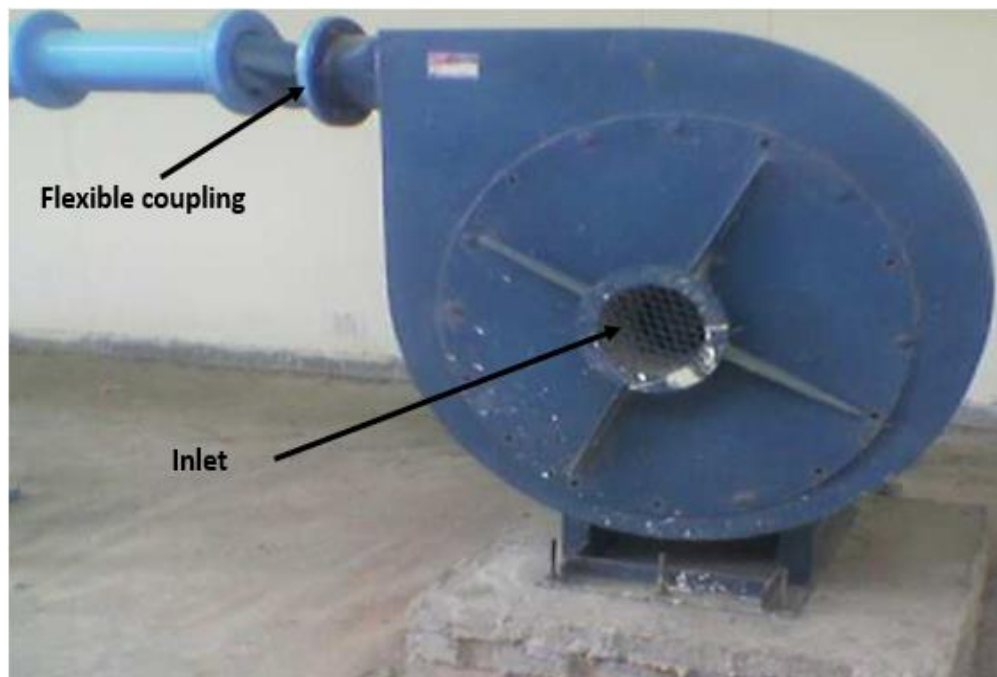


Figure 3.2: Centrifugal blower used for the experimental setup.

The longitudinal and swirl velocities were measured with a cobra probe at various axial locations in the test diffuser using the null technique. The calibration range associated with the cobra probe measures the velocity within $\pm 55^\circ$. The manometer's uncertainty in measuring static and total pressure is ± 4 mm and ± 3 mm of water, respectively.

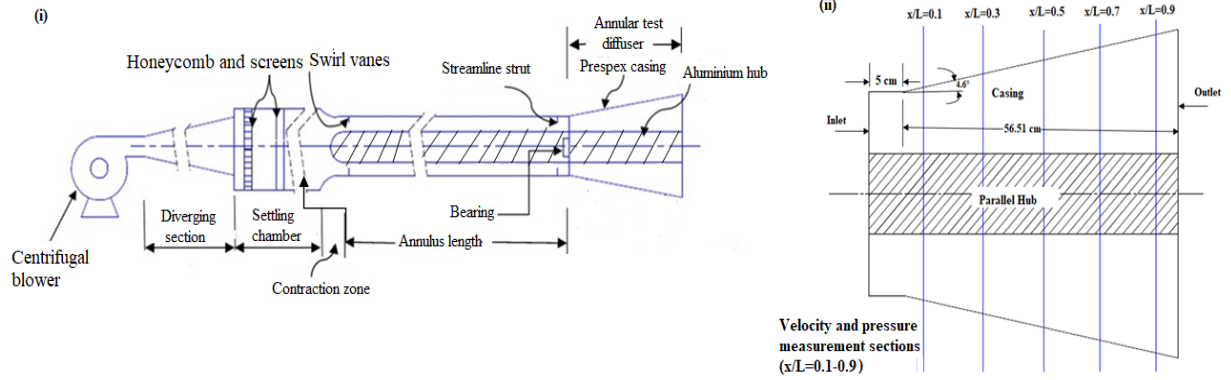


Figure 3.3: (i) Schematic of experimental test rig; (ii) location of actual measuring stations.

3.2 Geometrical Specification of the Test Diffuser

According to Fox & Kline (1962), the diffuser test geometry was developed to increase the area from the inlet to the outlet with an overall length of 0.32 m. The test diffuser was constructed with an AR of 2 and the other geometrical parameters listed in Table 3.1. The study's primary goal was to examine the impact of inlet swirl flow through the annular diffuser on separation flow and flow reversal in the diffuser.

Table 3.1: Geometrical parameters of the PHDC annular diffuser with an equivalent cone angle of 15° , $AR = 2$.

Sr. No.	R_{hi} (cm)	R_{ci} (cm)	θ_h (deg)	θ_c (deg)	L (cm)	L/AR	θ_e (deg)	AR
1	3.8	7.75	0	6.7	21.25	5.37	15	2

3.3 Swirl Generation Technique and Specification

Swirling flows are very widely used in industrial applications. The practical applications of swirl flow in the reacting combustion system include gas turbines, boilers, industrial furnaces, diesel engines, and many other heating devices. In recent years, numerous methods have been used to attain the swirl flow for experimental study.

The most appropriate methods are mentioned in the literature; some of the methods are used to generate the swirl flow as follows:

- The diffuser is mounted immediately at the outlet of the turbomachines;
- Axial flow deflects tangentially using fins or adjustable propellers;
- The fluid is passed through the rotating mechanical device, which generates the swirling flow;
- The fluid is inserted into the main duct using the tangential injection of the stream;
- Use of twisted tape inserts;
- The flow of air is through the stator vanes.

The above-listed methods cannot be said to be the best methods to attain the swirl flow. All of these techniques have their merits and demerits. The swirl flow was imparted by air passing through the stator vanes (swirl plate). The swirl plate is a simple steel flat plate with twelve radial cuts on it. The magnitude of the swirl was generated by adjusting vanes at particular angles. Whenever the desired magnitude of the swirl was required, the corresponding swirl plate was inserted at the annulus passage's entry section. The swirl plate position was preferred upstream of the annular passage to reduce the diffuser's wake entry. If the wakes had remained in the diffuser, the performance would have deteriorated. A Swirl can be defined as the swirl plate's geometrical feature for the swirl's generation, or it's calculated on the area-average value of the swirl angle. The last method is considered for specifying the swirl angle, which is a far better method than the previous ones. The swirl angle may vary along a passage due to that average process become necessary. The amount of swirl is defined by the swirl number (S). It characterizes the strength of the swirling flow. It describes

the axial flux of the angular momentum (G_ϕ) to the axial flux of the axial momentum (G_x) (Gupta et al. 1984) given in Equations 3.1-3.3:

$$S = \frac{G_\phi}{G_x R} \quad (3.1)$$

$$G_\phi = \int_0^R uwr^2 dr \quad (3.2)$$

$$G_x = \int_0^R u^2 r dr \quad (3.3)$$

Here, u and w are denoted by the axial and tangential velocities, respectively; R is the cross-sectional plane's radius; r is the radial coordinate.

Another representation of swirling flow is the swirl angle, which denotes the angle between absolute velocity and axial direction. When the swirl introduced is uniform along the axial direction, such as the flow induced by swirl vanes, the swirl angle is appropriate.

(1) Weak swirl ($S < 0.3$)

A swirl number below 0.3 is called a weak swirl. In the case of weak swirl flow, no separation bubble is developed by the pressure gradients.

(2) Medium swirl ($0.3 < S < 0.6$)

When the swirl number lies between 0.3 to 0.6, then it is known as a medium swirl. A light separation bubble is developed due to a larger axial pressure gradient in the medium swirl.

(3) Strong swirl ($S > 0.6$)

When the value of the swirl number is more than 0.6 is referred to as a strong swirl. The strong swirl number, very large size separation bubbles are established because of the radial and axial pressure gradient.

3.4 Diffuser Inlet Location

The inlet's fluid flow conditions should be considered ideal, which is the diffuser's geometric starting point. The mounting of the pressure tap at the transition is complicated, so the diffuser's inlet location is chosen the somewhere upper side of the test diffuser. The inlet position was selected to reduce the streamline curvature effect at the annular diffuser's entry length. The inlet diffuser's section was selected 5 cm upper side of the actual geometry entry of the test diffuser, which reduced the diffusion process and friction loss is very less compared with the real diffuser loss. In addition, the inlet's velocity profile would be very slightly changed compared to the diffuser's actual geometry start.

3.5 Instrumentation

The velocity and pressure of the annular diffuser were measured using a cobra probe. The yaw angle of the cobra probe was set manually with the traversing mechanism. The three-hole cobra probe, manometers, and traversing mechanism are explained as follows:

3.5.1 Three Hole Cobra Probe

A three-hole probe was used to measure the velocity and pressure components of the flow field. The probe was fabricated with three tubes of hypodermic stainless steel with a 0.08 cm outer diameter. The pressure probe size was selected to measure the pressure with accuracy and balance the pressure transmission lag whereby the probe is utilized, as recommended by Bryer et al. (1955, 1971); Dellenback et al. (1988).

The center tube square cut was shaped in the probe's leading-edge, whereas the remaining two tubes were chamfered at 45° individually to the respective tube axis. The three tubes were paralleled, coplanarized, and soldered into a 3 mm steel bar. These

tubes were assembled with maximum yaw sensitivity. To avoid errors caused by flow inferences, the probe's stem was formed 50 mm away from the tip. The cobra probe was mounted on a traversing mechanism for the measurement.

The probe's orientation relative to the mean velocity, the dynamic head, and the total pressure were the factors that influenced the pressures recorded by a given three-hole probe. The pressure readings can, therefore, be grouped into three different dimensionless parameters, each representing separately the flow direction, the dynamic head, and the total pressure. For steady incompressible flow along a streamline, the total pressure is calculated as follows:

$$p_t = p_s + \frac{1}{2} \rho U^2 \quad (3.4)$$

The equation of energy balance amid a point in the free flow and any of the holes of the three tube probe was used to develop suitable functional relations. The energy conservation equation correlates the pressure P_i indicated by one of the cobra probe tubes as

$$p_i = p_s + k_i + \frac{1}{2} \rho U^2 \quad (3.5)$$

Where K_i is a factor dependent on the probe geometry, the stream direction in relation to the tube, as well as the tube's identification, i.e., $i = 2$ for the mid tube and $i = 1$ and 3 for the side tubes. Thus:

$$\frac{p_2 - p_1}{p_2 - p_3} = \frac{k_2 - k_1}{k_2 - k_3} = f_1(\theta) \quad (3.6)$$

The functional relationship for the total pressure was determined by using Equations 3.4 and 3.5. The resultant expression of the total pressure is

$$p_j - p_1 = (k_j - k_2) \times \frac{1}{2} \rho U^2$$

Where $j = 1 \text{ \& } 3$

$$\frac{p_j - p_2}{p_t - p_s} = k_j - k_2 = f_2(\theta) \quad (3.7)$$

The resultant expression of the total pressure is

$$p_t - p_2 = \frac{1}{2} \rho U^2 (1 - k_2) = \frac{p_j - p_2}{k_j - k_2} (1 - k_2)$$

$$\frac{p_t - p_2}{p_j - p_2} = \frac{1 - k_2}{k_j - k_2} = f_3(\theta) \quad (3.8)$$

The tube 'j' is chosen in this manner to maximize the velocity range as well as direction sensitivity. The calibration functions mentioned above were determined experimentally by noting the pressure readings of the tubes for a known probe orientation in relation to the velocity of the free stream. The method outlined and used in this study was the same as that explained by Dau et al. (1968); Perry (1974) for investigating the asymmetric response of a three-tube cobra probe.

A probe calibration was carried out to determine the variation in pressure coefficients (as discussed in Equations. 3.6, 3.7, and 3.8 above) with the change in the yaw angle. The calibration of the probe was performed in a wind tunnel. First of all, the probe was aligned along the direction of flow. The probe's alignment in the direction of flow was ensured by rotating the probe until the two side tubes registered equal pressure. Then the probe was orientated relative to the flow direction and the pressure

sensed by the three tubes was recorded. The orientation was varied up to 40° in steps of 2° .

Reproducibility of response to the probe angle was ascertained by varying the orientation in both directions, from 0° to 40° and then from 40° to 0° . Once the calibration procedure was completed, it was put to test at some random angles. The probe calibration data obtained in the manner stated above was then used to calculate the functions f_1 , f_2 , and f_3 . During actual measurements in the diffuser, the probe orientation was kept fixed and readings of the three tubes were recorded at each of the traversing points. The flow variables were then evaluated in the following manner:

- i. Probe pressure readings P_1 , P_2 , and P_3 were used to compute the values of probe geometry constants and hence the functional parameter f_1 as described in Equation 3.6.
- ii. The functional constant for the dynamic head is then computed as given in equation 3.7 and the functional parameter f_2 is then calculated. The yaw angle corresponding to the calculated f_1 was determined from the calibration constant as calculated in Equation 3.6. The values for functions f_1 and f_3 corresponding to this yaw angle were obtained as explained in Equations 3.7 and 3.8.
- iii. The values of f_2 and f_3 as obtained in step (ii) and the indicated pressure readings P_1 , P_2 , and P_3 were used to obtain values for $(P_t - P_s)$, P_t , and P_s .

The above measurements cum calculation method provided an easy and rapid technique for calculating the desired flow parameters within acceptable limits of accuracy.

3.5.2 Manometers

The static pressure in the diffuser was measured with a 36-tube multi-tube water gauge manometer that is scaled to one-tenth of a centimeter. The manometers were tilted at a 10° angle to the horizontal to increase measurement sensitivity. The menisci in the tubes

were found to be at various levels when the manometer was tilted. This error, despite its small size, was corrected by using the pressure data adjusted to the corresponding flow parameters. Prior to data collection, proper precautions were made to confirm that steady-state equilibrium conditions in the diffuser length were achieved. In addition, to allow the probe system to reach a steady-state equilibrium condition, a time gap of 4 to 5 minutes is required among measurements. The leakage of the manometer's head and Polyvinyl chloride pipes were checked several times. The manometer panel enabled direct observation of the pressure distribution during the measurement.

3.6 Traversing Mechanism

This mechanism was built to hold the cobra probe properly without any free movement (Figure 3.4). The mean turbulence velocity in the flow regime is assessed using this mechanism, which has two degrees of freedom. These two degrees of freedom mean that the cobra probe traverses in the longitudinal direction and rotates about its axis. The traversing mechanism's least count in the longitudinal direction was retained at 0.1 mm, whereas the rotation was kept at 0.5° . The three-hole probe was attached to the traversing mechanism and then placed in the fluid stream to measure velocity and pressure. The probe was fixed to the flow passage's reference position, which aligns with the flow direction with an accuracy of $\pm 2^\circ$ and touches the diffuser's hub surface. Reading with a probe closer than 0.5 mm could not be possible near the hub and casing wall because the probe head was 0.5 mm in radius. In the boundary wall area, measurements were made in steps of 0.5 mm near the walls. But the large step was taken away from the walls, and the step was adjusted in such a way that 15 to 20 points covered the diffuser passage height at the particular traverse position. The backlash error of the system was removed by stirring the traversing mechanism in the same path when taking any single set of measurements.



Figure 3.4: Traversing mechanism for the experimental setup.

3.7 Initial Conditions

The physical conditions of the flow that is entered into the diffuser are accessed by the beginning flow conditions. The fluid goes via a lengthy annulus pipe with a hydraulic diameter 50 times that of the diffuser intake before entering the diffuser. The annular diffuser's inlet section had a fully developed turbulent flow. Some investigators use thin boundary layer flow, but the fully developed turbulent flow has been taken into consideration with and without a swirling. It is preferred to the turbomachinery diffuser's actual entry conditions. At the exit of the diffuser, no tailpipe was mounted, and there was atmospheric pressure. The experiment was performed in the incompressible flow area at a Reynolds number of $2.5E5$ on average, which was calculated based on the diffuser's equivalent diameter at the inlet. The turbulent boundary layer flow was checked for axial symmetry before carrying out the test diffuser's actual measurement. The measurements were made on static pressure's lateral

fluctuation. The inlet velocity profiles were obtained experimentally for the diffuser transverse as illustrated in Figure 3.5.

3.8 Experimental Procedure

The experimental observation results from each diffuser are as follows:

- Static pressure at the walls;
- Velocity profiles at the inlet;
- Velocity profiles at the various cross-sections;
- Visualizations of flow.

3.8.1 Static Pressure Measurement on the Wall

Static pressure tapings were installed on the casing surface's generatrix and the test diffuser's hub surface. The tap holes were drilled very carefully with a 0.3 cm inside diameter, and stainless steel tubes were inserted into the taps with 0.15 cm inside diameter and 0.3 cm outside diameter and flush with the inside surface. The pressure taps were connected to the inclined manometer using polythene tubing. The static pressure at the walls was determined in diametrically opposed portions at the different circumferential tapping, which shows the axial symmetry of flow. The deviation from the reading was recorded to be $\pm 3\%$ of the mean inlet dynamic flow. The flow was considered axisymmetric due to the very minor deviation.

3.8.2 Velocity Profile Measurement

A cobra probe was used to determine the transverse velocity profiles at different cross-sections relative to the diffuser hub surface. To insert the probe for velocity measurement, a series of 3 mm holes were bored into the diffuser surface at equally spaced over its span. The air from free apertures does not leak, which is completely plugged with round-shaped inserts. The velocity profiles in the flow field were

determined using static pressure and total pressure in different sections. The cobra probe was used to measure the three variables along the flow path's different transverses. The flow was supposed to be stable, inviscid, and incompressible. Using the energy conservation principle, Velocity U was computed at each location of the flow regime. The longitudinal and swirl velocity were calculated as given below:

$$u = U \cos \varphi$$

$$w = U \sin \varphi$$

Here φ represents the probe yaw angle.

The swirl and longitudinal velocities were non-dimensionalized in terms of the maximum longitudinal velocity, i.e. U_m at any transverse section. The obtained non-dimensionalized velocity profiles u/U_m and w/U_m were plotted about the diffuser passageway radius, i.e. y/Y_m . The measurement of the flow field was conducted at different cross-sections of diffuser passageways at various inlet swirls.

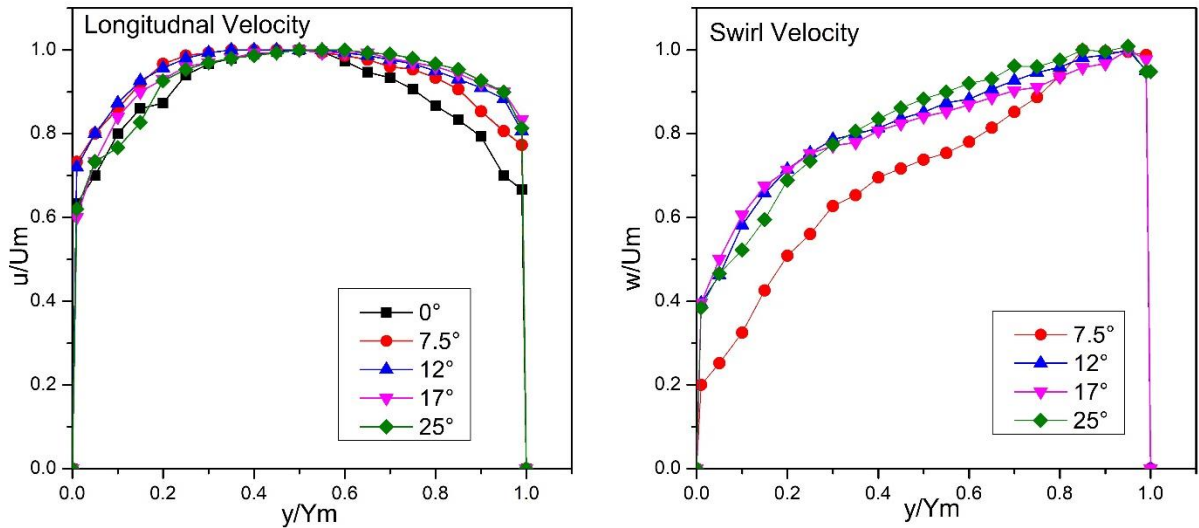


Figure 3.5: Inlet velocity profiles with an equivalent cone angle of 15° , $AR = 2$.

3.8.3 Flow Visualization

The flow pattern in the test diffuser was observed by the small wool tufts, which are 2.5 cm long and have the capability to move in any path. These tufts were attached to

the four generatrices, which are around 90° apart on the diffuser casing and hub walls. The tuft movement could be seen through the casing of the diffuser, which is transparent. The motion of the wool tuft has the potential to categorize the flow regimes for subjective interpretation. However, the available literature on the topic reveals that, according to a categorization proposed by Carlson & Johnston (1967).

3.9 Uncertainty in Measurements

The observations were taken by the experimenter with utmost care and followed the precautions rule, which is to eliminate all possible errors. Some errors in experimental readings are attributable to geometrical imperfections in the test equipment, whereas others are related to inaccuracies in the measurement instruments.

The test diffuser's casing was made from a 0.4 cm thick Perspex sheet that was first heated in an oil bath before being wound around a hardwood conical piece with the necessary sizes. The sheet is joined by a longitudinal butt joint, and the full length of the butt joint is reinforced by attaching a Perspex strip to the upper side. The flange is provided at both ends of the test diffuser. The inlet flange was used to connect the test diffuser to the straight annular path in the setup. Rolling inevitably results in an 'out of roundness' in the test diffuser's casing. Hence, its diameter deviated from the ideal taper diameter, resulting in a divergence angle inaccuracy for the casing. The hub is made of cast aluminium, then it's machined. Better precision in terms of the diverging angle of the casing wall and the hub diameter is obtained. The aforementioned variations indicate that the flow path of the hub and the casing wall of the diffuser assembly are affected. The adjustment of the hub inside the casing set at a particular level influenced the passage height. Similarly, one pipe fits into another pipe due to small irregularities in the passage height of the straight annular duct.

Many factors exist, both knowingly and unknowingly, that affect probe readings, including pressure tube leakage, misalignment of the cobra probe, surface condition of the manometer, and fluctuation of the stream pressure and atmospheric pressure, among others. The near-wall treatment was probable due to which pressure probe readings were taken away from the surface. Further, the used probe in the measurement had a minor size and its response to the enforced pressure was fairly slow. The utmost care was taken and the slow response of the probe due to that, adequate time was required to record the reading. The readings were recorded without stabilizing the pressure, so there was always a possibility of error. The impact of the backlash on the micrometer screw cannot be taken out completely, since all values are recorded along the same route. Table 3.2 shows uncertainty linked to the quantities measured.

Table 3.2: Uncertainties associated with measurement

Physical Quantity	Uncertainty in Measurement
Casing Radius(R_c)	$\pm 0.1\%$
Hub Radius (R_h)	$\pm 0.5\%$
Annular Height (Y_m)	$\pm 1\%$
Transverse position (y)	$\pm 0.05\text{mm}$
Divergence Angle(Θ)	$\pm 0.5\%$
Velocity (U)	$\pm 1.2\%$
Swirl angle(Φ)	$\pm 1.5\%$
Reynolds Number (Re)	$\pm 3\%$
Pressure Recovery Coefficient (C_p)	$\pm 5\%$
Total Pressure(P_t)	$\pm 1.2\%$
Static Pressure(P_s)	$\pm 1.5\%$
Dynamic head	$\pm 4.5\%$
Mean Velocity(\bar{U})	$\pm 2\%$
Atmospheric Pressure(P_{atm})	$\pm 1\%$

Chapter-4

4 Computational and Mathematical Formulation

The fluid flow in any system can be solved experimentally and computationally. The fluid flow simulation on the computer is more appropriate for considering experimental boundary conditions and different geometric variables. Very complex or idealized boundary conditions can be simulated, and it gives accurate results for each cell of the fluid domain by solving the governing equations. Thus, accessing the flow fields at various nodal points in the domain is very difficult to incorporate into an experiment. In the past ten years, there has been a marvelous improvement in the field of numerical techniques, which has had a significant impact on the evaluation of complex fluid problems and achieve better solutions.

Computational Fluid Dynamics (CFD) is the process of solving a set of governing equations for a fluid flow problem using a numerical method. The basic step in a computational process is the discretization of the computational domain into finite control volumes. The mass and momentum conservation laws, as well as certain extra equations for turbulence models, are utilized to solve the fluid flow phenomena. The momentum equations are used to solve for the velocity component of flow. However, calculating the velocity component in an unidentified flow field is a tough problem. The pressure gradient term is a component of the momentum equation's main term. Numerous methods have been used to calculate the pressure from the governing equation. *Fluent* is the computational software that uses the CFD method to solve fluid flow problems. *Fluent* was utilized to give a computational solution to a complex problem through the use of modelling. In the *Fluent* module, the SIMPLE scheme is

adopted. The algorithm pressure field's solution is initially found, and the corresponding velocity component is calculated using the momentum equation. The present research analyses the flow behaviour in an annular diffuser with and without inlet swirl flow by numerically solving the problem using a series of algorithms.

The chapter presents the details of computational and mathematical formulations being considered for modelling and simulation procedures of the problem.

4.1 Mathematical Formulation

The turbulent flow's numerical solution is determined by the magnitudes of the Reynolds numbers. It is well known that the fluctuating velocity fields that characterize turbulent flows. These fluid domains are made up of transported quantities, such as momentum, energy, and species concentration, which fluctuate. The simulation of practical engineering problems calculations is very expensive computationally since the fluctuations of fluid are very high frequency and small scale. Rather than that, the instantaneous governing equations can be time average, ensemble averaged, and some variables altered to eliminate small scales, yielding less expensive computing solutions. However, the altered governing equations include new unknown flow constants. These variable terms are the known quantities used in turbulence models.

The set of governing equations, which includes mass and momentum conservation, is solved using *Fluent*. When the fluid flow is turbulent, the fluid problem is solved using an additional set of transport equations. The following equations apply to two-dimensional axisymmetric geometries:

Mass Conservation Equation

The mass equation is conserved in the following manner:

$$\frac{\partial \rho}{\partial t} + \nabla \cdot (\rho \vec{v}) = 0 \quad (4.1)$$

Equation 4.1 is in its simplest form. It applies to compressible as well as incompressible fluids.

For two-dimensional axisymmetric geometry, the continuity equation is as follows (Equation 4.2):

$$\frac{\partial}{\partial x}(\rho v_x) + \frac{\partial}{\partial r}(\rho v_r) + \frac{\rho v_r}{r} = s_m \quad (4.2)$$

Where V_x and V_r are the axial and radial velocity, respectively.

Conservation of Momentum Equations

The conservation of momentum equations of the inertial reference frame in two-dimensional geometries can be stated as (Equations 4.3-4.4):

$$\begin{aligned} & \frac{1}{r} \frac{\partial}{\partial x}(r \rho v_x v_x) + \frac{1}{r} \frac{\partial}{\partial r}(r \rho v_r v_x) = \\ & -\frac{\partial p}{\partial x} + \frac{1}{r} \frac{\partial}{\partial x} \left[r \mu \left(2 \frac{\partial v_x}{\partial x} - \frac{2}{3} (\nabla \cdot \vec{v}) \right) \right] + \frac{1}{r} \frac{\partial}{\partial r} \left[r \mu \left(\frac{\partial v_x}{\partial r} + \frac{\partial v_r}{\partial x} \right) \right] + F_x \end{aligned} \quad (4.3)$$

And

$$\begin{aligned} & \frac{1}{r} \frac{\partial}{\partial x}(r \rho v_x v_r) + \frac{1}{r} \frac{\partial}{\partial r}(r \rho v_r v_r) = \\ & -\frac{\partial p}{\partial r} + \frac{1}{r} \frac{\partial}{\partial x} \left[r \mu \left(\frac{\partial v_r}{\partial x} + \frac{\partial v_x}{\partial r} \right) \right] + \frac{1}{r} \frac{\partial}{\partial r} \left[r \mu \left(2 \frac{\partial v_r}{\partial r} - \frac{2}{3} (\nabla \cdot \vec{v}) \right) \right] \\ & -2\mu \frac{v_r}{r^2} + \frac{2}{3} \frac{\mu}{r} (\nabla \cdot \vec{v}) + \rho \frac{v_z^2}{r} + F_r \end{aligned} \quad (4.4)$$

Where

$$\nabla \cdot \vec{v} = \frac{\partial v_x}{\partial x} + \frac{\partial v_r}{\partial r} + \frac{v_r}{r} \quad (4.5)$$

The tangential momentum equation for swirling flows needs to be solved, which can be written as (Equation 4.6):

$$\frac{1}{r} \frac{\partial}{\partial x} (r \rho v_x v_z) + \frac{1}{r} \frac{\partial}{\partial r} (r \rho v_r v_z) = \frac{1}{r} \frac{\partial}{\partial x} \left[r \mu \frac{\partial v_z}{\partial x} \right] + \frac{1}{r^2} \frac{\partial}{\partial r} \left[r^3 \mu \frac{\partial}{\partial r} \left(\frac{v_z}{r} \right) \right] - \rho \frac{v_r v_z}{r} \quad (4.6)$$

4.2 Turbulence Modelling

The fluid flow around the daily life in which we encounter is turbulent. Turbulence is characterized by instability in a fluid that causes rapid fluctuations in velocity about its mean value. Turbulent flows have characteristic structures present within them. The turbulent flow is irregular, random, and chaotic. In terms of time and space, transport quantities, such as mass, momentum, and scalar species change, the aperiodic motion of the flow. The energy is derived from the core stream by the largest eddies of the turbulent stream. The transitions of energy are from the biggest eddies to the smallest eddies. Then again, the transfer of turbulent energy from small eddies into the internal energy by the viscous dissipation effect. The average results were taken from modelling of the turbulence transport mechanism. Turbulence modelling is to specify the additional conditions to close the Reynolds-Averaged Navier-Stokes (RANS) equations. The RANS equation governs the transport flow quantity in average terms and the turbulence model is modelled at the whole range of scale. RANS based turbulence modelling significantly reduces the computational effort and resources.

Selection of Turbulence Model

In computational fluid dynamics, various types of turbulence models are available. Each model has its capabilities in specific domains to solve the problem. So, it is a very complicated process to select a single model that is universally accepted and gives the optimal solution for a class of problems. The selection of turbulence models is influenced by factors such as flow types, specific concerns about fluid problems, accuracy requirements, computational resource types, and the time required to solve the

problems, among others. Based on these observations, select the most appropriate model as per your practical application and give the solution to that problem.

The turbulence models are broadly categorized as:

1. Zero equation model (Algebraic model)
2. One equation model
3. Two equation model
4. Reynolds stress model

In the current work, the flow characteristics of an annular diffuser are predicted using two-equation turbulence models. This choice is based on a literature review where two-equation turbulence models were found to be superior to other models. Two-equation turbulence models are further subdivided into specific models, for example:

1. Standard $k-\varepsilon$
2. RNG $k-\varepsilon$
3. Realizable $k-\varepsilon$
4. Standard $k-\omega$
5. SST $k-\omega$

To identify the correct turbulence models are tested for the current research work. These models are described briefly in the following section.

4.2.1 Standard $k-\varepsilon$ Turbulence Model

The Standard $k-\varepsilon$ turbulence model was proposed by Launder & Spalding (1974), and since then it has become one of the most popular turbulence model employed to study a large number of practical fluid flow problems. This is largely due to its efficient nature, where it can handle diverse flow problems with reasonable accuracy and at an economical cost.

The evolution equation of turbulent kinetic energy (k) is derived from the exact form, whereas the evolution equation of turbulent dissipation energy (ε) is derived from physical reasoning. The transport equations for turbulent kinetic energy (k) and turbulent dissipation energy (ε) are Equations 4.7 and 4.8, respectively.

$$\frac{\partial}{\partial t}(\rho k) + \frac{\partial}{\partial x_i}(\rho k u_i) = \frac{\partial}{\partial x_j} \left[\left(\mu + \frac{\mu_t}{\sigma_k} \right) \frac{\partial k}{\partial x_j} \right] + G_k + G_b - \rho \varepsilon - Y_M + S_k \quad (4.7)$$

And

$$\frac{\partial}{\partial t}(\rho \varepsilon) + \frac{\partial}{\partial x_i}(\rho \varepsilon u_i) = \frac{\partial}{\partial x_j} \left[\left(\mu + \frac{\mu_t}{\sigma_\varepsilon} \right) \frac{\partial \varepsilon}{\partial x_j} \right] + C_{1\varepsilon} \frac{\varepsilon}{k} (G_k + C_{3\varepsilon} G_b) - C_{2\varepsilon} \frac{\varepsilon^2}{k} + S_\varepsilon \quad (4.8)$$

S_k and S_ε are user-defined source terms. σ_k and σ_ε are the turbulent Prandtl numbers for k and ε , respectively. C_{1k} and $C_{2\varepsilon}$ are model constants that are obtained through experiments on canonical flows such as decaying isotropic turbulence and homogeneous shear flow cases.

The turbulent viscosity μ_t in a standard k - ε turbulence model is calculated using the following Equation 4.9:

$$\mu_t = \rho C_\mu \frac{k^2}{\varepsilon} \quad (4.9)$$

The values of the model constants as per the literature are:

$$C_{1\varepsilon} = 1.44; C_{2\varepsilon} = 1.92; C_\mu = 0.09; \sigma_k = 1.0; \sigma_\varepsilon = 1.3$$

4.2.2 RNG k - ε Turbulence Model

Yakhot and Orszag (1986) proposed the RNG k - ε turbulence model, which is derived from the instantaneous Navier-Stokes equations and uses the mathematical technique known as the RNG method. The constants used in this model differ from those used in the standard k - ε turbulence model, resulting in new transport equations for k and ε . The RNG model accounts for the effect of swirl flow and enhances the accuracy of swirl

flow. The appropriate wall treatment is taken into account, and an analytically derived differential formula is used to calculate turbulent viscosity for low Reynolds numbers. As a result, the RNG K - ε turbulence model accurately measures the swirl flow and is more reliable than the standard K - ε turbulence model.

Equations 4.10 and 4.11 are the transport equations of k and ε respectively:

$$\frac{\partial}{\partial t}(\rho k) + \frac{\partial}{\partial x_i}(\rho k u_i) = \frac{\partial}{\partial x_j} \left(\alpha_k \mu_{eff} \frac{\partial k}{\partial x_j} \right) + G_k + G_b - \rho \varepsilon - Y_M + S_k \quad (4.10)$$

$$\frac{\partial}{\partial t}(\rho \varepsilon) + \frac{\partial}{\partial x_i}(\rho \varepsilon u_i) = \frac{\partial}{\partial x_j} \left(\alpha_\varepsilon \mu_{eff} \frac{\partial \varepsilon}{\partial x_j} \right) + C_{1\varepsilon} \frac{\varepsilon}{k} (G_k + C_{3\varepsilon} G_b) - C_{2\varepsilon} \rho \frac{\varepsilon^2}{k} - R_\varepsilon + S_\varepsilon \quad (4.11)$$

Here, G_k and G_b represent the generation of turbulent kinetic energy that arises due to mean velocity gradients and buoyancy respectively. Y_M denotes the fluctuating dilation incompressible turbulence that contributes to the overall dissipation rate. α_k and α_ε are inverse effective Prandtl numbers for the k and ε respectively.

The effective viscosity of the RNG theory is described in the following Equation 4.12:

$$d \left(\frac{\rho^2 k}{\sqrt{\varepsilon \mu}} \right) = 1.72 \frac{\hat{v}}{\sqrt{\hat{v}^3 - 1 + C_v}} d\hat{v} \quad (4.12)$$

Where

$$\hat{v} = \frac{\mu_{eff}}{\mu}$$

$$C_{\hat{v}} \approx 100$$

The effective viscosity for turbulent transport is above defined for the low Reynolds number and accurately measures the results near the wall. The effective viscosity of the high Reynolds numbers is described in the following Equation 4.13:

$$\mu_t = \rho C_\mu \frac{k^2}{\varepsilon} \quad (4.13)$$

The value of the model constants as per the literature are:

$$C_\mu = 0.0845, C_{I\varepsilon} = 1.42, C_{2\varepsilon} = 1.68$$

4.2.3 Realizable k - ε Turbulence Model

Shih et al. (1995) proposed a realizable k - ε turbulence model with transport equations based on turbulent kinetic energy (k) and turbulent dissipation energy (ε). In the realizable k - ε turbulence model, the transport equation for ε is obtained from the exact transport equation of the mean-square vorticity fluctuation, unlike in the standard k - ε turbulence model where the equation was based on physical reasoning. Also, the turbulent viscosity μ_t in the realizable k - ε turbulence model has the same formulation as given in Equation 4.14 but the factor C_μ is not constant. It is computed as:

$$C_\mu = \frac{1}{A_0 + A_s \frac{kU^*}{\varepsilon}} \quad (4.14)$$

$$U^* = \sqrt{S_{ij}S_{ij} + \widehat{\Omega}_{ij}\widehat{\Omega}_{ij}}$$

Equation 4.15 and Equation 4.16 are the transport equations for k and ε , respectively:

$$\frac{\partial}{\partial t}(\rho k) + \frac{\partial}{\partial x_i}(\rho k u_j) = \frac{\partial}{\partial x_i} \left[\left(\mu + \frac{\mu_t}{\sigma_k} \right) \frac{\partial k}{\partial x_j} \right] + G_k + G_b - \rho \varepsilon - Y_M + S_k \quad (4.15)$$

$$\begin{aligned} \frac{\partial}{\partial t}(\rho \varepsilon) + \frac{\partial}{\partial x_j}(\rho \varepsilon u_j) &= \frac{\partial}{\partial x_j} \left[\left(\mu + \frac{\mu_t}{\sigma_\varepsilon} \right) \frac{\partial \varepsilon}{\partial x_j} \right] \\ + \rho C_{1\varepsilon} S \varepsilon - \rho C_2 \frac{\varepsilon^2}{k + \sqrt{\nu \varepsilon}} + C_{1\varepsilon} \frac{\varepsilon}{k} C_{3\varepsilon} + G_b + S_\varepsilon \end{aligned} \quad (4.16)$$

Where

$$C_1 = \max \left[0.43, \frac{\eta}{\eta + 5} \right] \quad \eta = S \frac{k}{\varepsilon}$$

The values of the other model constants as per the literature are:

$$C_{1\varepsilon} = 1.44; C_{2\varepsilon} = 1.9; \sigma_k = 1.0; \sigma_\varepsilon = 1.2$$

4.2.4 Standard k - ω Model

The standard k - ω model was proposed by Wilcox (1998); it shows a better formulation of low Reynolds number, compressibility effects, and more accuracy near the wall regions. The turbulent kinetic energy (k) and specific dissipation rate (ω) are used to calculate the transport equations. The Shear Stress Transport modification, k - ω is widely used to solve practical applications in industry and research codes. Equation 4.17 and Equation 4.18 are the transport equations for k and ω , respectively;

$$\frac{\partial}{\partial t}(\rho k) + \frac{\partial}{\partial x_i}(\rho k u_i) = \frac{\partial}{\partial x_j} \left[\left(\mu + \frac{\mu_t}{\sigma_k} \right) \frac{\partial k}{\partial x_j} \right] + G_k - Y_k + S_k \quad (4.17)$$

and

$$\frac{\partial}{\partial t}(\rho \omega) + \frac{\partial}{\partial x_i}(\rho \omega u_i) = \frac{\partial}{\partial x_j} \left[\left(\mu + \frac{\mu_t}{\sigma_\omega} \right) \frac{\partial \omega}{\partial x_j} \right] + G_\omega - Y_\omega + S_\omega \quad (4.18)$$

Where, G_k and G_ω represent the generation of k and ω due to mean velocity gradients.

Y_k and Y_ω represent the dissipation of respective variables due to turbulence.

The following Equation 4.19 is used to calculate turbulent viscosity μ_t :

$$\mu_t = \alpha^* \frac{\rho k}{\omega} \quad (4.19)$$

Where α^* represents the low Reynolds number correction, its value can be computed.

4.2.5 Shear-Stress Transport (SST) k - ω Model

SST k - ω turbulence model was proposed by Menter (1994) and like the other two turbulence models, has two transport equations (i) turbulent kinetic energy (k) and (ii) specific dissipation rate (ω). It is a combination of Standard k - ω and Standard k - ε models where a blending function activates one model over the other based on the wall

distance. In the near-wall region, the Standard $k-\omega$ model is active, while in the free stream area, the Standard $k-\varepsilon$ model is active.

Equation 4.20 and Equation 4.21 are the transport equations for k and ω , respectively:

$$\frac{\partial}{\partial t}(\rho k) + \frac{\partial}{\partial x_i}(\rho k u_i) = \frac{\partial}{\partial x_j} \left[\left(\mu + \frac{\mu_t}{\sigma_k} \right) \frac{\partial k}{\partial x_j} \right] + G_k - Y_k + S_k \quad (4.20)$$

$$\frac{\partial}{\partial t}(\rho \omega) + \frac{\partial}{\partial x_i}(\rho \omega u_i) = \frac{\partial}{\partial x_j} \left[\left(\mu + \frac{\mu_t}{\sigma_\omega} \right) \frac{\partial \omega}{\partial x_j} \right] + G_\omega - Y_\omega + D_\omega + S_\omega \quad (4.21)$$

Where G_k and G_ω represent the generation of k and ω due to mean velocity gradients.

Y_k and Y_ω denote the dissipation due to turbulence of k and ω , respectively. D_ω denotes the cross-diffusion term.

The following Equation 4.22 is used to calculate turbulent viscosity μ_t :

$$\mu_t = \frac{\rho k}{\omega} \frac{1}{\max \left[\frac{1}{\alpha^*}, \frac{\Omega F_2}{a_1 \omega} \right]} \quad (4.22)$$

$$\Omega = \sqrt{2\Omega_{ij}\Omega_{ij}}$$

Ω_{ij} represents the mean rate of rotation tensor.

4.3 CFD Analysis Procedure

The *ANSYS Fluent* 16 version software is used for simulation. The software is used as a simulator and a real-time analyzer for the analysis of fluid and heat flow in fluid dynamics. The overall steps used in the CFD technique are as follows.

4.3.1 Pre-processor

Creation of Geometry In the *Fluent* module's workbench, the two-dimensional geometry of the annular diffuser was created.

The geometry of the diffuser is properly generated as per the geometrical specification of the test diffuser (Figure 4.1).

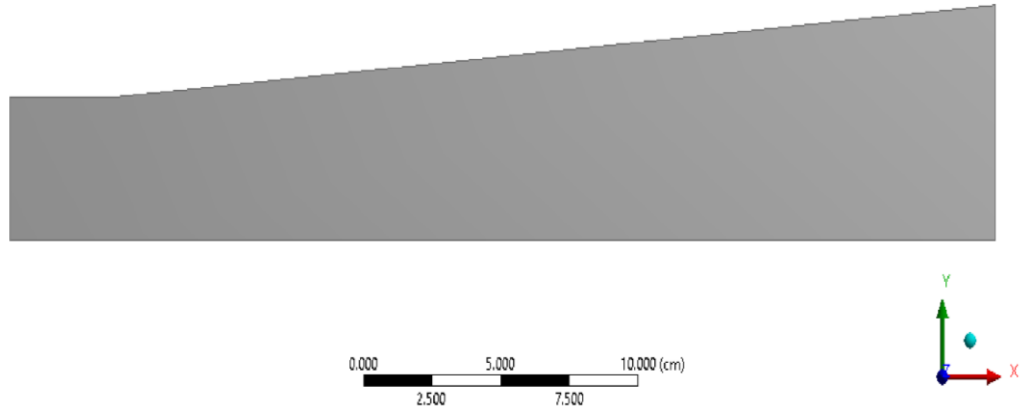


Figure 4.1: The annular diffuser's two-dimensional geometry.

Wall Treatment

A typical near-wall region on any surface is shown in Figure 4.2. It is broadly divided into two layers (i) inner layer, and (ii) outer layer. The inner layer is further classified into three layers: (i) viscous sub-layer ($y^+ < 5$), (ii) buffer layer ($5 < y^+ < 30$), and (iii) log-law region ($30 < y^+ < 300$). These regions are also identified with y^+ values (Figure 4.2), which is defined as;

$$y^+ = \frac{\rho u_T \Delta y}{\mu}$$

$$u_T = \sqrt{\frac{T_w}{\rho}}$$

Here, Δy represents the first cell height from the wall, u_T is the wall shear stress. In this region, the flow variables have large gradients, which directly affect their transport properties. In order to obtain accurate numerical solutions for a fluid flow problem, the

near-wall region needs to be adequately modelled. The treatment of the near-wall area varies as per the turbulence model under consideration.

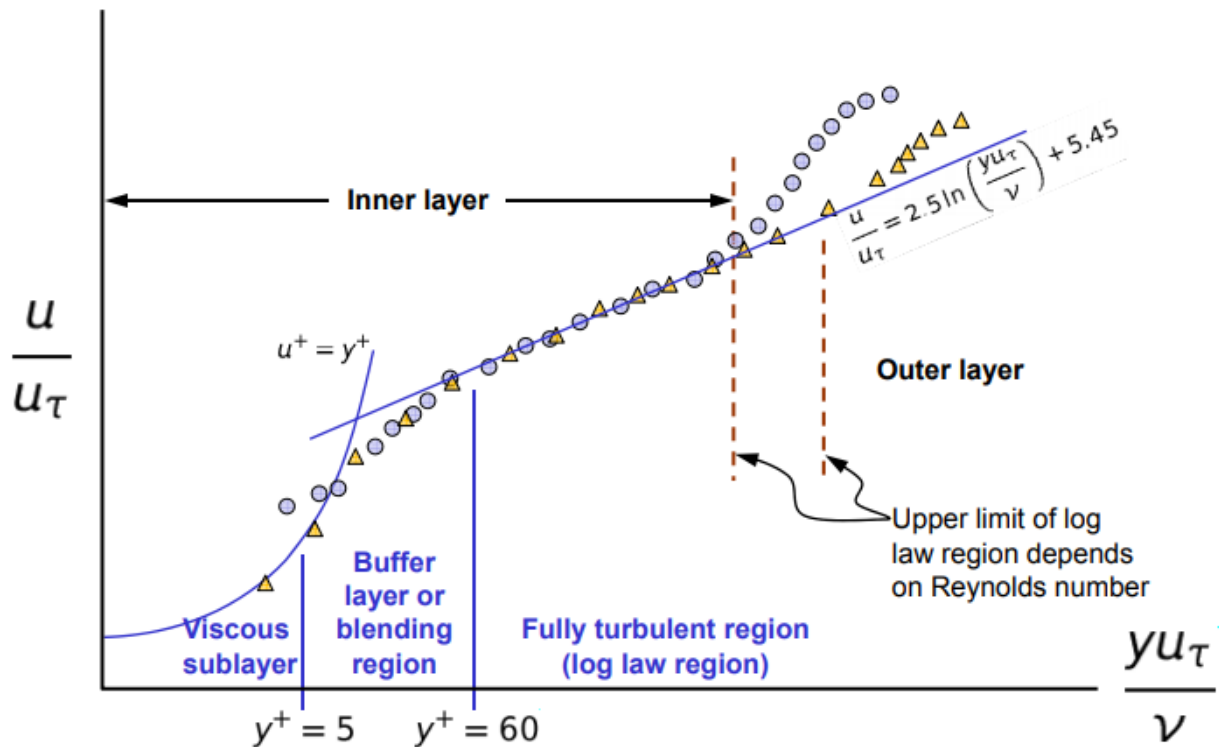


Figure 4.2: Near wall region (Source: ANSYS Academic Research *Fluent* (Release 15.0)).

Discretization

After the generation of the geometry of the CFD domain, the next step is to discretize the computational domain. Meshing is defined as dividing the flow domain into a large number of computational cells. That means discretization of the domain. The number of cells in the finite control volume should be high. Adequate resolution is required to represent the geometry of the diffuser and the expected flow pattern is smooth in the control volume. The quadrilateral cell elements have been chosen with a structure mesh scheme selected for the analysis (Figure 4.3). The meshing quality of the geometry is controlled by the jacobian ratio, aspect ratio, wrap angle, and skewness of each cell. The aspect ratio value attained less than 50 in geometry, and distorted cells made an

angle of more than 45 on the sides of the cell. Near wall areas, a fine mesh is applied while maintaining $y^+ < 1$. The first mesh node is placed at a distance of 0.03 mm from the wall. Boundary layer meshing was employed near the hub and casing wall to capture the viscous sub-layer, velocity gradient, and separation of flow with a high level of accuracy. After mesh generation, the quality of the grid was checked in the *ANSYS Fluent* module.

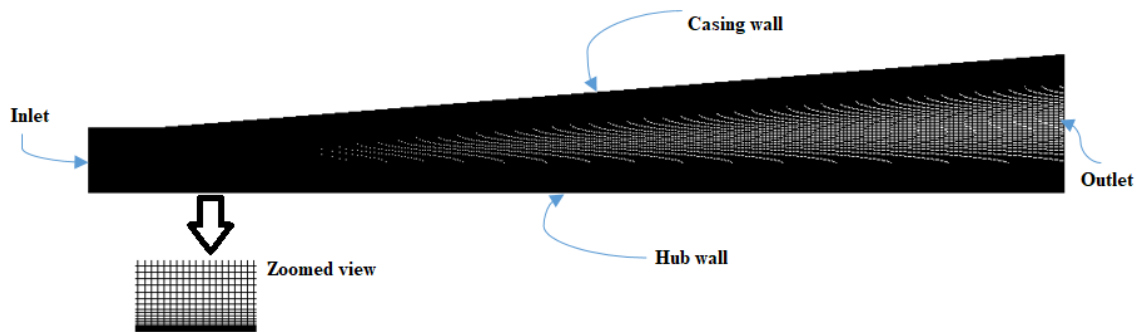


Figure 4.3: Meshed computational domain.

Boundary Name

After the mesh generation, the names of the boundaries are to be defined for the CFD domain. In the *ANSYS Fluent* module, a "Specify boundary name" function is used to create the boundary names. The *ANSYS* workbench can also be used to make mesh files for many different CFD codes. In the proposed work, the *Fluent 16* has been selected. It is also capable of being used in the *ANSYS* workbench environment. Figure 4.4 represents the different boundary names by color-coding used in the *ANSYS* workbench.

- Inlet
- Casing Wall
- Hub Wall
- Outlet

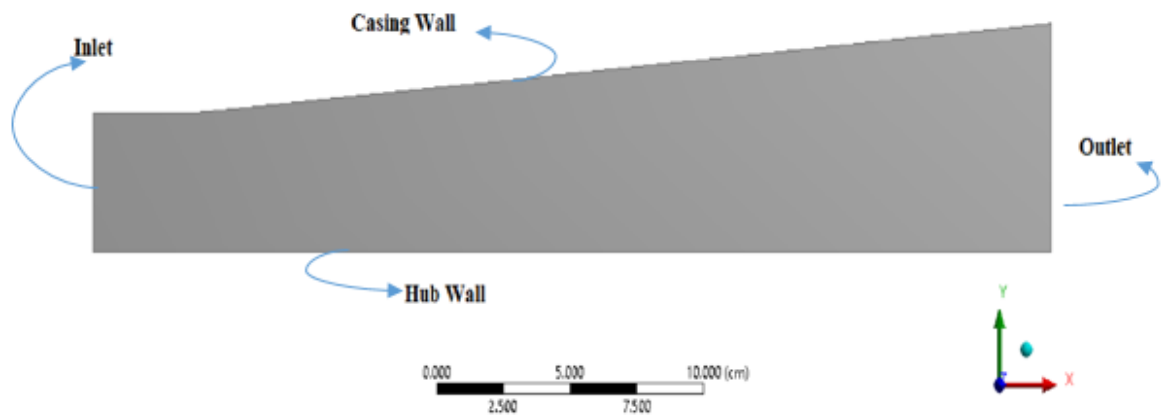


Figure 4.4: 2D axisymmetric annular diffuser.

4.3.2 Solver

The finite volume technique (FVM) is applied to the discretized computational domain of the governing equations (Equation 4.1-4.6), resulting in a set of algebraic equations for turbulent kinetic energy (k) and specific dissipation rate (ϵ). By selecting the appropriate boundary conditions, all of these equations are solved. The solver is used as a default under-relaxation factor to start a calculation. The pressure-based solver's iterative process is stabilized by under-relaxation. The problem is a general set under the axisymmetric swirl and absolute velocity formulation with steady-state conditions.

Boundary Conditions

After generation of the mesh of the diffuser geometry, we have defined the different boundaries on the surface of the axial diffuser and the region of fluid flow, which is described as follows:

- a) Inlet-Velocity profile
- b) Outlet-Pressure
- c) Hub wall
- d) Casing wall
- e) Fluid flow domain

The axial diffuser fluid flow problem is solved with various operating conditions and boundary conditions. In the current research work, the RNG $K-\varepsilon$ model was adopted to find the best results. The various boundary conditions have been chosen, which are described as follows:

Boundary condition at the inlet

In the current problem, the axial velocity with swirl flow is applied at the inlet of the boundary conditions. The velocity specification with the component method and absolute reference frame was chosen at the inlet of the boundary. The fluid flow with swirl has two components, i.e. tangential velocity, and axial velocity. The tangential velocity has been calculated based on the inlet swirl angle. The present problem is solved with inlet swirl angles of 0° , 7.5° , 12° , 17° , and 25° . The value of turbulence intensity is calculated as $I = 0.16(R_{eDH})^{-1/8} \times 100$. Here, R_{eDH} represents the Reynolds number on the basis of the hydraulic diameter at the inlet. At the inlet, a different axial and swirl velocity profile is inserted with a turbulence intensity of 3%.

Boundary condition at the outlet

The atmospheric pressure condition is used at the boundary condition's exit. The backflow direction specification method has been selected with a normal to the boundary of the outlet section. The backflow turbulence intensity of 3% and the backflow hydraulic diameter are specified based on the axial diffuser's geometrical design.

Boundary condition at the Wall

In the present fluid flow problem, the walls are stationary not moving, so the fluid velocity is zero. The no-slip in the shear section specifies the boundary conditions at the hub and casing walls. The wall roughness affects the heat & mass transfer and drag force on the walls. The wall roughness effects are considered and its value is calculated

based on a modified law of the wall for roughness. The roughness height (0) and roughness constant (0.5) values are assigned in the boundary condition's wall roughness section.

Solution Methods

The Navier-Stokes governing equations for mass and momentum are discretized using the finite volume method. Under pressure velocity coupling, the SIMPLE algorithm is used to solve the pressure correction equation iteratively until the solution converges. A 2nd order upwind discretization scheme is adopted under spatial discretization for pressure, momentum, swirl velocity, turbulent kinetic energy (k), and turbulent dissipation energy (ε) while a first-order upwind discretization scheme is selected for discretizing volume fraction. These schemes ensure satisfactory accuracy, stability, and convergence.

The discretization scheme defines that how the solver calculating gradients and interpolates variables to non-stored locations. The default schemes are generally more suitable but less accurate than other schemes.

Convergence criteria

The *Fluent* 16 software reports the values of residuals. The values are indications of the error in the current solution, so these residuals should be decreased during the calculation. There are various methods available for the reduction of residuals that are helpful for getting a solution to a given problem. The residuals are reduced on the basis of their convergence criteria and the reduced residuals are known as "converged residuals" (Figure 4.5). There is a need to set the convergence criteria for the iterative method. Generally, two iteration levels are used to solve the computational domain. In the first level iteration, linear equations are solved, and the second level iteration is used

to solve non-linear and coupled equations. From both the efficiency and accuracy point of view, the decision to stop each level's iteration process is important.

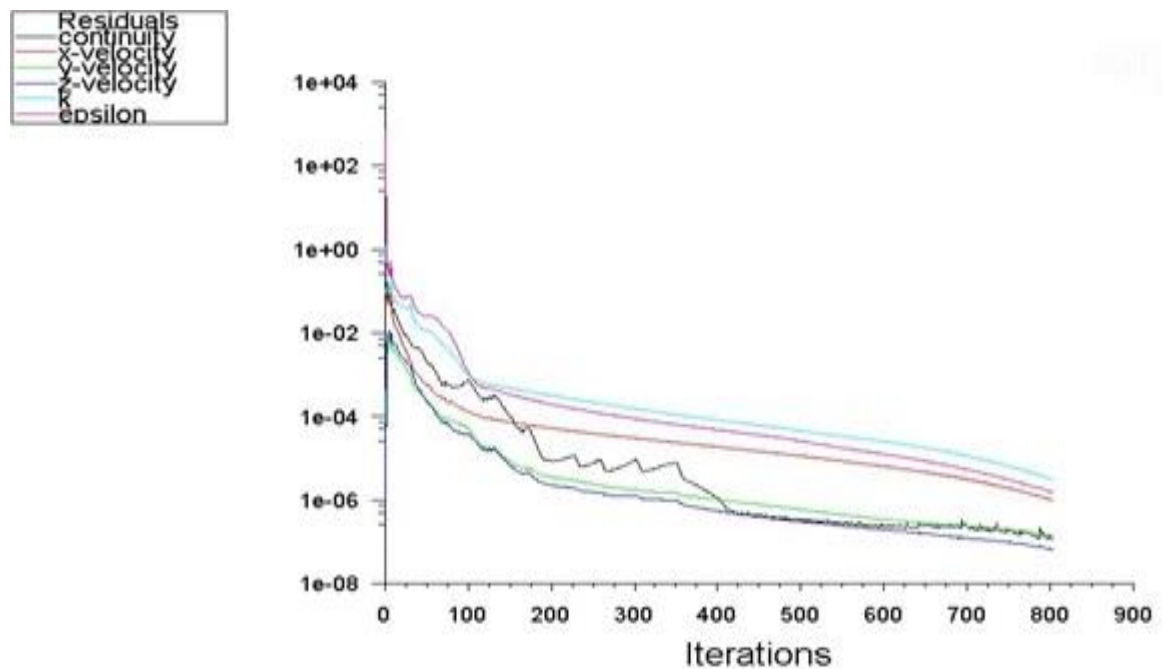


Figure 4.5: Iteration process for a convergence.

For example, suppose the solution of the discretized equations is likely to correct the solution of the differential as the grid spacing tends to be zero. In that case, the numerical is said to be convergent. The convergence criterion is around 1×10^{-6} for residual variables. The results are stable for the present problem.

4.3.3 Post-processor

The final results are shown in the *Fluent Post*. The *ANSYS Fluent* post processor is used to analyze and visualize the obtained results from the analysis. With the help of various functions available in the *ANSYS Fluent-Post*, the data can be utilized to calculate various parameters like velocity, pressure, maximum/minimum values of various quantities like coefficient of pressure etc. The other CFD-Post properties are that they present the results in different forms, i.e. tabulated presentation, chart plotting, and special turbo-machinery functionality, and automatic report generation. The *ANSYS*

Fluent post solution shows the results virtually and there are many possibilities for presenting the results.

4.4 Procedure of Simulation

Pre-processor

- ❖ The 2 D geometry of the diffuser is created on the *Fluent* workbench as per the geometrical design.
- ❖ The boundary layer meshing is generated at the hub and the casing walls with $y^+ < 1$ and 15 inflation layers with growth factor 1.1.
- ❖ The axisymmetric geometry of the annular diffuser has been meshed with quadratic meshing. The mesh size is 0.07 cm and the mesh elements range from 150000-175000.
- ❖ Assign the names of the boundaries, i.e. inlet, hub wall, casing wall, and outlet.

Solver

- ❖ The quality of the meshing was checked in the report quality.
- ❖ Pressure based, steady, and axisymmetric swirl solvers were chosen in the post processing of the general section.
- ❖ In the solver, the standard wall function with the RNG $K-\varepsilon$ turbulence model was chosen.
- ❖ Fluid medium air was chosen and assigned its properties.
- ❖ Axial velocity and swirl velocity profiles were specified in the boundary conditions at the inlet.
- ❖ The intensity and hydraulic diameter were specified based on equivalent flow diameter in the turbulence section.

- ❖ Atmospheric pressure was specified at the exit section of the boundary condition with backflow intensity and hydraulic diameter.
- ❖ In the solution methods, the SIMPLE scheme was chosen to solve the continuity and momentum equations.
- ❖ The absolute convergence criteria of 10^{-6} have been taken.
- ❖ A standard initialization method with an absolute reference frame was selected to initialize the problem.

Post processor

- ❖ After converged the problem, check the results and plot the velocity and pressure contours.
- ❖ Generate a report of the results.

Chapter-5

5 Validation

The two-dimensional axisymmetric boundary layer means flow quantities used in the axial annular diffusers. The swirling and non-swirling flows with different inlet conditions obtain detailed performance data from the experimental and computational methods that have been described in the earlier chapters. The correlation between the two techniques and validation of results needs to be assessed for analyzing the results and their further investigation. This chapter deals with the grid independence study and validates the computational results using experimental results. The comparison has been carried out based on optimum mesh size, selecting the best turbulence model, and numerical results obtained from the simulation's proximity to the experimental finding about velocity profiles and static pressure recovery coefficients.

5.1 Grid Independence Study

Meshing is a process that decreases the degree of freedom into the finite amount of cells of the computational domain. Nodes, cells, or grids are used in geometry discretization. The grid influences the convergence, accuracy, and speed of the simulation. The two-dimensional meshing is created in the diffuser geometry with the *Fluent* module in *ANSYS*. The accuracy of the results is determined by the meshing of any computational model.

The mesh's shape and size are critical in determining the best diffuser geometry results. A large mesh size reduces the quantity of elements in the geometry, resulting in a coarse mesh that does not produce accurate results. Then, it increases the quantity of elements by reducing the size, i.e. finer mesh, which gives better results than coarse mesh. Computational time and convergence of the solution time increase enormously with the

finer mesh. As a result, optimization is required to achieve the optimal mesh size to obtain accurate results in a short amount of time.

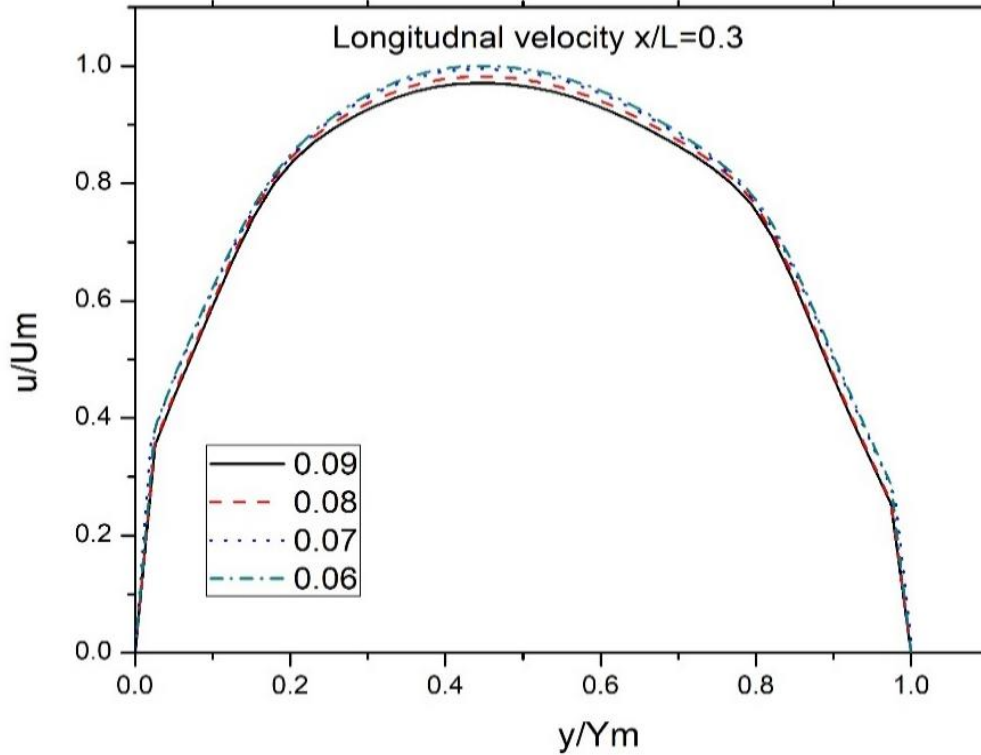


Figure 5.1: Grid refinement study of the longitudinal velocity profile with an inlet swirl angle of 0° at $x/L = 0.3$ for PHDC diffuser equivalent cone angle of 15° and $AR = 2$.

In the current study, a grid independence study was performed for several geometric designs with various turbulence models. One case of grid independence study is described in detail. The parallel hub axial annular diffuser whose casing is diverging on that experiment was performed. The inlet velocity profile is fed into the computational model, which was taken from the experimental setup. The simulation was performed on different mesh sizes, i.e. 0.09, 0.08, 0.07, and 0.06 cm, to examine the grid's sensitivity. The grid size depends on the diffuser's geometrical parameters, and the number of the grids will vary as per the geometrical dimension. The quadrilateral element has been chosen to discretize the complete geometry. Mesh sizes ranging from 0.06 to 0.09 cm were considered to evaluate the effect of element size on

the accuracy attained compared to experimental data and the amount of simulation time required to achieve the desired numerical solution.

Figure 5.1 depicts the longitudinal velocity profile of a parallel hub diverging casing (PHDC) diffuser with four mesh sizes with an inlet swirl angle of 0° at $x/L = 0.3$. The velocity profile results from mesh sizes of 0.07 and 0.06 cm have no significant differences from each other. The optimal mesh size gives accurate results with the consumption of less computational time. Hence, a 0.07 cm mesh size has been selected for the present study.

5.2 Validation of the CFD Methodology

Validation of the CFD methodology is an essential numerical study to establish the reliability of numerical results. This section compares the numerical findings of the simulations to experimental data. The numerical results produced using the five turbulence models (described in Section 5.1) are validated with the experimental data. Based on the available literature, five turbulence models were chosen (standard $k-\varepsilon$, RNG $k-\varepsilon$, Realizable $k-\varepsilon$, standard $k-\omega$, and SST $k-\omega$). Choose one of the five turbulence models that best match the experimental results. This exercise helps in determining the choice of turbulence model for future simulations.

All studies were conducted at a mean axial velocity of 60 m/s ($Re = 2.5 \times 10^5$) of the diffuser inlet equivalent diameter. The velocity profiles have been drawn at a particular transverse cross-section height, i.e. (y/Y_m). The casing position is represented as $y/Y_m = 1$, while the hub position is represented as $y/Y_m = 0$. The fully developed inlet velocity profile was acquired from the experimental setup of a PHDC diffuser with a cone angle of 15° and $AR = 2$ to investigate these models. Figures 5.2-5.5 show a comparison of velocity profiles and static pressure recovery coefficients with experimental data. The trend of the velocity profile for different planes is the same. The predicted and

experimental results of velocity profiles very well match each other at sections $x/L = 0.3-0.9$.

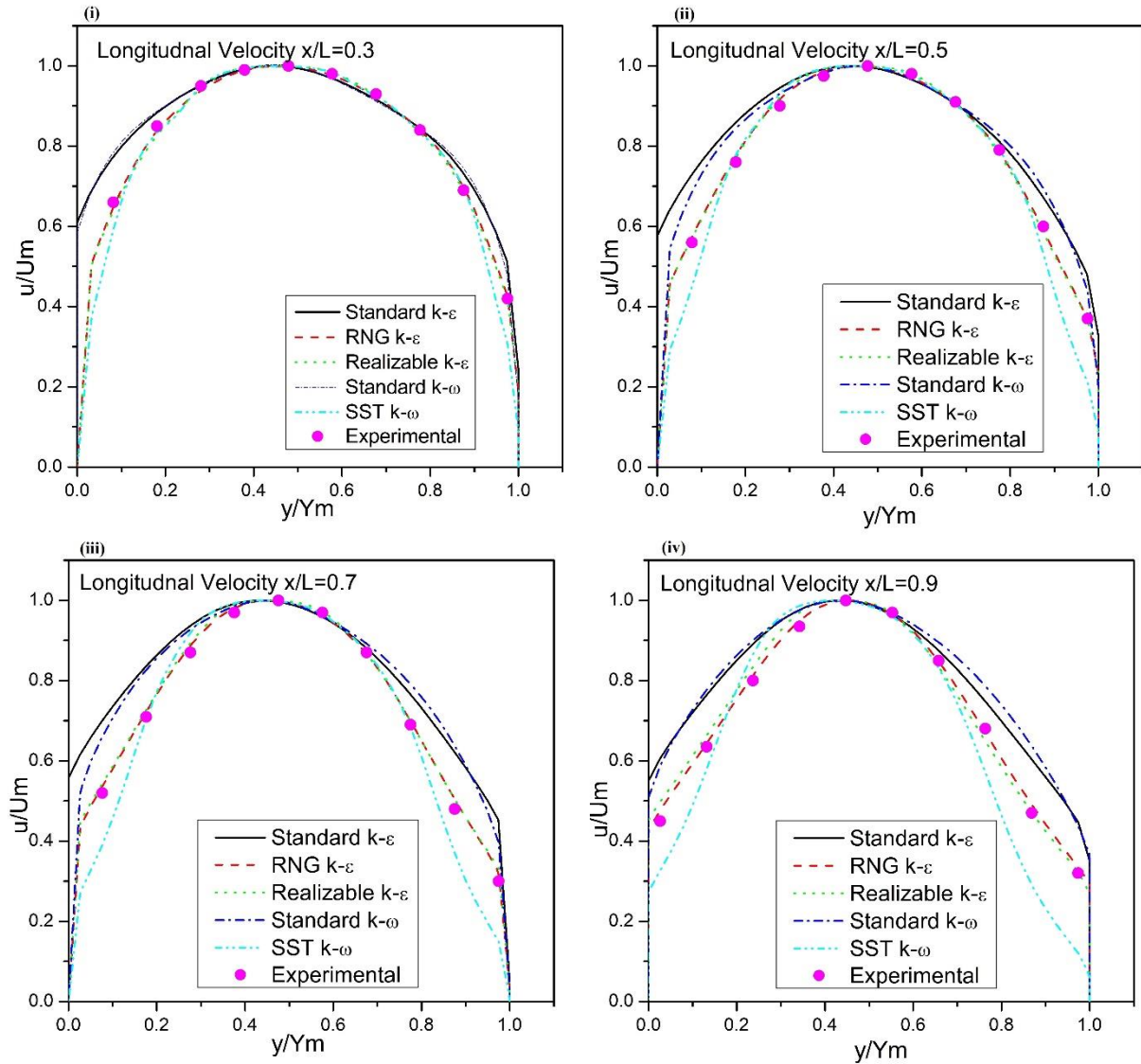


Figure 5.2: (i-v) Comparison of longitudinal velocity profiles with experimental results along the passage ($x/L = 0.3, 0.5, 0.7,$ and 0.9) for the PHDC diffuser with an equivalent cone angle of 15° at an inlet swirl angle of 0° ($AR = 2$).

The possible reason for the maximum deviation is the reduction of the core flow region, which is shifted towards the wall region, as well as a high shear layer of flow at the boundary. From the figures, it is apparent that the RNG $k-\epsilon$ turbulence model has the least deviations from the experimental results. As a result, to perform the current work

simulations, the RNG $k-\varepsilon$ turbulence model is used for swirl flow. The above-selected model was used to conduct additional research on the current work.

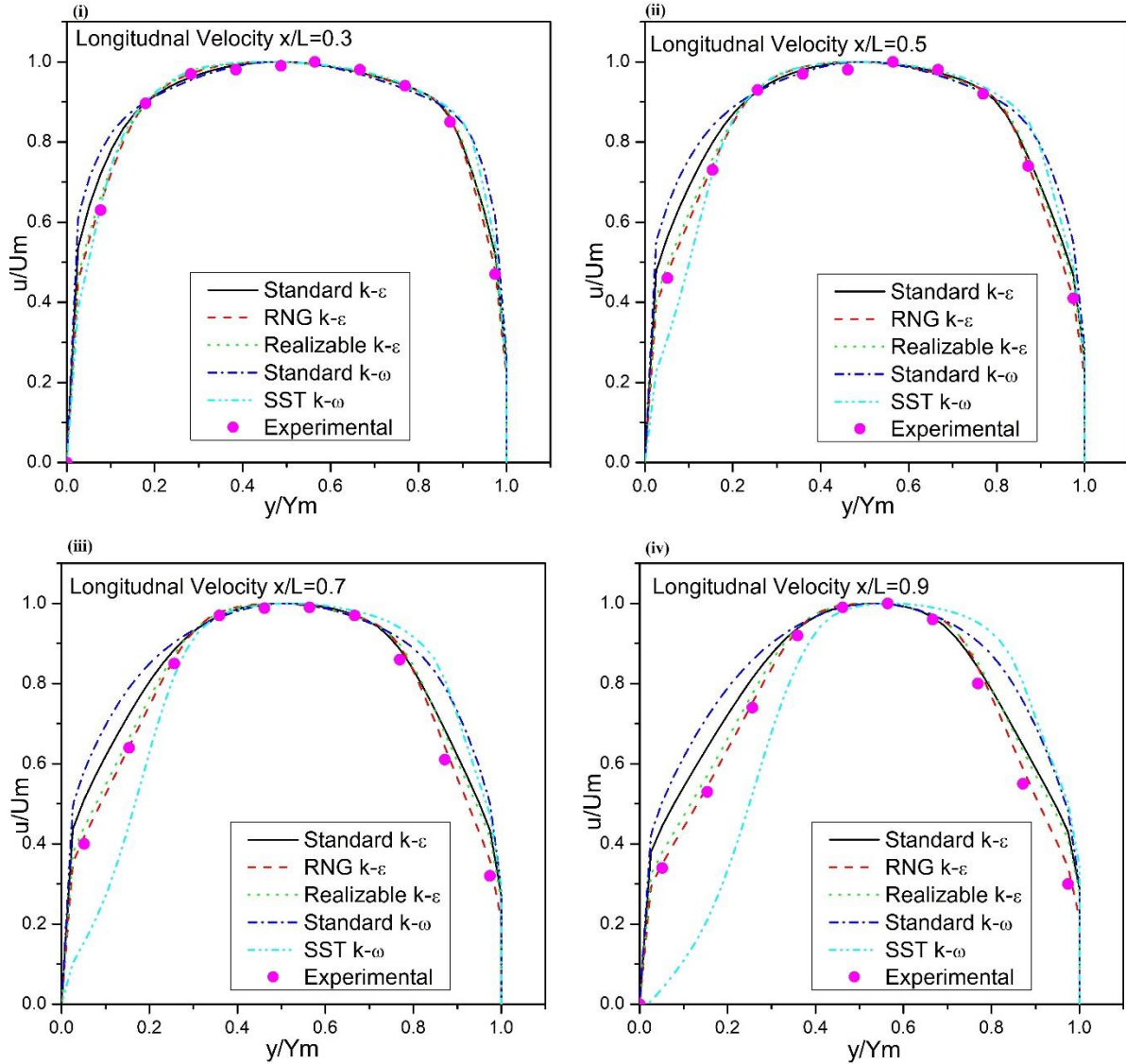


Figure 5.3: (i-v) Comparison of longitudinal velocity profiles with experimental results along the passage ($x/L = 0.3, 0.5, 0.7,$ and 0.9) for the PHDC diffuser with an equivalent cone angle of 15° at an inlet swirl angle of 12° ($AR = 2$).

5.3 Validation of Static Pressure Recovery Coefficient Profile

The flow development within the annular diffuser was studied using the five turbulence models. Figure 5.5 depicts the comparison of the static pressure recovery coefficient profile to the experimental results. The turbulence models validated the results obtained from the same design and validated them against the current experimental data, which

is very close. The standard $k-\omega$ shows the maximum deviation, while the RNG $k-\varepsilon$ better matches the swirl flow results in case of the PHDC diffuser.

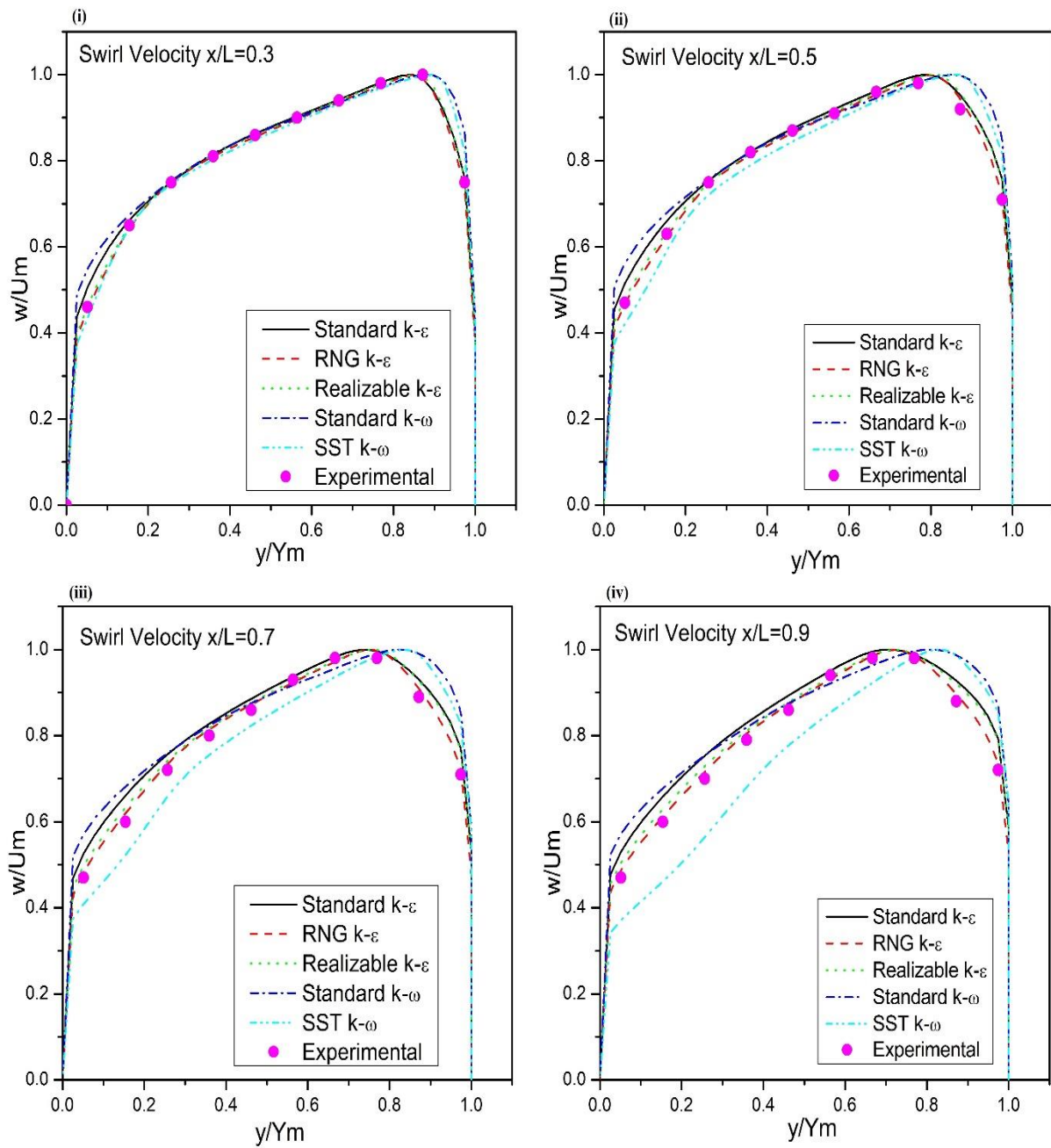


Figure 5.4: (i-v) Comparison of swirl velocity profiles with experimental results along the passage ($x/L = 0.3, 0.5, 0.7,$ and 0.9) for the PHDC diffuser with an equivalent cone angle of 15° at an inlet swirl angle of 12° ($AR = 2$).

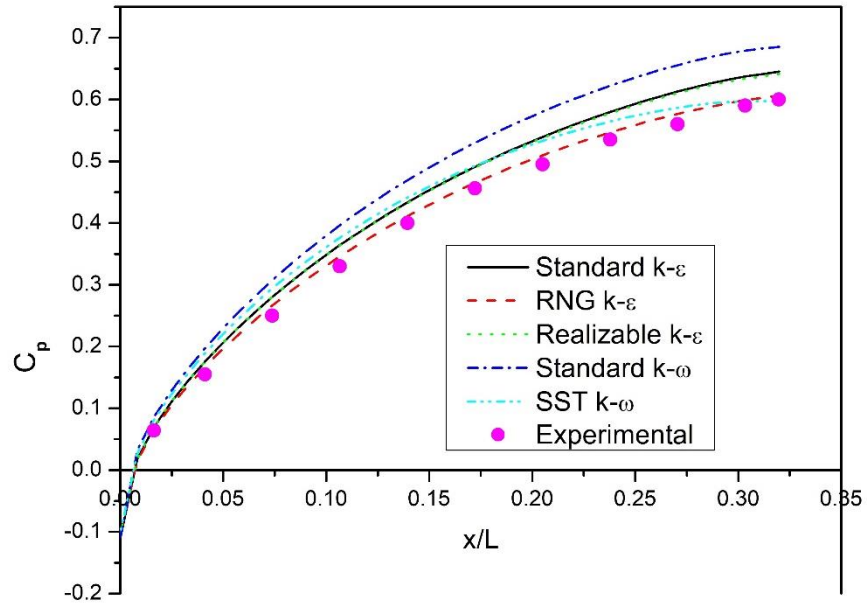


Figure 5.5: comparison of different turbulence models with experimental data of static pressure recovery coefficient at the casing wall of the PHDC diffuser with a cone angle of 15° at an inlet swirl angle of 12° ($AR = 2$).

Chapter-6

6 Computational Investigation: Effects of Casing Angle on the Performance of Parallel Hub Annular Diffusers

The current study aims to assess the performance of a parallel hub axial annular diffuser, which is used in gas turbine engines. Performance is measured using velocity profiles, static pressure recovery coefficients, total pressure loss coefficients, and effectiveness. The current work endeavors to investigate the new design of an annular diffuser capable of performing better than existing annular diffusers. The prime objective of the research is to recover maximum static pressure with swirl and non-swirl flow. The new design of the annular diffuser or design modification of the existing annular diffuser is an area of continuous research. Conducting experiments to evaluate their performance is a very costly as well as time-consuming process. Thus, CFD has become a suitable resource for doing such exercises. The results obtained from a parametric investigation using the CFD code *Fluent* are discussed in the current chapter.

6.1 Range of Parameters

Annular diffuser performance is influenced by several geometrical parameters, i.e. axial length (L), area ratio (AR), hub wall angle (θ_h), and casing wall angle (θ_c). In addition, the dynamic parameters of the fluid flow, i.e. inlet velocity profile, Reynolds number, and inlet swirl. Therefore, studying the impact of these parameters on casing wall angles ($3^\circ, 6^\circ, 9^\circ$), area ratios ($AR = 1.67, 2.48, 3.44$), and constant axial length ($L = 33.76$ cm) of the parallel hub axial annular diffuser. The annular diffuser's performance is evaluated at a Reynolds number of 2.5×10^5 with inlet swirls ($7.5^\circ, 12^\circ, 17^\circ, 25^\circ$) and non-swirl flow (0°).

The simulations were conducted on two-dimensional axisymmetric annular diffusers having different casing positions. The inlet velocity profiles for non-swirl and swirl flow obtained from the experimental setup were introduced in the *Fluent* software as the inlet boundary conditions. The geometric parameters and design of the annular diffuser are shown in Table 6.1 and Figure 6.1, respectively.

Table 6.1: Geometrical parameters of the annular diffuser.

$R_{hi} = 38 \text{ mm}$ $R_{ci} = 77.5 \text{ mm}$, $R_{ho} = 38 \text{ mm}$, $(R_h/R_c)_I = 0.49$, $L/AR = 8.54$, $\theta_h = 0^\circ$, $L = 33.76 \text{ cm}$			
Types of diffuser	θ_c	$R_{co}(\text{cm})$	AR
A	3°	9.52	1.67
B	6°	11.3	2.48
C	9°	13.1	3.44

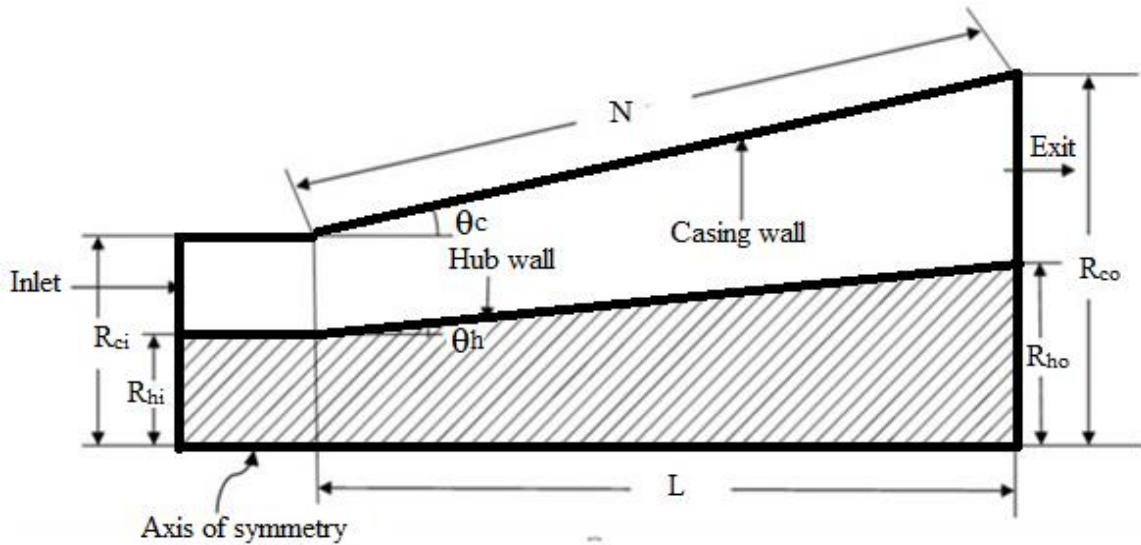


Figure 6.1: Design of an annular diffuser with its components.

6.2 Parallel Hub Axial Annular Diffuser

The performance characteristics and flow behavior of three annular diffusers with various fluid flow conditions along the flow path have been discussed in terms of turbulence intensity, velocity vector, velocity profiles, static pressure recovery coefficient (C_p), and total pressure loss coefficient (C_L). The computational studies were

carried out on swirl flow (7.5° , 12° , 17° , and 25°) and non-swirl flow (0°). The detailed description of the study is discussed at the inlet swirl angles of 0° , 12° , and 25° are given below.

6.2.1 Turbulence Intensity

Turbulence intensity at the entrance of the annular cross-section with various inlet swirl angles (0° - 25°) is shown in Figure 6.2. The turbulence intensity is lowest near the center of the cross-section and highest at the diffuser's outer wall. The figure shows a significant deviation between the diffuser's inner and outer walls, as well as the strong shear layer near the casing wall. The swirl flow does not much affect the magnitude of intensity and nature of flow distribution. The transverse component of turbulent energy is produced near the casing wall and is suppressed close to the hub wall. These profiles agree with the findings of Coladipietro et al. (1975); Hoadley (1970).

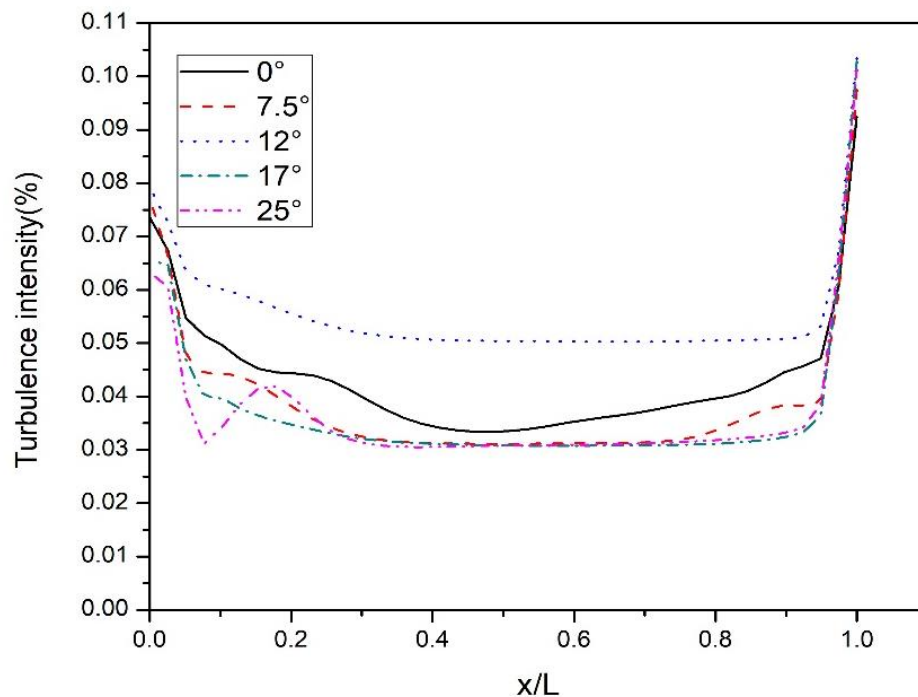


Figure 6.2: Turbulence intensity at the inlet.

6.2.2 Velocity Vector

The velocity vectors of the two-dimensional axisymmetric parallel hub annular diffusers are shown in Figure 6.3 at the swirl angles of 0° , 12° , and 25° . The vector clearly shows the fluid movement between the hub and casing walls as per the value of the inlet swirl angles of the diffuser passage. It is apparent from Figure 6.3 (i) that the fluid uniformly flows between the walls along the length of the flow path where diffusion takes place.

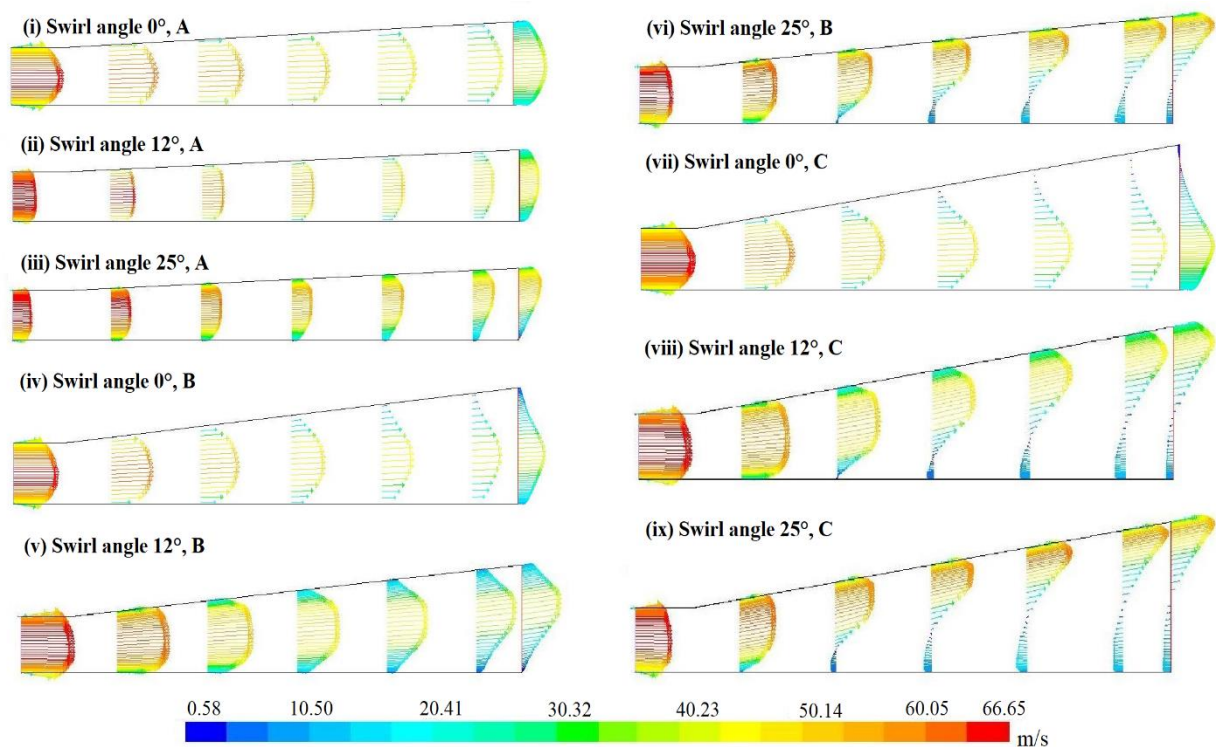


Figure 6.3: (i-ix) Velocity vector contours of diffusers A, B, and C at swirl angles of 0° , 12° , and 25° .

In the case of swirl flow, the fluid is moved from the inner wall to the outer wall, and there is no reversal flow along the length due to the less annular space in diffuser A. The flow is reversed from the hub wall in diffuser B due to the adverse pressure gradient on the hub surface at the inlet swirl angle of 25° . The flow separation from the casing wall at the swirl angle of 0° and reversed flow occurs on the hub wall at the swirl angles

of 12° and 25° for the C-type diffuser due to the availability of large annular diffusion space.

6.2.3 Velocity Profiles

The velocity profiles are represented in non-dimensional velocity as local longitudinal or local swirl velocity to the transverse's local maximum longitudinal velocity. At each location along the diffuser passage, the transverse is taken normally with the hub position. The non-dimensional velocity has been plotted as a function of the non-dimensional diffuser passage height of the cross-section. Where y represents the local diffuser passage height and Y_m represents the maximum diffuser passage height; both are measured from the centerline. So, $y/Y_m = 1$ represents the casing position, and $y/Y_m = 0$ represents the hub position as per the area ratio and equivalent cone angle. The figures are displayed at numerous transverses of the non-dimensional flow path $x/L = 0.1, 0.3, 0.5, 0.7$ and 0.9 for all of the diffuser's inlet swirl angles and area ratios. The velocity profiles are shown in Figures 6.4-6.5 without inlet swirl (0°) and with inlet swirl ($12^\circ, 25^\circ$). In the non-swirl flow, more fluid moves toward the hub wall of the diffuser passage in the case of diffuser A, as shown in Figure 6.4 (i). With the introduction of the swirl, there is a uniform flow between the inner and outer walls of the flow passage at the swirl angle of 12° . The reversal of flow does not occur on both walls of the diffuser for swirl or non-swirl flow. The longitudinal velocity peak shifts towards the casing at $y/Y_m = 0.49$ and 0.71 for the transverse section $x/L = 0.9$ of the A-type diffuser at inlet swirl angles of 12° and 25° . Figures 6.4 (iii) and 6.5 (ii) show the swirl velocity distribution at 12° and 25° inlet swirl angles, respectively. It shows that the tangential component of velocity increases toward the casing of the diffuser. However, the magnitude varies depending on the cross-section, and the patterns are similar to the swirl velocity distribution, as shown in Figures 6.4 (iii) and 6.5. (ii).

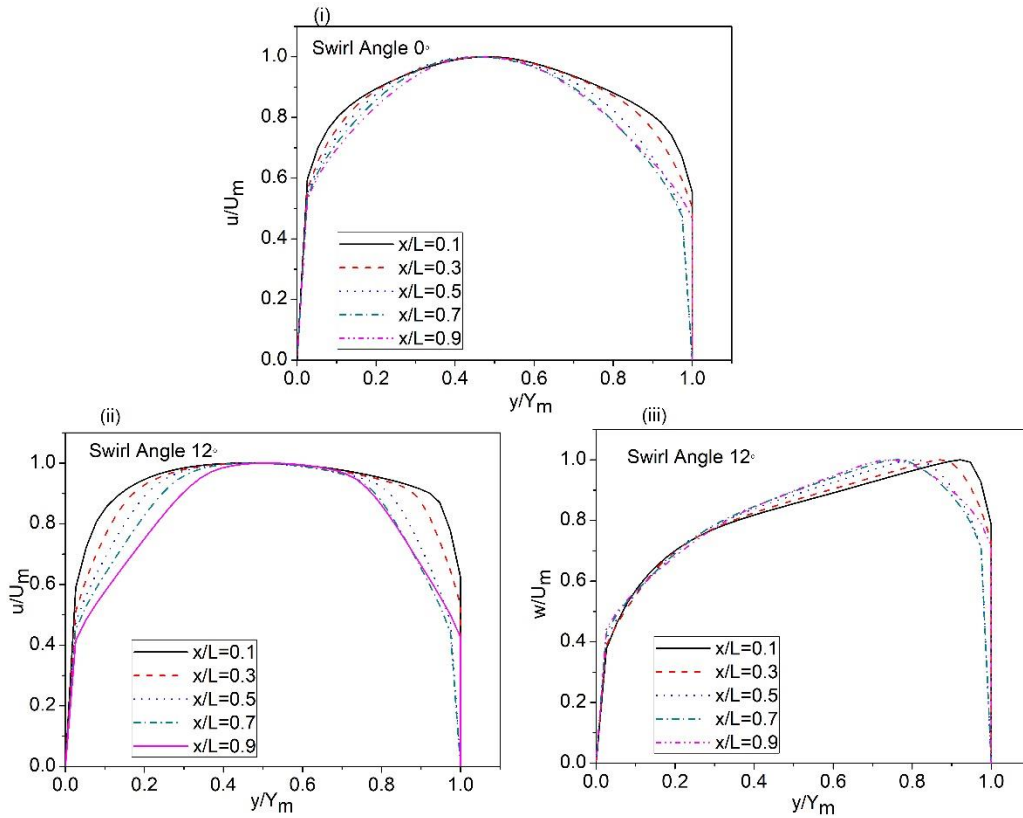


Figure 6.4: (i-ii) Longitudinal velocity distribution of diffuser A at 0° and 12°swirl angles; (iii) Swirl velocity distribution of diffuser A at a 12°swirl angle.

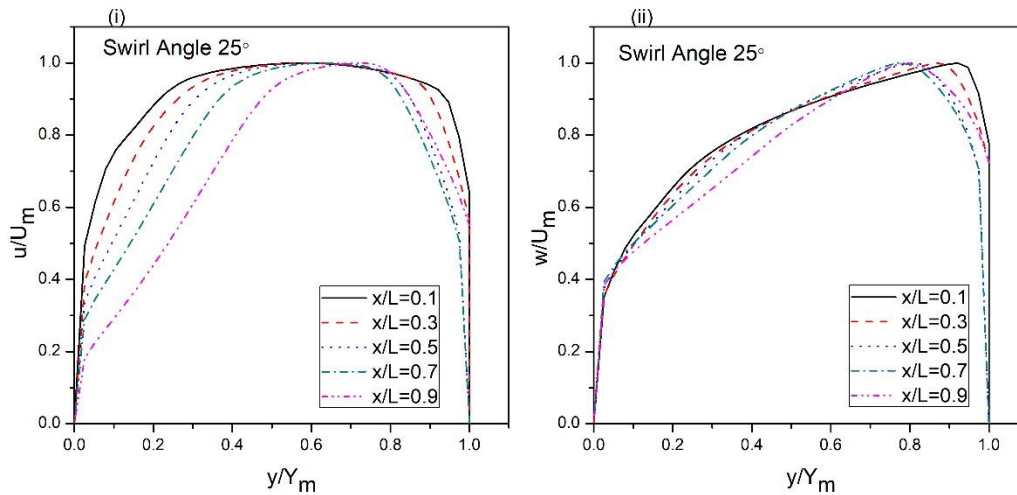


Figure 6.5: (i) Longitudinal velocity distribution of diffuser A at a 25° swirl angle; (ii) Swirl velocity distribution of diffuser A at a 25°swirl angle.

The distribution of longitudinal and the swirl velocity profiles are shown in Figures 6.6 and 6.7 of the B-type annular diffuser. In the case of non-swirl flow, the flow is hub generated, and the shift towards the hub increases significantly as the area ratio increases for the similar inlet velocity profile.

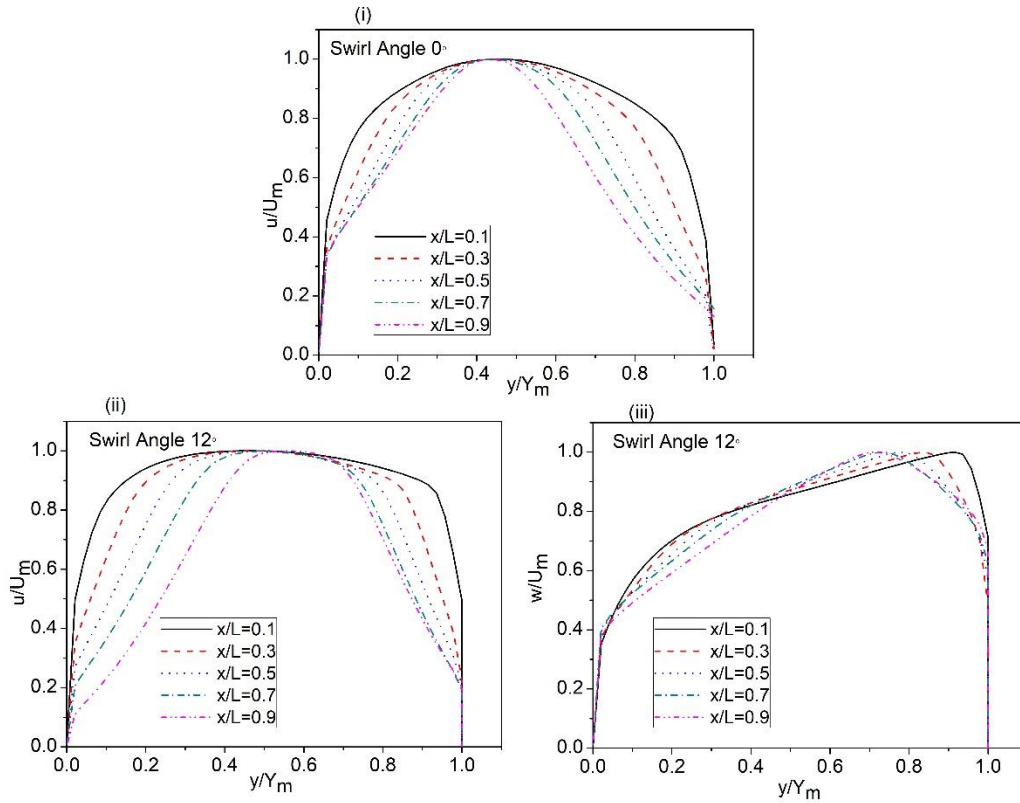


Figure 6.6: (i-ii) Longitudinal velocity distribution of diffuser B at 0° and 12° swirl angles; (iii) Swirl velocity distribution of diffuser B at a 12° swirl angle.

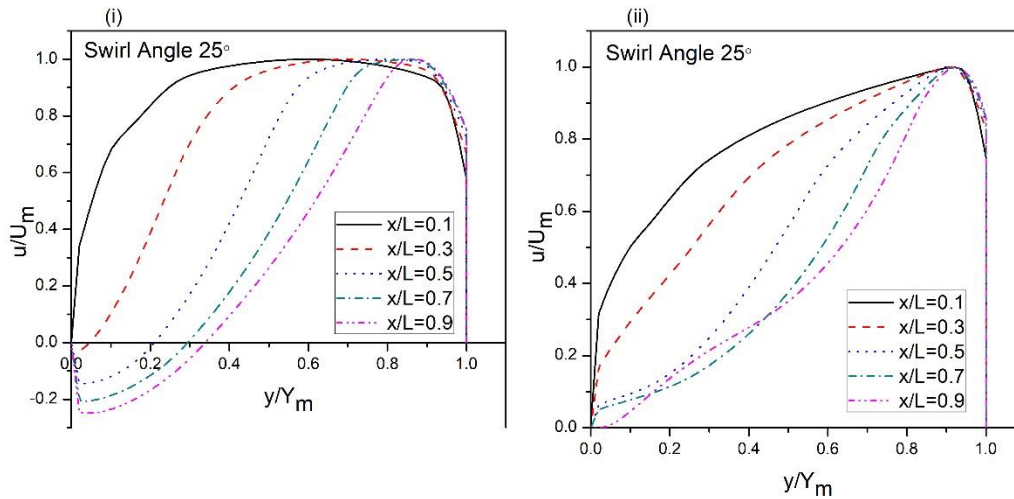


Figure 6.7: (i) Longitudinal velocity distribution of diffuser B at a 25° swirl angle; (ii) Swirl velocity distribution of diffuser B at a 25° swirl angle.

The bulk fluid moves in between two walls at an inlet swirl angle of 12°. The peak velocity at $x/L = 0.9$ is observed at $y/Y_m = 0.56, 0.87$ area ratio of 2.48 for the swirl angles of 12°, and 25° in a B-type diffuser. The fluid flow is reversed up to $y/Y_m = 0.04, 0.20, 0.28$ and 0.34 for $x/L = 0.3, 0.5, 0.7,$ and $0.9,$ respectively for an inlet swirl angle

of 25° . The swirl velocity profile trends are due to the forced vortex phenomenon. It also demonstrates that the swirl velocity is increased as the radius increases.

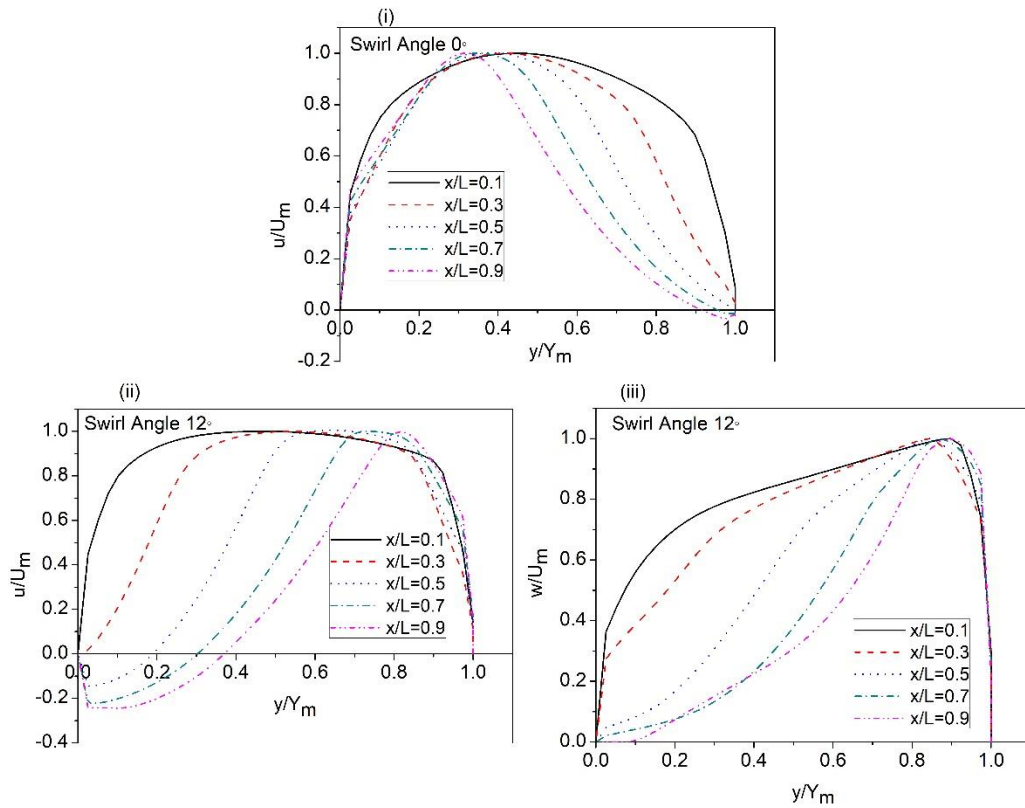


Figure 6.8: (i-ii) Longitudinal velocity distribution of diffuser C at 0° and 12° swirl angles; (iii) Swirl velocity distribution of diffuser C at a 12° swirl angle.

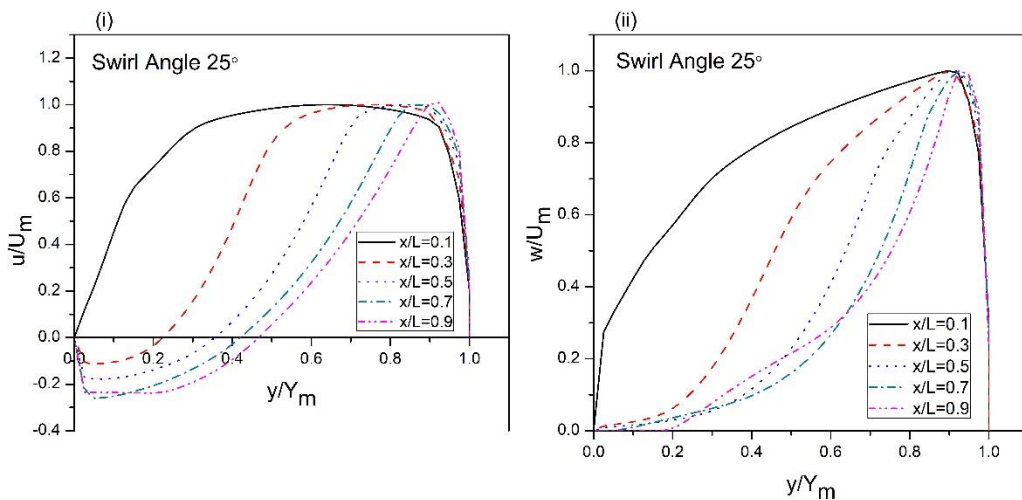


Figure 6.9: (i) Longitudinal velocity distribution of diffuser C at a 25° swirl angle; (ii) Swirl velocity distribution of diffuser C at a 25° swirl angle.

The distribution of longitudinal and the swirl velocity profiles are shown in Figures 6.8 and 6.9 of the C-type diffuser having $AR = 3.44$ and a casing angle of 9° . Flow reversal

occurs on the casing wall in the absence of swirl and the hub wall in the presence of swirl. The flow is reversed from $y/Y_m = 0.97$ and 0.92 up to the diffuser exit at $x/L = 0.7$ and $x/L = 0.9$ at 0° inlet swirl angle. At 12° and 25° inlet swirl angles, flow separation is observed on the inner surface. The flow separation is observed on the hub wall at inlet swirl angles of 12° and 25° . In a swirling flow, centrifugal force propels the flow towards the diffuser's casing wall. In the C-type diffuser, wide annular space is available; hence, flow separation is greater than the B-type diffuser. Figures 6.8 (iii) and 6.9 (ii) depict the same nature of swirl velocity profiles as the earlier case due to the forced vortex nature.

6.2.4 Static Pressure Recovery Coefficient

The main function of the diffuser is to recover the static pressure. The variations of C_p along the flow length of the annular diffusers A, B, and C for swirling and non-swirling flow are shown in Figures 6.10 (i), 6.11 (i), and 6.12 (i). The static pressure at any point in the diffuser passage is computed using a mass-weighted average value. It is observed from Figures 6.10 (i) that the static pressure improves continuously along the length of either a swirl or non-swirl flow. At the swirl angle of the 25° in A-type diffuser, the highest C_p occurs at $x/L = 0.88$ of the passage. In swirl flow, the pressure recovery coefficient rises at the beginning of the B-type diffuser compared to non-swirl flow. The maximum pressure recovery and minimum pressure loss coefficient occur in the B-type diffuser at a swirl angle of 12° . The lowest pressure recovery is observed at the swirl angles of 17° and 25° of the diffuser passage is beyond $x/L = 0.50$ and $x/L = 0.25$ than without swirl flow. The distorted velocity profile is correlated with the existence of flow separation, which acts like a decline in pressure recovery. Beyond $x/L = 0.56$, 0.48 , 0.15 , 0.12 , the magnitude of static pressure in the C-type diffuser is lesser than the flow without swirl for swirl angles of 7.5° , 12° , 17° , and 25° .

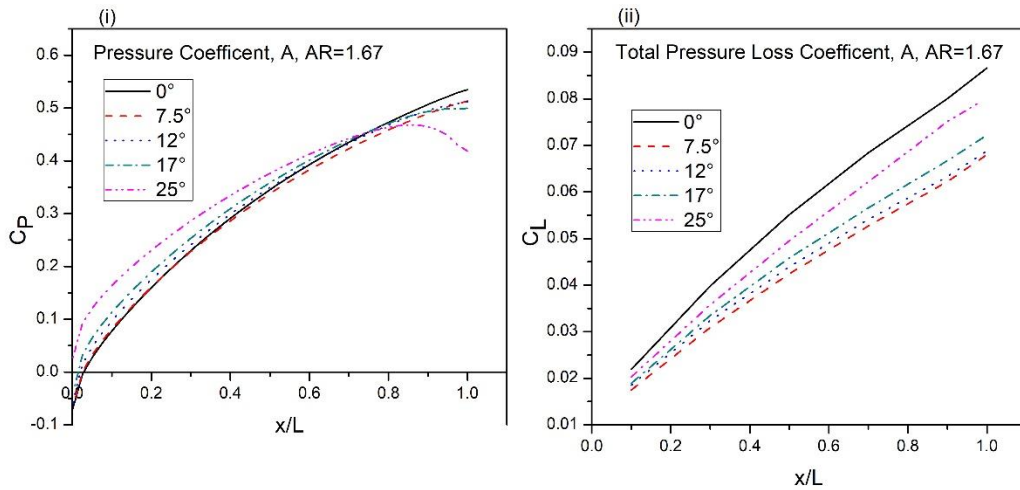


Figure 6.10: (i) Static pressure recovery coefficient (C_p) at the casing of diffuser A; (ii) Total pressure loss coefficient (C_L) of diffuser A.

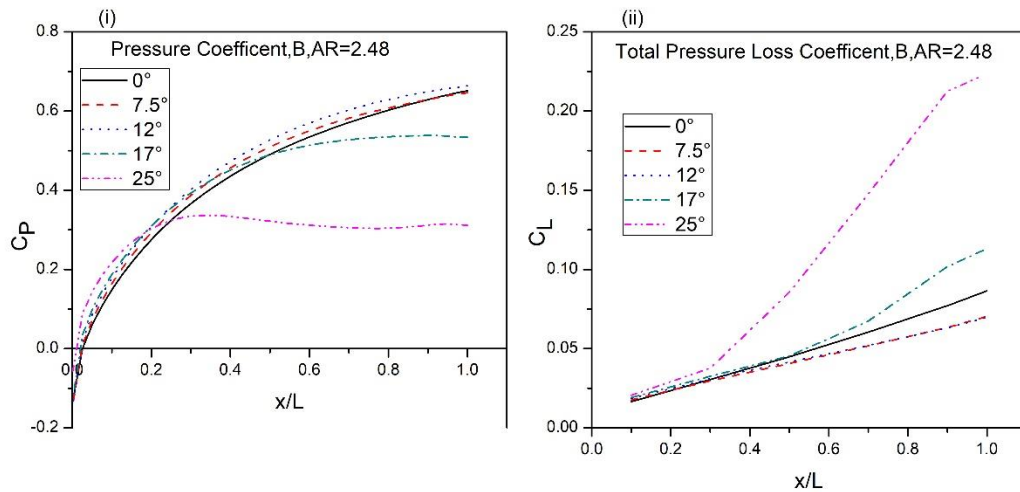


Figure 6.11: (i) Static pressure recovery coefficient (C_p) at the casing of diffuser B; (ii) Total pressure loss coefficient (C_L) of diffuser B.

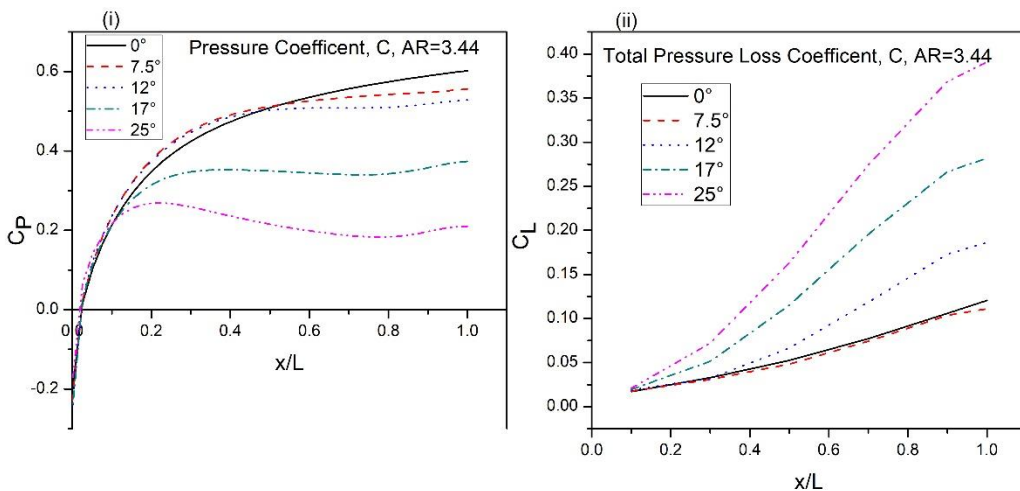


Figure 6.12: (i) Static pressure recovery coefficient (C_p) at the casing of diffuser C; (ii) Total pressure loss coefficient (C_L) of diffuser C.

There is a marginal increases in pressure recovery with the swirl flow at the commencement of the flow path after that decrease due to the decay of swirl intensity and the wide divergence angle of the casing.

For non-swirl flow, the effect of static pressure recovery coefficient (C_p) with the area ratio (AR) and the non-dimensional diffuser passage of the annular diffusers are plotted as shown in Figures 6.13 (i) and 6.13 (ii), respectively. The computational results of the three tested diffusers show meticulous agreement with the outcomes of Sovran (1967); Coladipietro et.al. (1975). The highest pressure recovery is produced in the B-type diffuser as compared to the remaining two diffusers, as shown in Figures 6.13 (i) and 6.13 (ii).

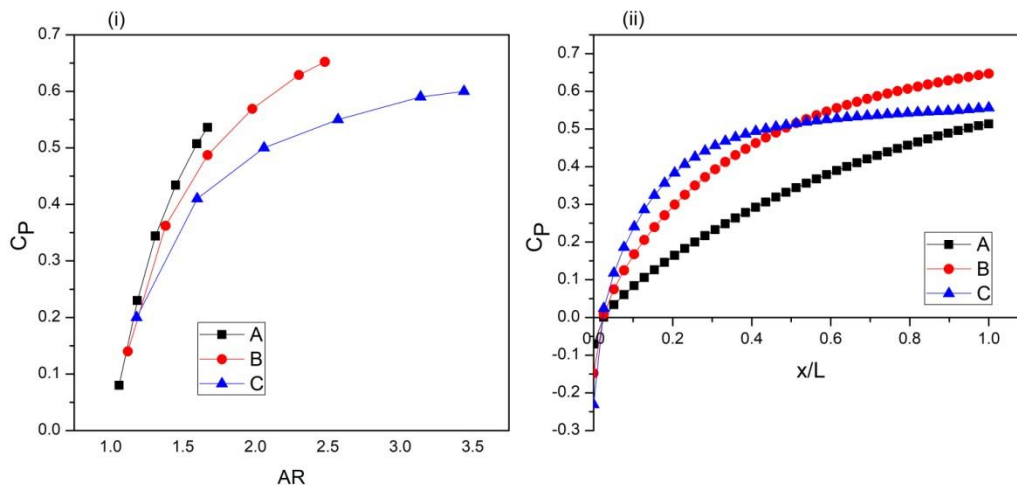


Figure 6.13: (i) C_p with the area ratio of diffusers A, B, and C; (ii) C_p with the non-dimensional length of diffusers A, B, and C.

The maximum pressure recovery is significantly less due to the limited area ratio in the A-type diffuser as compared to other diffusers. In a C-type diffuser, static pressure recovery (C_p) of 55% is observed at the exit of the flow length. The maximum static pressure is achieved up to the mid-length of the diffuser passageway. After that, it depreciates due to the reversal of flow on the casing wall, and its value lies between the A and B-types of diffusers, as shown in Figure 6.13 (ii).

6.2.5 Total Pressure Loss Coefficient

The total pressure loss coefficient is inversely proportional to the effectiveness of the diffuser. The pressure loss coefficient declines as the diffuser effectiveness rises, and vice versa. As a result, the diffuser with the best performance has the lowest pressure loss coefficient. The loss coefficients are shown in Figures 6.10 (ii), 6.11 (ii), and 6.12 (ii) of diffusers A, B, and C, respectively. In the A-type diffuser, the lowest pressure loss coefficient is observed at a swirl angle of 7.5° due to the uniform flow between the two walls and no adverse pressure gradient on the walls. The highest pressure loss coefficient is observed at a swirl angle of 25° in B and C type diffusers, equal to 23 percent and 40 percent, respectively. The maximum loss coefficient degrades the performance of the diffuser.

6.3 Concluding Remarks

The investigations were carried out on three PHDC annular diffusers with swirling and non-swirling flow, and the important findings are as follows:

1. It is found that with swirl flow, the local velocity increases continuously in the downstream diffuser passage as seen in the longitudinal velocity profiles.
2. The finding of the swirl flow shows that the flow moves towards the casing wall of the diffuser, due to which no adverse pressure gradient is observed on the outer wall.
3. A high inlet swirl angle increases the pressure recovery up to a certain distance; after that, the diffuser's performance depreciates due to the reversal of flow on the hub wall.
4. The maximum performance is observed in a B-type diffuser at an inlet swirl angle of 12° and has the lowest total pressure loss coefficient at that angle.

Chapter-7

7 Computational Investigation: Effect of Swirl Flow on the Performance of Axial Annular Diffusers

This chapter discusses the performance characteristics of an axial flow annular diffuser with modified divergent casing varying between equivalent cone angles (10° , 15° , and 20°) and area ratios of 2 and 3. The numerical simulations were performed to examine the inlet swirl's effect on the annular diffusers. Simulations were performed on a fully developed flow at Reynolds number 2.5×10^5 . The results are analyzed using the velocity profiles, static pressure recovery coefficient (C_p), and total pressure loss coefficient (C_L). Velocity profiles were assessed along the span of diffusers in several locations. The following studies were undertaken in the present chapter:

1. PHDC annular diffuser equivalent cone angles of 10° , 15° , and 20° having the same area ratio of 3 with swirling and non-swirling flow.
2. PHDC annular diffuser with an equivalent cone angle of 15° for an area ratio of 2 with swirling and non-swirling flow.
3. UHDC annular diffuser with an equivalent cone angle of 15° for an area ratio of 3 with swirling and non-swirling flow.

7.1 Study of Parallel Hub Diverging Casing Annular Diffuser having Different Equivalent Cone Angle

The diffusers having equivalent cone angles of 10° , 15° , and 20° of the same area ratio ($AR = 3$) have been selected for present investigations. The fully developed turbulent flow with swirl angles of 0° , 7.5° , 12° , 17° , and 25° is selected to generate a tangential

velocity type distribution at the inlet of the diffuser. The primary goal of the research is to improve the annular diffuser's performance. The annular diffuser is used in conjunction with the gas turbine to increase the power plant's efficiency. The computationally determined velocity vectors, longitudinal velocity profiles, swirl velocity profiles, static pressure recovery coefficient (C_p), and total pressure loss coefficient (C_L) across the length of the diffusers are presented and discussed.

7.1.1 Physical Model

Based on the exhaustive literature review, it is very difficult to conclude which choice of geometrical parameters and dynamic parameters will give the desirable performance of diffusers because the fluid flow is quite complicated. Since there is no research carried out on the different cone angles and having the same area ratio, there is a need for exploration. The objective of this research work has been to examine the impact of geometrical parameters on the performance of area ratio 3. These annular diffuser geometric values have been optimized for maximum pressure recovery and the lowest pressure loss coefficient. The effect of swirl intensity with various swirl regimes on the flow behavior of annular diffusers is also being investigated. Further, they prophesy the flow separation and reattachment of the flow inner side of the annular diffusers.

Table 7.1: Geometrical parameters of straight hub axial annular diffusers.

$R_{hi} = 3.8 \text{ cm}, R_{ci} = 7.75 \text{ cm}, \theta_h = 0 \text{ (deg)}, AR = 3$				
Sr. No.	θ_c (deg)	L (cm)	$L/\Delta R$	θ_e (deg)
A	4.6	56.51	14.30	10
B	6.91	37.55	9.50	15
C	9.22	28.04	7.09	20

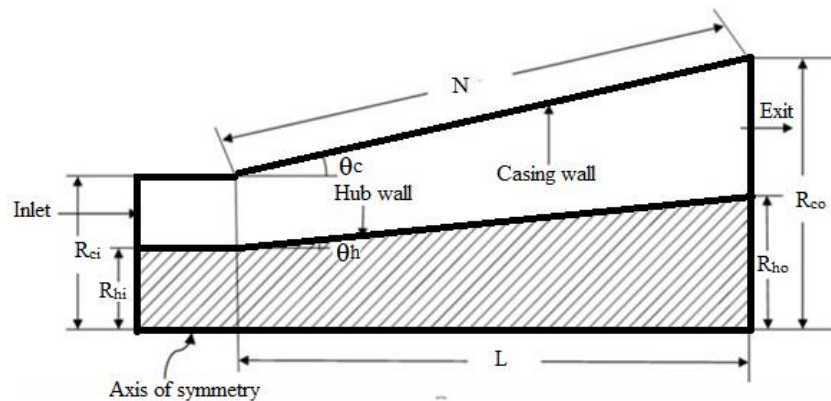


Figure 7.1: Geometrical design of the annular diffuser.

Figure 7.1 and Table 7.1 show the geometrical configuration details of the straight hub axial annular diffuser parameters.

7.1.2 Velocity Vector

The axisymmetric 2D annular diffusers (A, B, and C) with and without swirl flow of velocity vector at the inlet (0° , 12° , and 25°) are shown in Figure 7.2. The velocity vectors show the result across the length, i.e. inlet, $x/L = 0.1, 0.3, 0.5, 0.7, 0.9$, and outlet using CFD. The uniform flow is distributed between the casing and the hub wall at swirl angles of 0° and 12° as the flow moves toward the downward direction in diffuser A. The flow separation is observed on the inner wall at an inlet swirl angle of 25° along the two-third length of diffuser A. In diffuser B, the reverse flow is observed at the swirl angles of 12° and 25° on the hub walls because of the existence of adverse pressure gradient inside the diffuser. The high casing divergent angle in diffuser C is due to that flow separation is observed on the outer wall with the non-swirling flow. The separation zone's size increases with the inlet swirl angles (12° , and 25°) and results in the shifting of flow separation position and negative velocity towards the hub wall. The flow

visualization in the velocity vectors for a 25° inlet swirl angle shows stable flow on the casing wall with large separations from the hub wall.

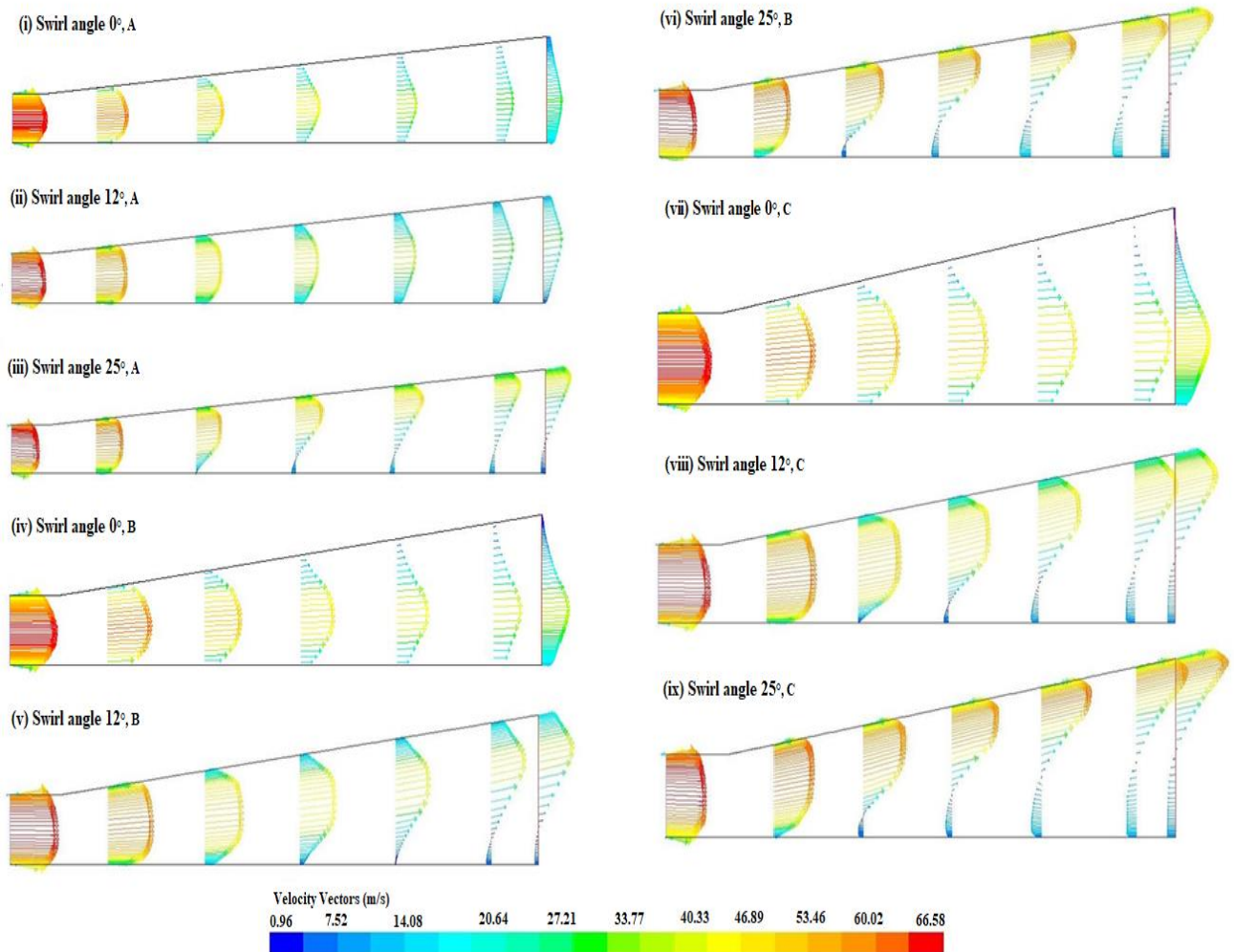


Figure 7.2: (i-ix) Velocity vector contours at swirl angles of 0°, 12°, and 25° for the equivalent cone angles of 10°, 15°, and 20°.

7.1.3 Velocity Profiles

The flow behavior and performance of diffusers (A, B, and C) have been shown in Figures 7.3-7.8 in the form of longitudinal velocity profiles and swirl velocity profiles concerning mass average velocity with various inlet swirl angles, i.e. 0°, 7.5°, 12°, 17°, and 25°. Explained in detail, three cases with inlet swirl angles are 0°, 12°, and 25° for the sake of brevity with velocity profiles.

The graphs shown in Figures (7.3-7.8) are drawn at different locations, i.e. $x/L = 0.1, 0.3, 0.5, 0.7,$ and 0.9 for diffusers of area ratio 3 with swirl angles of $0^\circ, 12^\circ,$ and 25° . For no swirl condition, flow is accumulated near the hub at a cone angle of 10° as shown in Figure 7.3 (i).

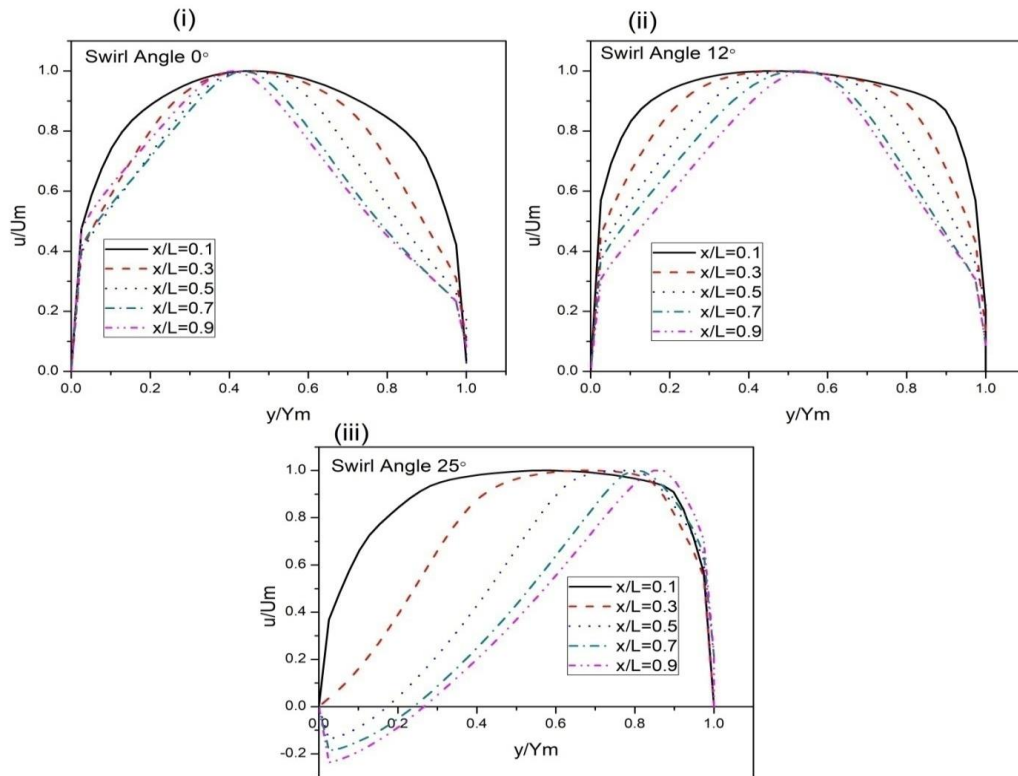


Figure 7.3: (i-iii) Longitudinal velocity distribution at inlet swirl angles of $0^\circ, 12^\circ,$ and 25° for an equivalent cone angle of 10° .

The peak velocity occurs at $x/L = 0.9$ in area ratio (AR) 3 at y/Y_m 0.41, 0.39, 0.30 for equivalent cone angles of $10^\circ, 15^\circ,$ and $20^\circ,$ respectively. The velocities recede at a faster rate on the walls as continuous diffusion occurs throughout the diffusers. The tangential movement generated by the swirl of 12° is not enough to move the bulk flow from the hub to the casing, as displayed in Figure 7.3 (ii). Figure 7.3 (iii) depicts a reversal trend for a 25° swirl in the longitudinal velocity distribution. In this case, the bulk flow moved towards the outer wall. At a swirl angle of $25^\circ,$ the reverse flow for $x/L = 0.5, 0.7,$ and 0.9 is reversed up to $y/Y_m = 0.18, 0.25,$ and $0.27,$ respectively. The

swirl velocity distribution is shown in Figure 7.4 (i-ii) at the 12° and 25° swirl angles. The trends are similar for 12° and 25° swirl angles, but the value of magnitude is different. The bulk flow is forced toward the casing in the case of a swirl angle of 25°. These patterns are based on the principle of angular momentum conservation. The flow is moving towards the outer wall by introducing a swirl.

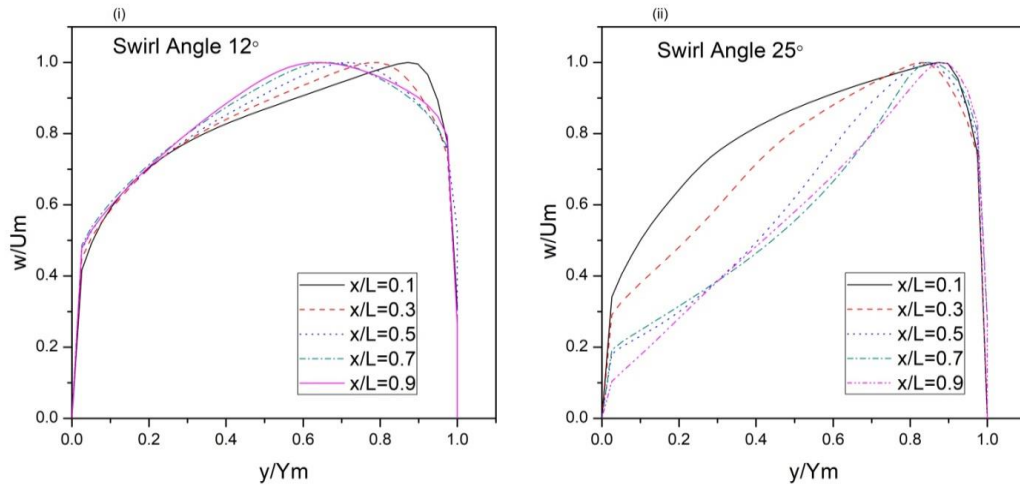


Figure 7.4: (i-ii) Swirl velocity distribution at inlet swirl angles of 12° and 25° for an equivalent cone angle of 10°.

The longitudinal velocity distribution of a cone angle of 15° with *AR* of 3 in a straight hub axial annular diffuser at swirl angles of 0°, 12°, and 25° is presented in Figure 7.5 (i-iii). The diffusion takes place continuously along the diffuser length. For the non-swirl flow, most of the fluid is close to the hub wall and separation is taking place at swirl angles of 12° and 25°, as seen in Figure 7.5 (ii-iii). The reverse flow occurred on the inner wall at the inlet swirl angle of 12° and 25° for $x/L = 0.7-0.9$ and $x/L = 0.5-0.9$, respectively. The swirl velocity distribution is shown in Figure 7.6 (i-ii). The swirl velocity is increased toward the diffuser's casing wall, according to these plots. Due to the forced vortex nature, swirl velocity around the outside surface is higher in the case of a 25° inlet swirl.

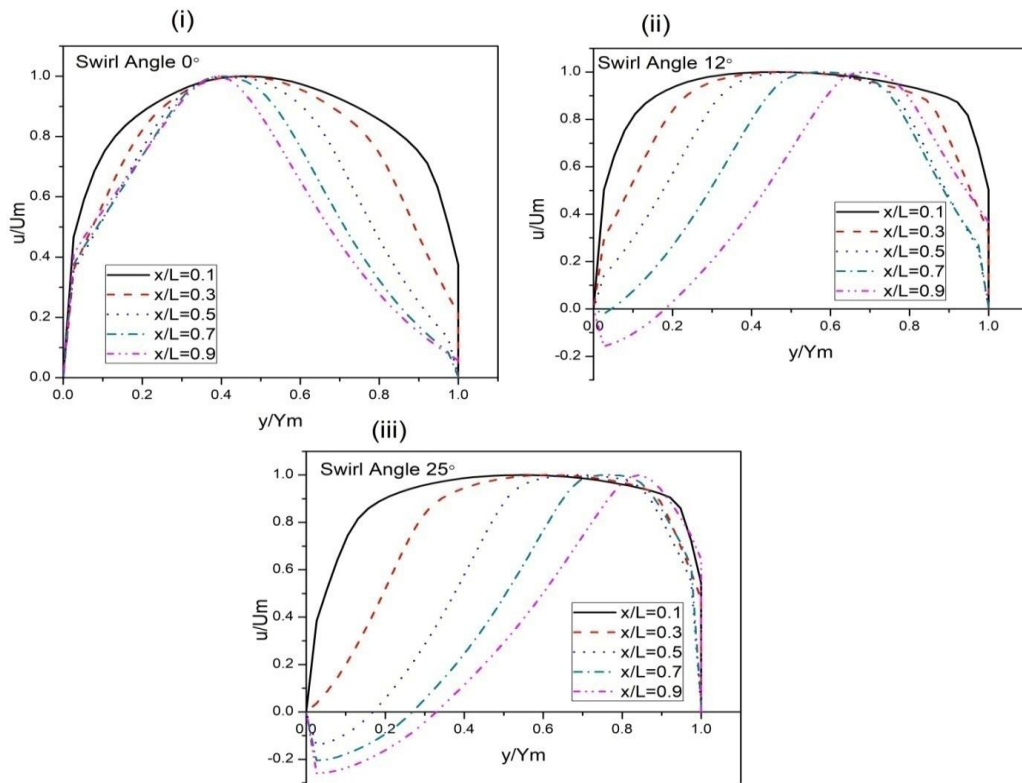


Figure 7.5: (i-iii) Longitudinal velocity distribution at inlet swirl angles of 0° , 12° , and 25° for an equivalent cone angle of 15° .

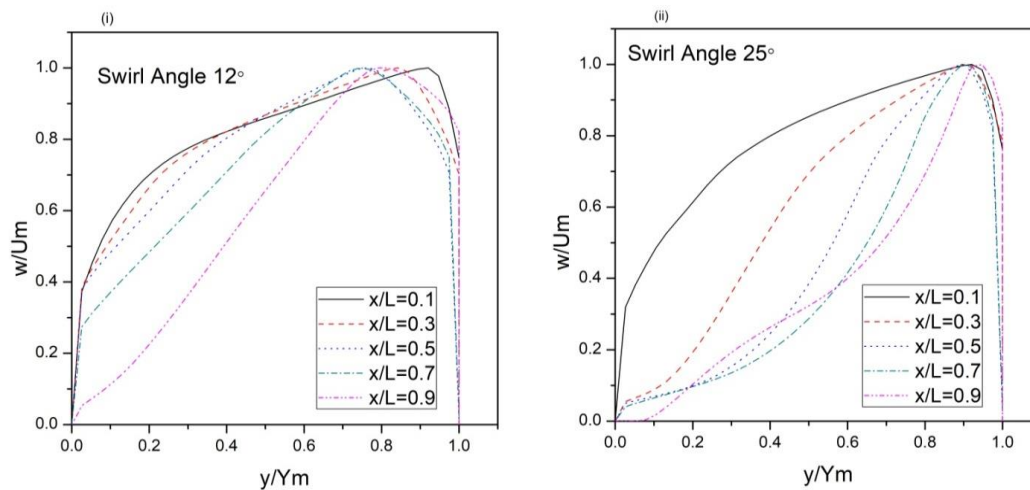


Figure 7.6: (i-ii) Swirl velocity distribution at inlet swirl angles of 12° and 25° for an equivalent cone angle of 15° .

The longitudinal velocity distribution of equivalent cone angle 20° with area ratio 3 in the straight hub axial annular diffuser at swirl angles of 0° , 12° , and 25° is presented in Figure 7.7 (i-iii).

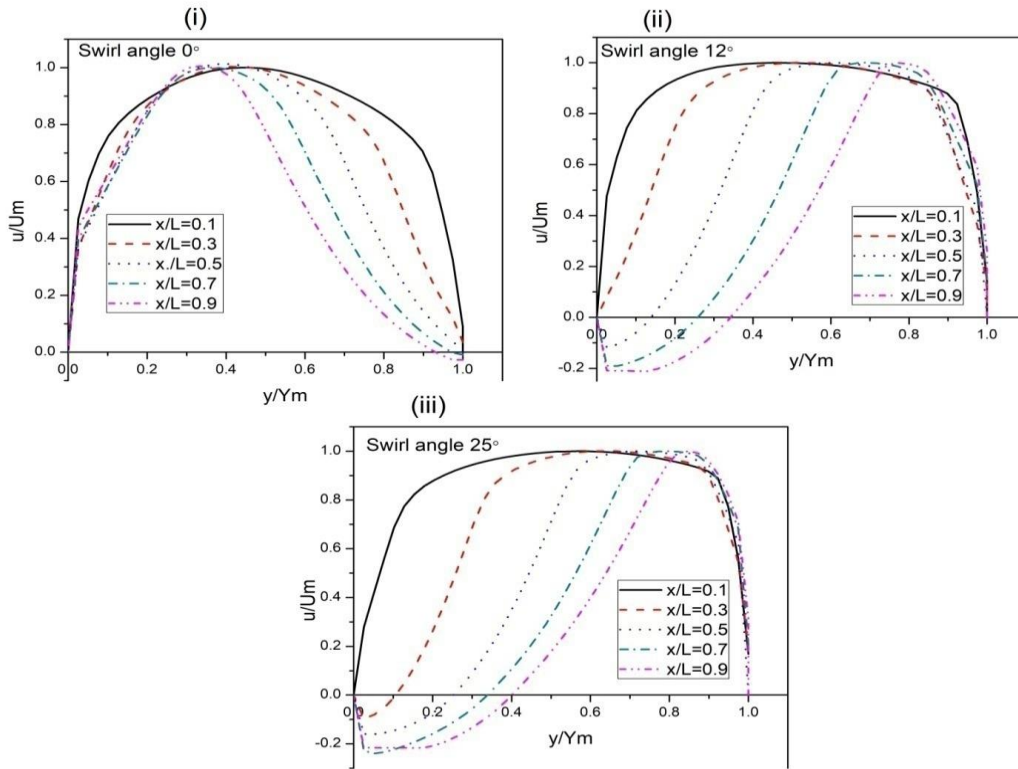


Figure 7.7: (i-iii) Longitudinal velocity distribution at inlet swirl angles of 0° , 12° , and 25° for an equivalent cone angle of 20° .

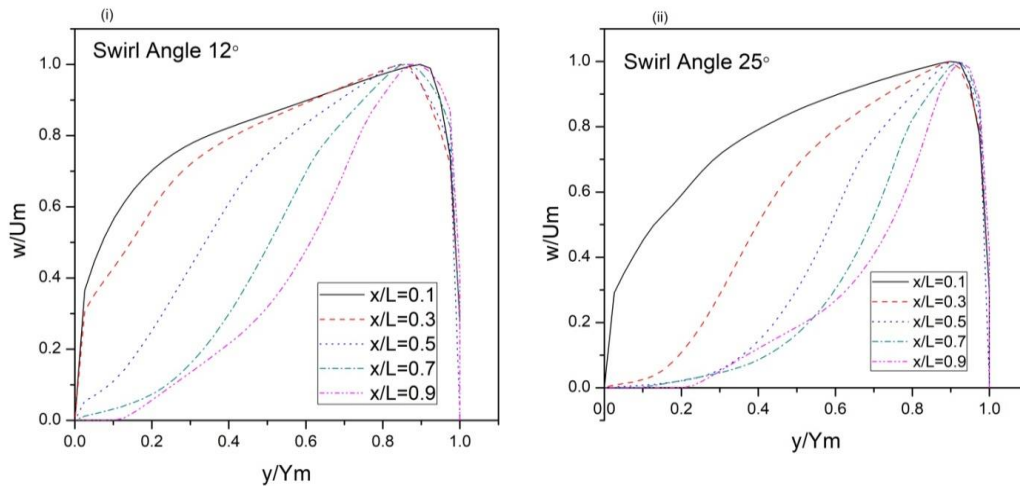


Figure 7.8: (i-ii) Swirl velocity distribution at inlet swirl angles of 12° and 25° for an equivalent cone angle of 20° .

For the 0° inlet swirl condition, massive fluid flow close to the hub surface and the flow separation occurred at the casing wall due to the largest divergence angle of the flow passage. As compared to A and B type diffuser cases, the early detachment occurred near the inner surface in the C type diffuser at 12° and 25° inlet swirl angles. The reverse

flow occurred on the hub wall at 12° and 25° inlet swirl angles of $x/L = 0.5-0.9$ and $x/L = 0.3-0.9$, respectively. Figure 7.8 (i-ii) depicts the swirl velocity distribution for inlet swirl angles of 12° and 25° . The swirl velocity shifted toward the casing for a higher swirl angle. The high swirl velocity near the casing indicates the flow separation from the hub. The above phenomena indicate that the swirl decays as the flow moves in the downward direction of the diffuser.

The flow distribution of velocity profiles is very well matched with the Coladipietro et al. (1975); Hoadley (1970) with swirl flow, who attributed this behavior to centrifugal effect force. The centrifugal force pushes the flow toward the diffuser's casing wall, delays the flow detachment, stabilizes the flow and escalates the flow separation from the inner surface. The flow behavior of the three diffusers is affected by the cone angle. The wall angle increases, then velocity profiles are distorted as seen in the velocity profiles in spite of the same AR . The diffuser's performance is susceptible to the cone angle as well as the swirl angle.

7.1.4 Static Pressure Recovery Coefficient

The mass average coefficient of pressure recovery was determined in a diffuser with cone angles of 10° , 15° , and 20° and inlet swirl angles of 0° , 7.5° , 12° , 17° , and 25° at the diffuser casing wall. Figures 7.9 (i), 7.10 (i), and 7.11 (i) show the pressure coefficient at the casing for area ratio 3 with normalized axial length x/L . C_p increases with flow downstream of the diffuser passage, as shown by the plots. The curves drawn represent the value of C_p for swirl flow almost identical to the 0° swirl. The figure shows that marginal C_p improves with the swirl flow in the beginning because of the radial pressure existing on the outer surface, and later on decreases due to separation of flow on the hub observed from the longitudinal velocity profile distribution. The swirl increases the C_p at the entrance of the downstream diffuser passage as compared to the

non-swirl flow. Figure 7.9 (i) depicts the C_p plot. It exhibits the greatest improvement in the pressure recovery at an equivalent cone angle of 10° with a 7.5° inlet swirl angle. The maximum pressure recovery for equivalent cone angles of 15° up to 12° swirl angle gives the best performance. The pressure recovery increases up to $x/L = 0.60$, and 0.54 for swirl angles of 7.5° and 12° , respectively, at an equivalent cone of 20° . After that, it decreases due to decay of swirl intensity and separation of flow. The highest C_p is up to $x/L = 0.18$, 0.15 , and 0.12 for equivalent cone angles of 10° , 15° , and 20° , respectively, at an inlet swirl angle of 25° of the diffuser passage. The unbalanced increases in rotational kinetic energy losses could be attributed to a decline in diffuser performance at high swirl angles. The maximum percentage of static pressure recovery growth for diffuser A is consistent with the findings of Coladipietro et al. (1975), who demonstrated that the swirl effect is more effective for diffusers with a lower cone angle. The lowest pressure recovery is accredited to a higher casing angle of diffuser C, which results in more growth of the boundary layer and a high adverse pressure gradient on the surface.

Figure 7.12 (i) depicts the variations in the C_p with inlet swirl angle for three diffuser types (A, B, and C). These plots show that there is a maximum static pressure recovery coefficient with swirl angles of 7.5° and 12° for equivalent cone angles of 10° and 15° , respectively. In diffuser C, pressure recovery is not improved at the exit with swirl flow, but it increases up to a certain length, as seen in Figure 7.11 (i). According to the experimental data of Lohmann et al. (1979), increasing the inlet swirl angle beyond 25° causes a distorted velocity profile as well as a decrease in static pressure recovery from the core flow. The coefficient of static pressure recovery (C_p) with a variation of the area ratio of diffusers A, B, and C along the length of non-swirl flow is shown in Figure 7.12 (ii).

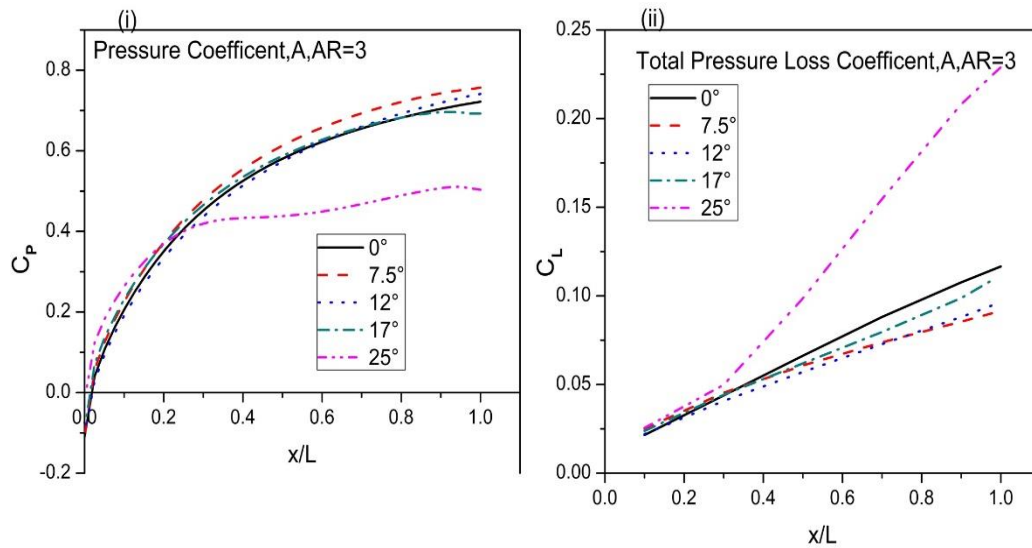


Figure 7.9: (i) Static pressure recovery coefficient at the casing wall with a cone angle of 10°; (ii) Total pressure loss coefficient with a cone angle of 10°.

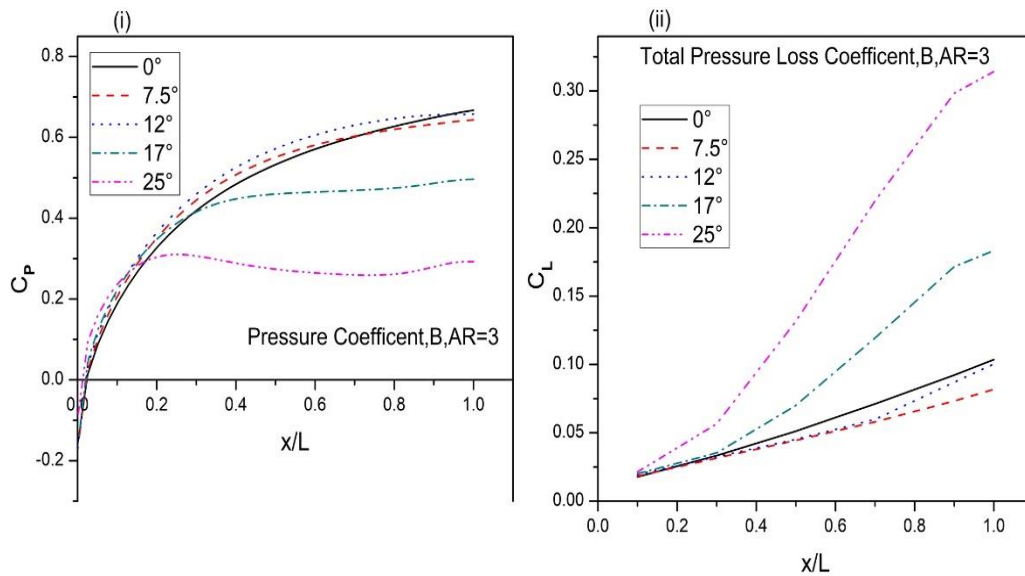


Figure 7.10: (i) Static pressure recovery coefficient at the casing wall with a cone angle of 15°; (ii) Total pressure loss coefficient with a cone angle of 15°.

The three test diffusers of non-swirl flow very well match the results of Sovran (1967); Coladipietro et al. (1975). Even though there is pressure recovery increasing continuously along the casing wall, there is a limit to the area ratio of 3. Maximum pressure recovery is obtained from an equivalent cone angle of 10° for the A-type diffuser, as shown in the figure.

7.1.5 Total Pressure Loss Coefficient

The total pressure loss coefficient nearly linearly increases along the longitudinal length. As displayed in Figure 7.9 (ii), the C_L plot shows that the minimum loss coefficient for equivalent cone angle is 10° at 12° inlet swirl angle.

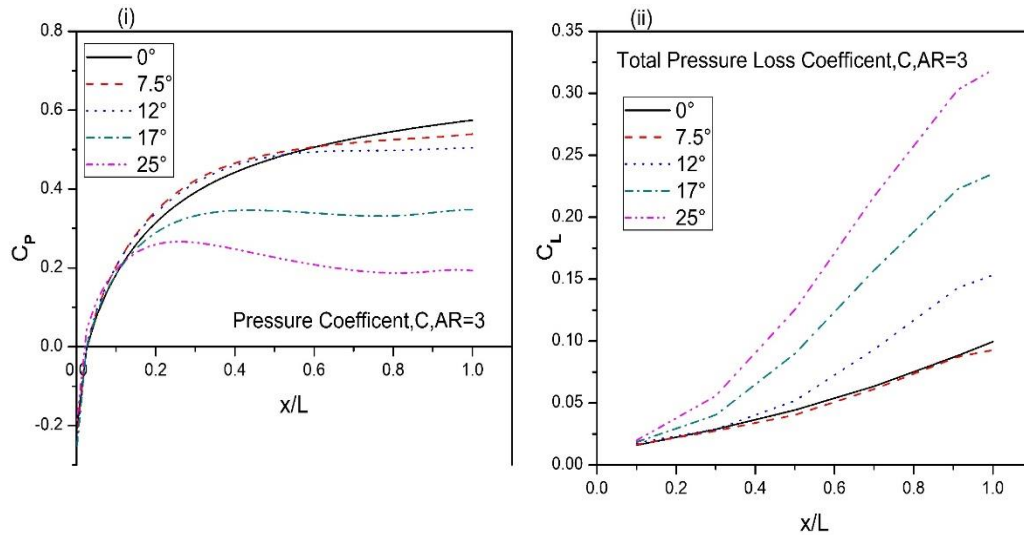


Figure 7.11: (i) Static pressure recovery coefficient at the casing wall with a cone angle of 20° ; (ii) Total pressure loss coefficient with a cone angle of 20° .

The smallest loss of the total pressure coefficient for the equivalent cone angle of 15° is up to a 7.5° swirl angle and gives an optimum performance at that angle. It also shows the minimum loss of the total pressure coefficient at a 7.5° swirl angle for a cone angle of 20° . This result implies that the optimum selection of the inlet swirl angle suppresses the flow separation by a relatively low total pressure loss. Figures 7.9 (ii), 7.10 (ii), and 7.11 (ii) show the maximum loss of total pressure coefficient at 25° swirl angle for equivalent cone angles of $10^\circ, 15^\circ,$ and 20° . Figure 7.13 (ii) depicts the C_L about the swirl angle. The high cant angle, decaying swirl intensity, and adverse pressure gradient on the walls all contribute to the maximum loss coefficient. Further, the value of the pressure lost coefficient increases due to the distorted velocity profile distribution inside the diffuser.

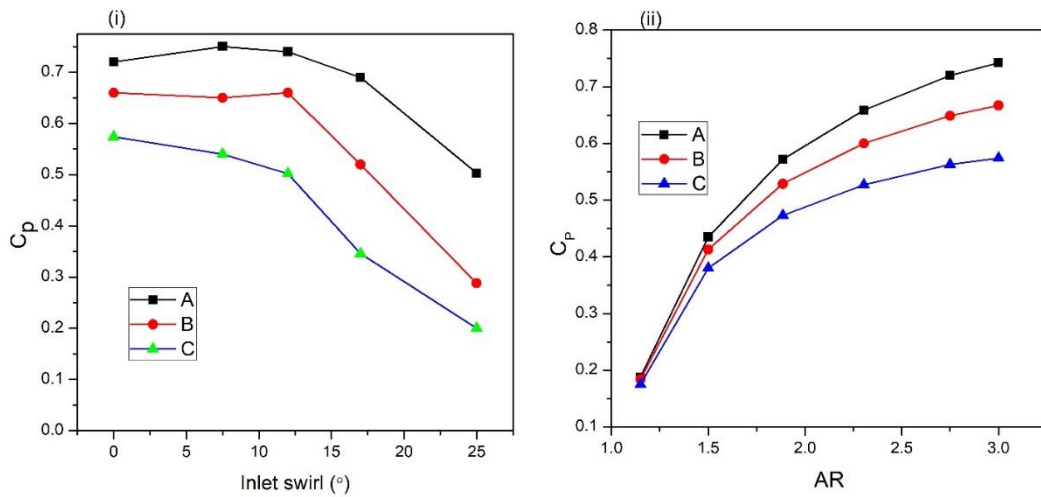


Figure 7.12: (i) Static pressure coefficient at the exit with inlet swirl of diffusers A, B, and C; (ii) Static pressure recovery coefficient (C_p) with the variation of the area ratio of diffusers A, B, and C along the length.

7.1.6 Effectiveness

The effectiveness of diffusers is the reverse of the pressure loss coefficient. The apparent data of the effectiveness is affected by the axial inlet flow, cant angle, and diffuser length. The diffuser's effectiveness is plotted about the inlet swirl angle for A, B, and C type diffusers are shown in Figure 7.13 (i).

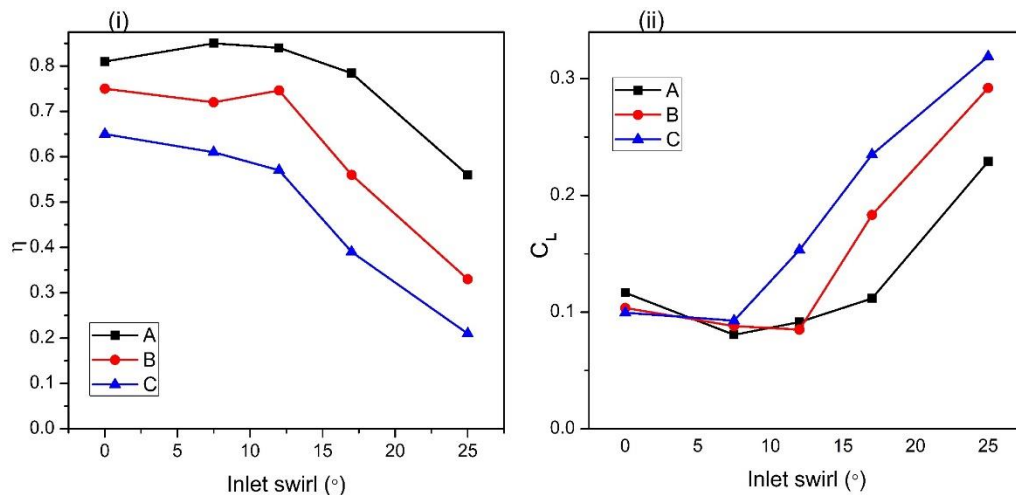


Figure 7.13: (i) Effectiveness with inlet swirl of diffuser A, B, and C; (ii) Total pressure loss coefficient with inlet swirl of diffuser A, B, and C.

The plots indicate that η decreases with an increasing equivalent cone angle for the non-swirl flow. The swirl flow effect is very significant in improving the effectiveness of

the A-type diffuser with a swirl angle of 7.5° . The diffuser's effectiveness decreases beyond the swirl angle of 12° for A-type and B-type diffusers due to the separation and reversal flow in the hub. Improvements in diffuser performance are significantly enhanced by swirling flow; there is a radial pressure gradient enhancing the momentum exchange between the mainstream and the boundary. In the C type diffuser, the η decreases by the swirling flow due to wide space availability, which promotes flow separation either from the hub or casing wall, as seen in the velocity vector contours of an equivalent cone angle of 20° .

7.2 Inlet Swirl Optimization for Flow Separation in PHDC Annular Diffuser

In this section, the computational studies were carried out on the straight hub axial annular diffuser with swirling and non-swirling flow at the inlet. The equivalent cone angle of the annular diffuser is 15° and the area ratio is 2. The computational analysis predicts the flow behavior and performance characteristics in form of streamline contours, velocity profiles, and static pressure recovery coefficient along the non-dimensional diffuser passage. The goal of this research is to determine the optimal inlet swirl angle of the annular diffuser for the best performance. Simulation for all cases is performed at $Re = 2.5 \times 10^5$. Table 7.2 shows the values of the fixed geometric parameters for the annular diffuser.

Table 7.2: Value of the geometric parameters of the annular diffuser.

$R_{hi} = 3.8 \text{ cm}, R_{ci} = 7.75 \text{ cm}, \theta_h = 0 \text{ (deg)}, AR = 2$				
Sr. No.	θ_c (deg)	L (cm)	$L/\Delta R$	θ_e (deg)
1	6.7	21.25	5.37	15

7.2.1 Streamline Contours

The streamline contours for the two-dimensional axisymmetric annular diffuser with and without swirl flow are shown in Figure 7.14.

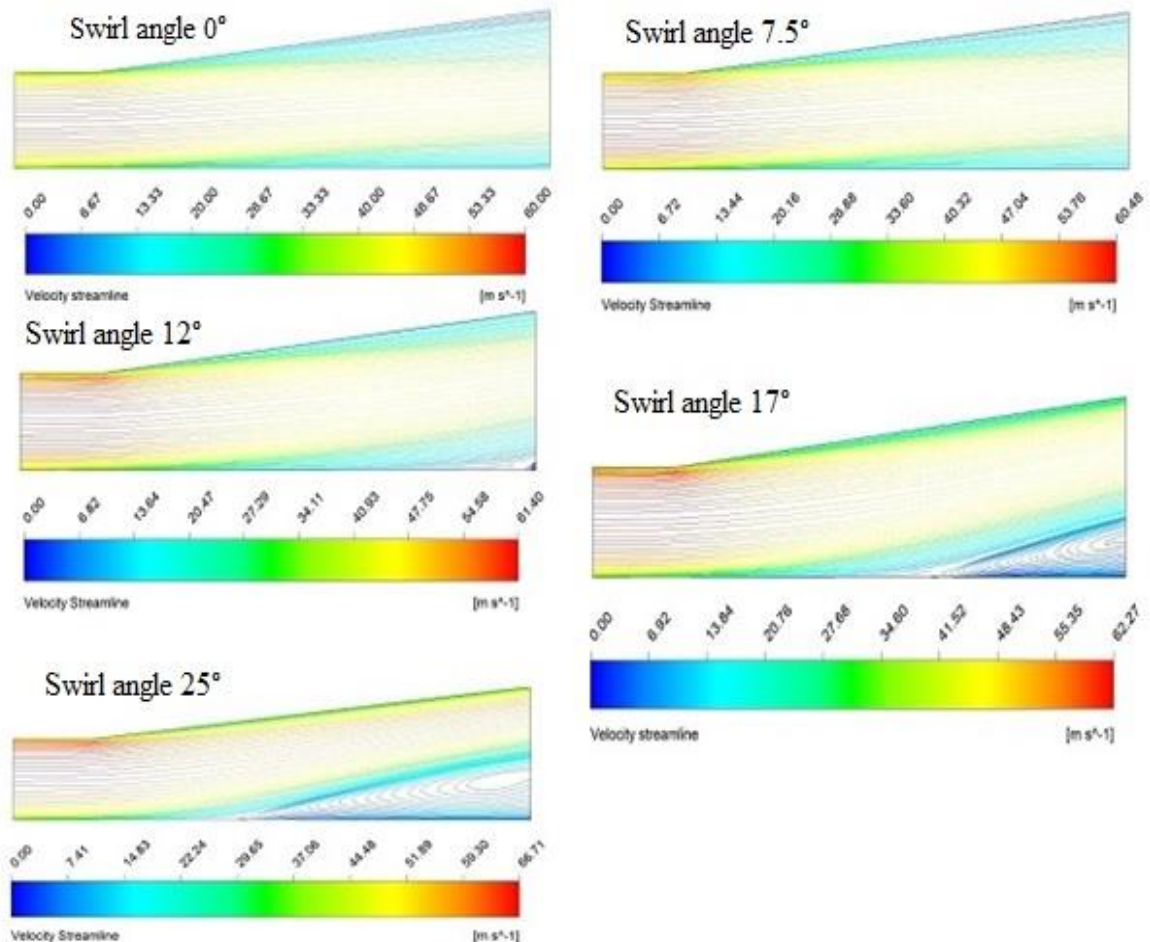


Figure 7.14: Streamline contours for the two-dimensional axisymmetric annular diffuser with and without swirl flow.

The fluid movement is visible in the diffuser's streamlined contour from the entry to the exit. The contours exhibit symmetry of flow at inlet swirl angles of (0°-12°). The separation zone exists at the swirl angles of 17° and 25° because of the adverse pressure gradient on the wall. Strong swirl flow degrades the performance by causing a separation zone at the hub wall, resulting in higher total losses and a decrease in the flow's effective area.

7.2.2 Velocity Profiles

Figures 7.15-7.16 depict the distribution of longitudinal and swirl velocity profiles for a PHDC annular diffuser with a cone angle of 15° and an area ratio of 2. The flow moves along the diffuser passage, then velocity declines at a greater rate close to the inner and outer wall as the boundary layer grows.

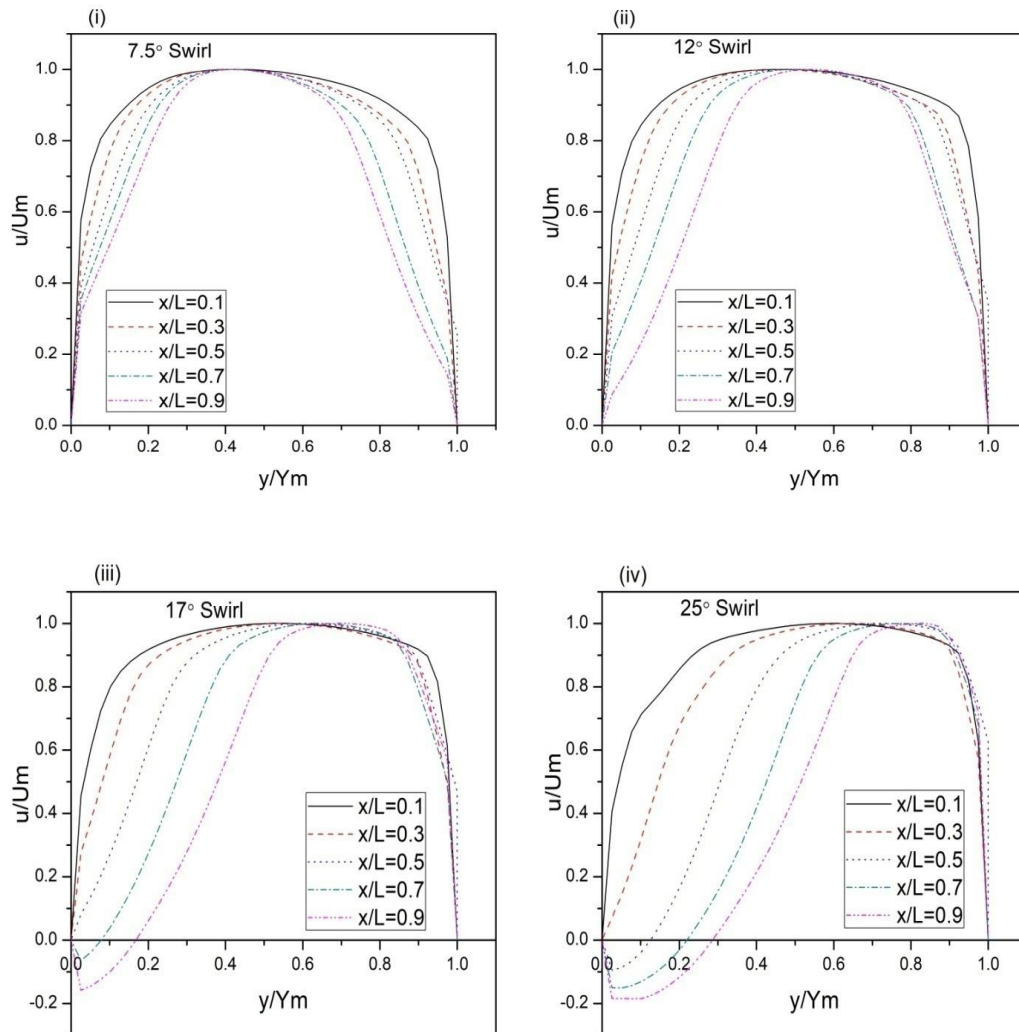


Figure 7.15: Longitudinal velocity distributions of an equivalent cone angle of 15° with inlet swirl angles (7.5° - 25°).

The growth of the boundary layer is evident from the longitudinal velocity profiles that the velocity diminishes near the hub and casing wall as the diffuser passage increases from $x/L = 0.1 - 0.9$. The highest non-dimensional velocity moves toward the inner

surface along the flow passage of the diffuser at a swirl angle of 7.5° is depicted in Figure 7.15 (i). When swirl flow is introduced at the inlet, the velocity moves toward the diffuser's outer wall. At a whirl angle of 17° , reversal flow is indicated on the inner surface up to $y/Y_m = 0.092$ and $y/Y_m = 0.18$ at the diffuser passage $x/L = 0.7$ and $x/L = 0.9$, respectively. The stall is seen at the hub wall, with the increase of swirl intensity at the inlet. The tangential component of velocity increases towards the casing as the radius of the annular cross-section increases.

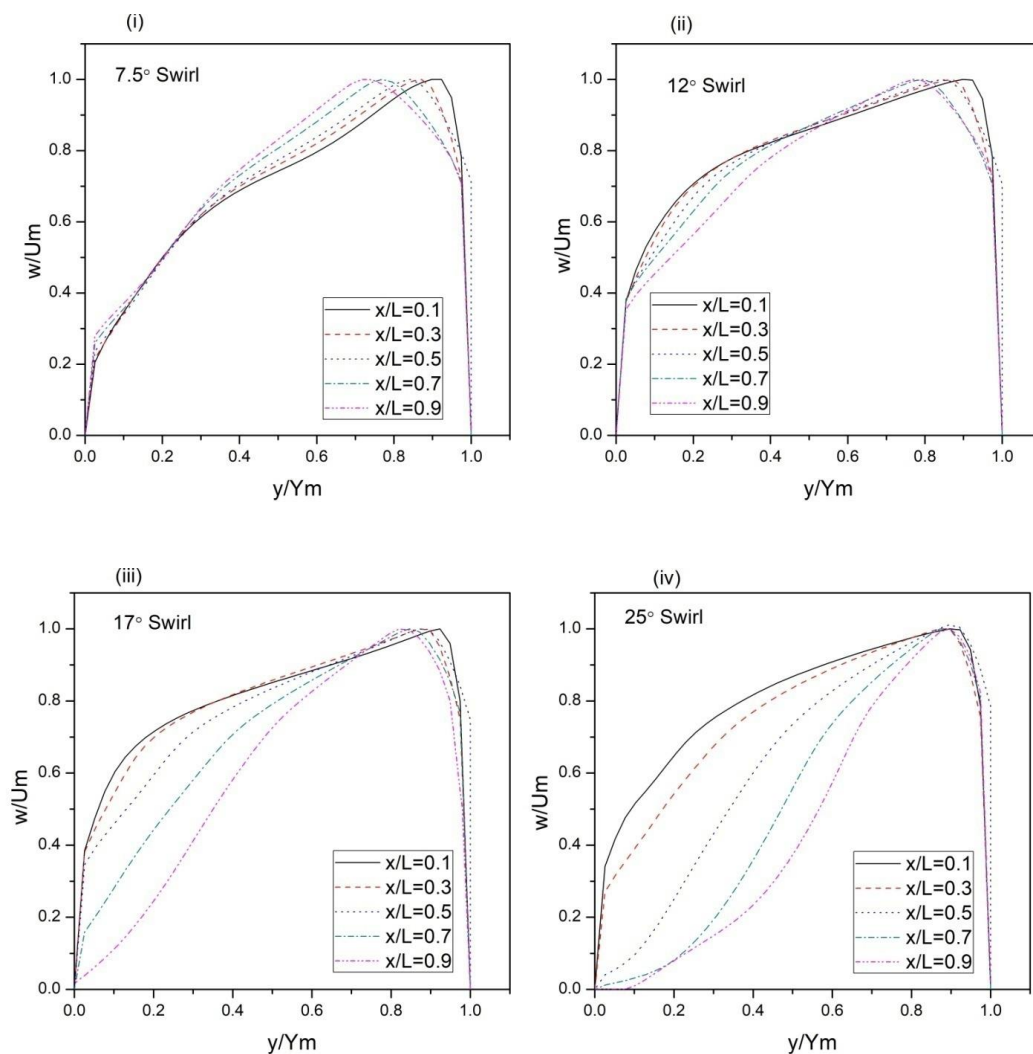


Figure 7.16: Swirl velocity distributions of an equivalent cone angle of 15° with inlet swirl angles (7.5° - 25°).

7.2.3 Static Pressure Recovery Coefficient

Figure 7.17 shows the pressure recovery coefficient (C_p) along the flow path with varied inlet swirl flow (0° - 25°) for a cone angle of 15° and $AR = 2$. The static pressure rises as the diffuser passage expands with the non-swirl flow. At a 12° inlet swirl angle, the best pressure recovery is attained. For inlet swirl angles of 17° and 25° , C_p is greatest up to diffuser passage $x/L = 0.54$ and 0.29 , respectively. The decay of swirl intensity and flow separation on the wall causes the pressure recovery coefficient to decrease after a certain length of the diffuser.

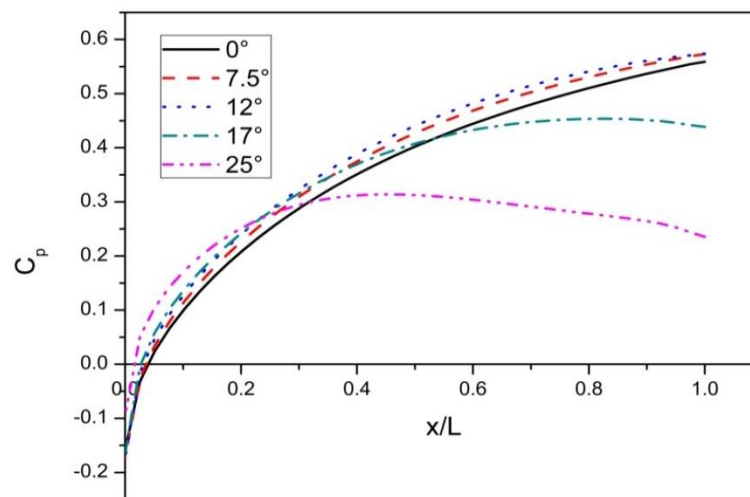


Figure 7.17: Static pressure recovery coefficient at the casing wall with an equivalent cone angle of 15° .

7.3 Effect of Swirling Flow on the Characteristics of the UHDC Annular Diffuser

This section investigated the performance characteristics of a UHDC diffuser with a casing wall angle of 9° and a hub wall angle of 5° of $AR = 3$. The fully developed turbulent flow with a swirl angle of 0° - 25° is to be chosen to generate a swirl velocity type distribution at the diffuser's inlet. The geometric value of the annular diffuser has been optimized for maximum static pressure recovery coefficient and the lowest total

pressure loss coefficient possible. The geometrical configuration specifications of the UHDC annular diffuser are listed in Table 7.3.

Table 7.3: Geometrical dimensions of the Unequal Hub and Diverging Casing (UHDC) annular diffuser.

$R_{hi} = 3.8 \text{ cm}, R_{ci} = 7.75 \text{ cm}, \theta_h = 5^\circ, AR = 3$				
Sr. No.	θ_c (deg)	L (cm)	$L/\Delta R$	θ_e (deg)
1	9	37.55	9.5	15

7.3.1 Velocity Distribution Analysis

The effects of swirling and non-swirling flows are examined in this study. Further, the effect of the recirculation zone (RZ) on performance is investigated. Figure 7.18 shows a detailed investigation of the UHDC diffusers streamline contours at swirl angles varying from 0° to 25° .

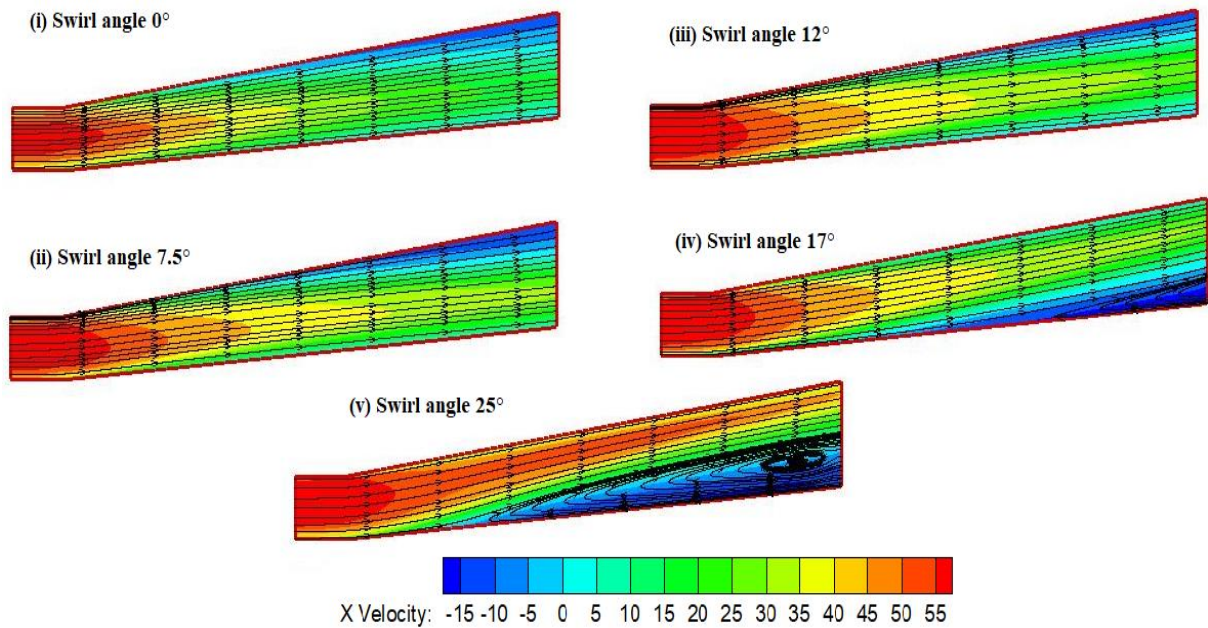


Figure 7.18: Streamline contours of UHDC diffuser at inlet swirl angles (i) 0° , (ii) 7.5° , (iii) 12° , (iv) 17° , and (v) 25° .

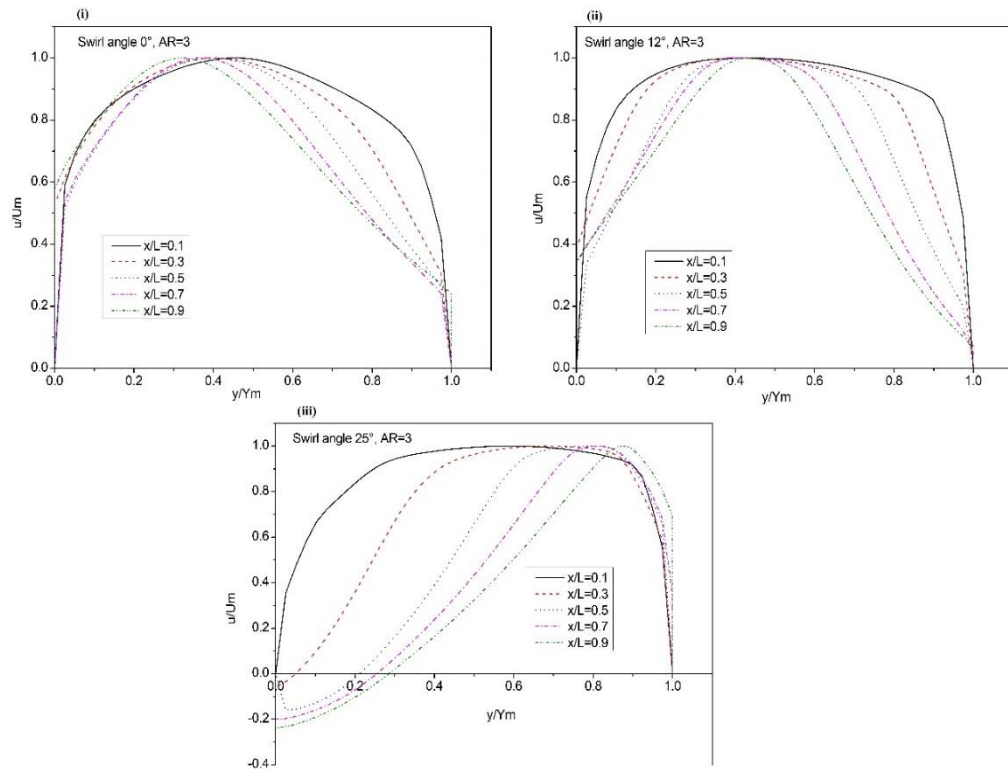


Figure 7.19: Longitudinal velocity profiles at the different axial locations of UHDC diffuser (i) Swirl angle 0° ; (ii) Swirl angle 12° ; (iii) Swirl angle 25° .

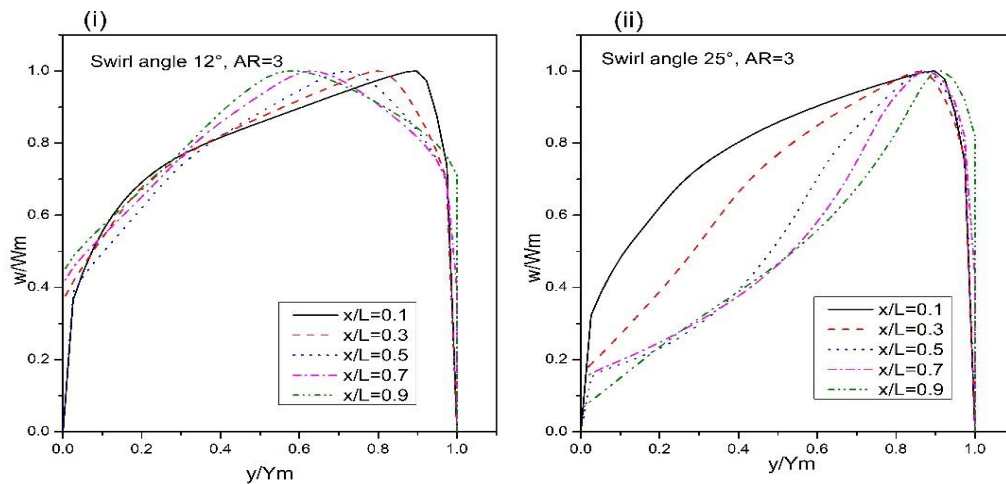


Figure 7.20: Swirl velocity profiles at the different axial locations of UHDC diffuser (i) Swirl angle 12° ; (ii) Swirl angle 25° .

The velocity profiles of the UHDC diffuser exhibit symmetry of flow between the walls at swirl angles of 0° - 12° . Due to the appropriate selection of geometrical parameters and inlet swirl angles, there is no flow reversal from the walls, as shown in Figure 7.18

(i-iii). Figure 7.19 depicts the longitudinal velocity pattern of the UHDC annular diffuser with an area ratio of 3 at swirl angles of 0° , 12° , and 25° . Diffusion occurs constantly along the length of the diffuser. Most of the fluid flows close to the hub wall at a 0° inlet swirl angle and separation occurs at a swirl angle of 25° , as seen in Figure 7.19. The reverse flow occurred on the hub surface at the inlet swirl angle of 25° for $x/L = 0.3-0.9$, respectively. The swirl velocity distribution is shown in Figure 7.20 for the inlet swirl angles of 12° - 25° . According to these plots, the swirl velocity increases towards the diffuser's casing wall. Due to the forced vortex nature, swirl velocity nearby the casing surface is greater in the case of a 25° inlet swirl. The high swirl velocity towards the casing indicates that the flow has separated from the hub. The aforementioned phenomena indicate that swirl decay occurs as the fluid moves downward direction through the diffuser.

7.3.2 Static Pressure Recovery Coefficient

The mass-weighted average pressure recovery coefficient has been determined in the annular diffuser with inlet swirl angles of 0° - 25° at the casing wall of the diffuser.

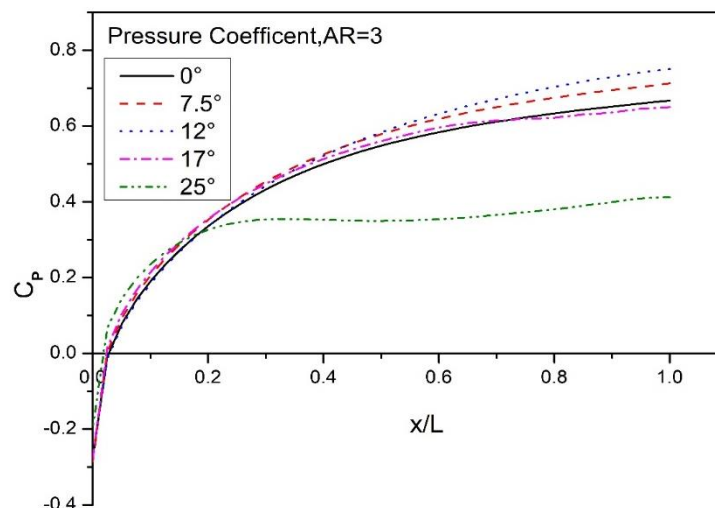


Figure 7.21: Static pressure recovery coefficient at the casing wall of the UHDC diffuser.

It is observed that static pressure rises in swirl flow as compared to without swirl flow. The maximum pressure recovery is achieved at a 12° inlet swirl angle, as shown in Figure 7.21. The strong swirl angles improve the pressure recovery up to a certain length, but afterward, they have a negative impact. The pressure recovery decreases from $x/L = 0.19$ to the exit of the diffuser passage at a swirl angle of 25° . The decrement in performance is due to the existence of a separation zone on the hub wall and the strong swirl intensity at the inlet.

7.4 Concluding Remarks

The following inferences have been highlighted from the numerical investigation of the incompressible flow through the annular diffuser having an AR of 2-3.

1. The stall is seen on the casing surface at a cone angle of 20° in non-swirl flow, but with swirl flow it vanishes and moves away from the casing wall.
2. The static pressure recovery coefficient increases along the diffuser length as the fluid flow develops downstream. The rate of increase in pressure recovery depends upon the distance from the inlet. The maximum value of C_p achieved at the exit of the diffuser are 0.75, 0.67, and 0.56 corresponding to 7.5° , 12° , and 0° swirl angles and 10° , 15° , and 20° equivalent cone angles respectively.
3. The coefficient of total pressure loss (C_L) is the lowest at the optimum swirl angle along the diffuser passage. The optimum swirl angles are 7.5° and 12° for equivalent cone angles of 10° and 15° , respectively.
4. The maximum coefficient of pressure recovery rises to 75% at a swirl angle of 7.5° of a cone angle of 10° for AR 3.
5. It is found that the highest performance is observed at a swirl angle of 12° for an equivalent cone angle of 15° and an AR of 2.

6. The UHDC diffuser's performance is degraded due to the existence of a separation zone on the hub wall at the inlet swirl angles of 17° and 25° .
7. The best performance is observed at the optimized swirl angle of 12° for the UHDC diffuser.

Chapter-8

8 Computational investigation: Performance Characteristics of Flow in Annular Diffusers

This chapter presents the computational investigation into the impact of geometrical and dynamical parameters on the performance of annular diffusers. The effect of swirl and non-swirl flow at the diffuser's inlet is an important dynamic parameter. All these studies were conducted on a fixed Reynolds number of 2.5×10^5 . The simulations were carried out on the four different configurations of the annular diffuser using the *ANSYS Fluent*. The simulated results show that increasing the swirl intensity at the diffuser's inlet improves pressure recovery at the casing surface. Swirl intensity reduces flow separation on the casing and shifts flow from the hub wall to the annulus region's casing wall. The intensity of the swirl reduces the separation of flow on the casing and shifts flow from the hub wall to the casing wall of the annulus region. The proposed annular diffuser design improves the efficiency of gas turbine engines.

8.1 Computational Domain

For all simulations, a two-dimensional axisymmetric computational domain was used, as per the geometric details of the annular diffusers listed in Table 8.1. Figure 8.1 depicts the geometrical configuration of an annular diffuser, whereas Figure 8.2 illustrates the geometrical designs of annular diffusers.

8.2 Computational Analysis of Different Types of Annular Diffuser

The flow behavior and performance characteristics of four annular diffusers with numerous inlet swirl angles were examined along their length. These are analyzed in

terms of streamline traces over velocity contours, longitudinal velocity distribution, swirl velocity distribution, static pressure recovery (C_p), and total pressure loss coefficient (C_L).

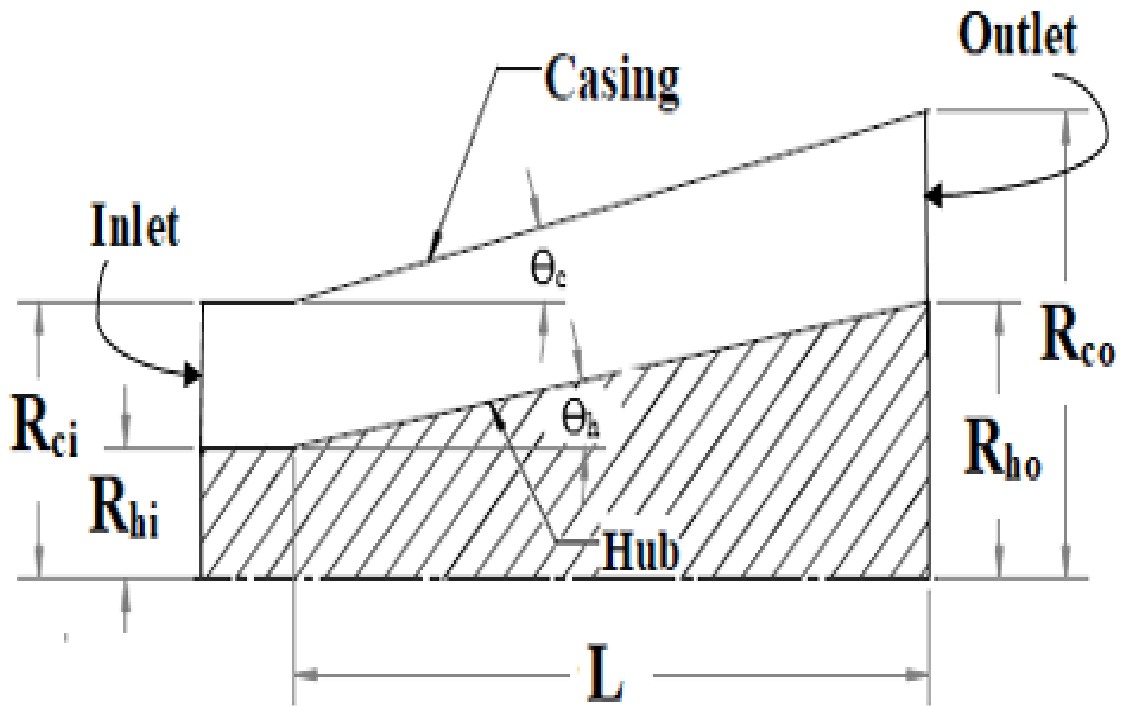


Figure 8.1: Geometrical configuration of the annular diffuser.

Table 8.1: Geometrical specifications of annular diffusers.

Diffuser types	$R_{hi} = 3.8 \text{ cm}, R_{ci} = 7.75 \text{ cm}, AR = 3,$ $L = 56.52 \text{ cm}, (R_h/R_c)_I = 0.49, L/\Delta R$ $= 14.30, \theta_e = 10^\circ$			
	R_{ho}	R_{co}	θ_h	θ_c
Equal Hub and Diverging Casing (EHDC)	15.35	19.3	11.55	11.55
Unequal Hub and Diverging Casing (UHDC)	8.75	14.61	5	6.92
Parallel Hub and Diverging Casing (PHDC)	3.8	12.30	0	4.6
Convergent Hub and Diverging Casing (CHDC)	0	11.69	-3.85	3.99

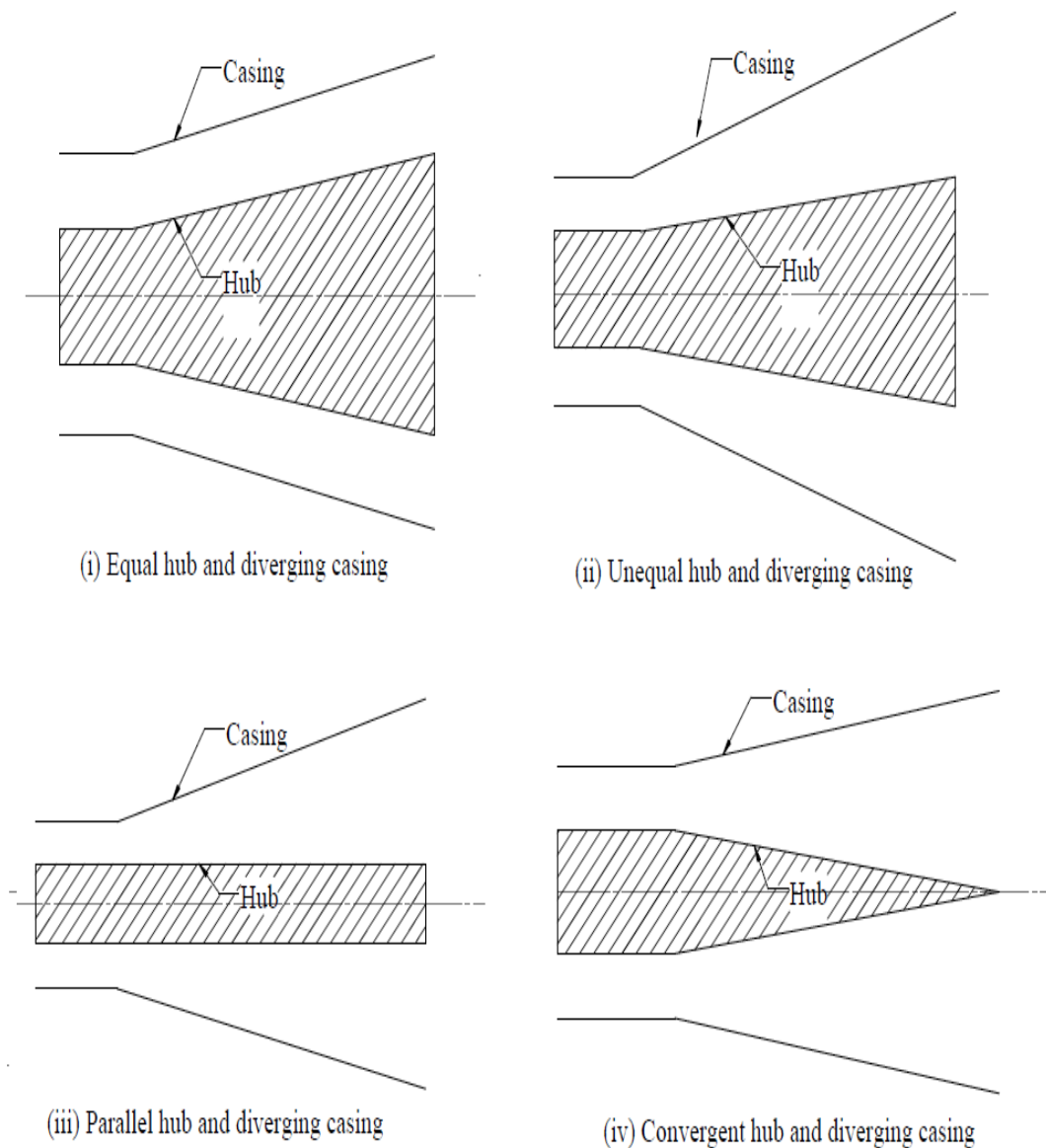


Figure 8.2: Geometrical designs of annular diffusers.

8.2.1 Streamline Traces over Velocity Contours

The analysis of streamline traces over velocity contours assists in evaluating the quality of flow direction change. However, the recirculation zone (RZ) has been seen at the annular diffuser's exit in some cases. The detailed analysis of the velocity and streamline contours of four diffusers, viz., EHDC, UHDC, PHDC, and CHDC, at swirl angles of 12° and 25° , is presented in Figure 8.3 (i) and 8.3 (ii), respectively.

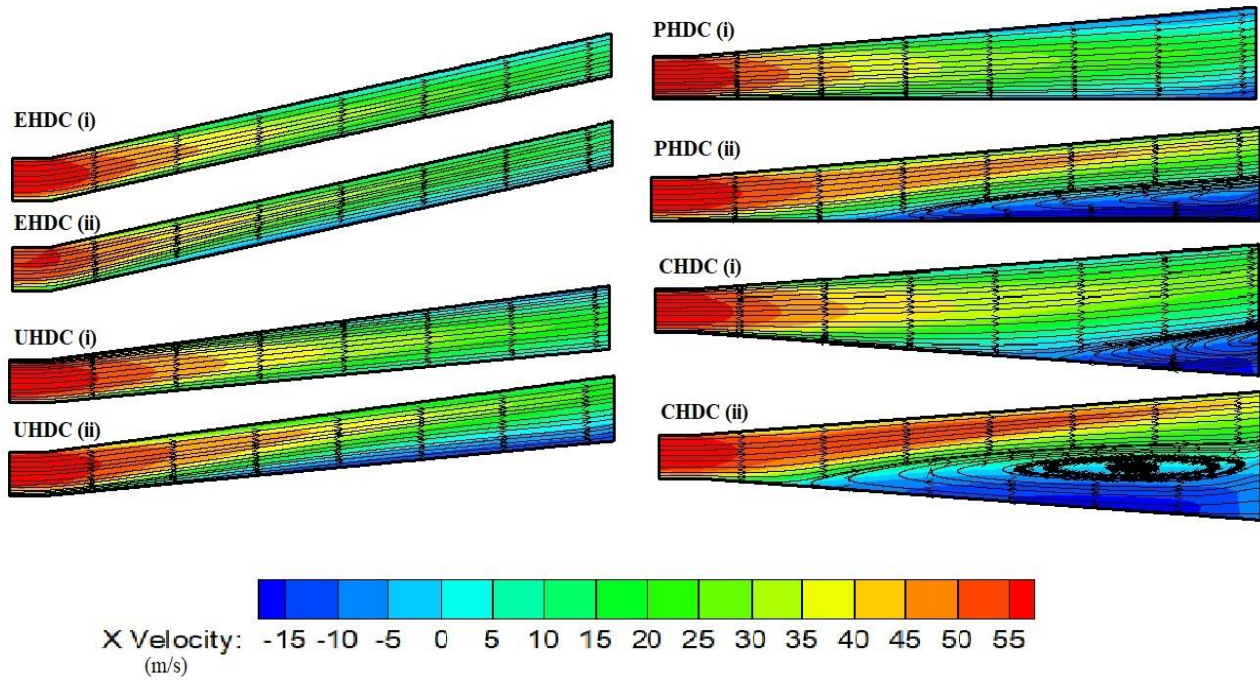


Figure 8.3: Streamline traces over velocity contours for different diffusers at inlet swirl angles (i) 12° and (ii) 25° .

The flow decelerates as it goes through the diffuser, causing the static pressure to rise continually. The velocity profiles of flow are symmetrical between the walls at a swirl angle of 12° for EHDC and UHDC diffusers. There is also no separation of flow from the walls in both cases, indicating that the geometrical specifications and swirl angles used in this investigation were adequate. In the case of PHDC diffuser geometry, there is no RZ and maximum performance is reached at a swirl angle of 12° . Further, at a swirl angle of 25° , RZ is quite extensive in the axial direction; but, RZ is less extended in the radial direction in the diffuser's two-thirds length. As a result, the amount of pressure gradients affects the shape of the RZ in velocity contours. The RZ is apparent in the CHDC diffuser case at swirl angles of 12° and 25° due to the gradual geometry variation. The RZ is observed along the hub wall at a swirl angle of 12° at one-third of the diffuser length, as shown in Figure 8.3. (i). The large RZ is seen in the axial and radial directions along the hub wall at a 25° inlet swirl angle.

As a result, the RZ's strength and size grow as the inlet swirl angle increases, resulting in a shift in flow separation position and negative velocity towards the hub wall. The flow distribution of velocity contours with swirl flow is attributed to the effect of centrifugal force. The flow is pressed against the diffuser's casing wall by centrifugal force, which promotes flow stabilization and intensifies the tendency for flow separation from the hub wall. There is an increase in angular momentum and a subsequent decrease in turbulence at the curvature and streamline curvature radius, respectively, due to the establishment of a reverse flow region across the inner wall. From the above study, it is concluded that there is a variation in the streamline flow in the PHDC diffuser at a swirl angle of 25° and the CHDC diffuser at swirl angles of 12° and 25° .

8.2.2 Velocity profiles

The flow pattern occurring at the annular region's exit is investigated using longitudinal and swirl velocity profiles in four different geometrical designs of annular diffusers. The effect of inlet swirl angles on velocity profiles has been investigated in this section. The research reveals whether RZ exists at diffuser exits and its significance. Figure 8.4 (i) shows the longitudinal velocity profiles with inlet swirl angles of 0° to 25° of EHDC and UHDC diffusers. Peak velocity is close to the hub wall in the EHDC diffuser at 0° swirl angle but moves towards the casing wall as the swirl angle increases. Figure 8.4 (ii) shows the swirl velocity profile with swirl angles of 7.5° to 25° for EHDC and UHDC diffusers. The swirl velocity profile in the EHDC diffuser shows the forced vortex nature of the flow, and maximum diffusion is close to the diffuser's casing wall.

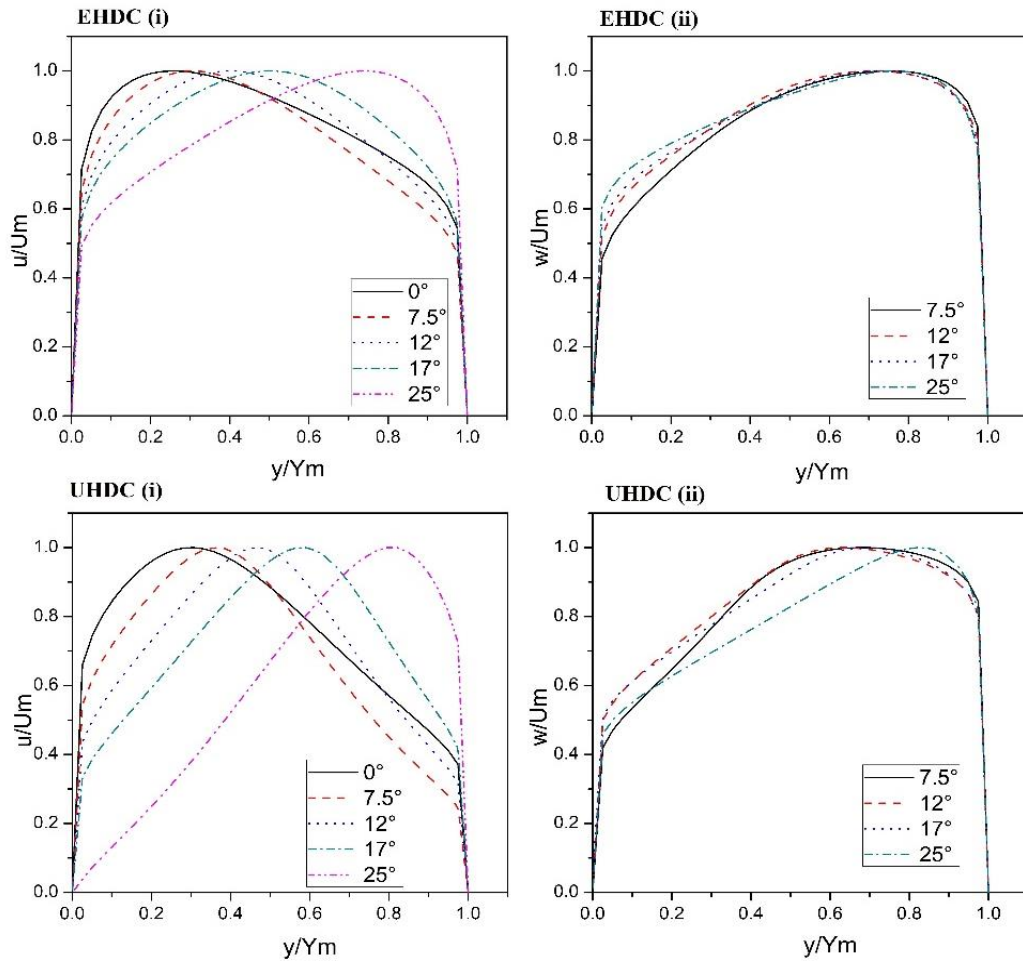


Figure 8.4: (i) Longitudinal velocity profiles at the exit of EHDC and UHDC diffusers; (ii) swirl velocity profiles at the exit of EHDC and UHDC diffusers.

The UHDC diffuser has higher flow diffusion because the hub and casing wall have a lower divergence angle than the EHDC diffuser. At swirl angles of 12° to 17° , the bulk of the fluid flow occurs between the inner and the outer walls. At a swirl angle of 25° , the velocity profile changes abruptly, indicating that the bulk of the fluid has accumulated near the casing wall. Figures 8.5 (i) and 8.5 (ii) illustrate the longitudinal velocity and swirl velocity profiles of PHDC and CHDC diffusers, respectively. The negative magnitude of the velocity profile is observed in the PHDC diffuser from the hub to radial heights of $y/Y_m = 0.15$ and $y/Y_m = 0.31$ for swirl angles of 17° and 25° , respectively. The flow is pushed towards the outer surface by centrifugal force, and

thus the RZ exists at the beginning of the stream due to the availability of more annular space.

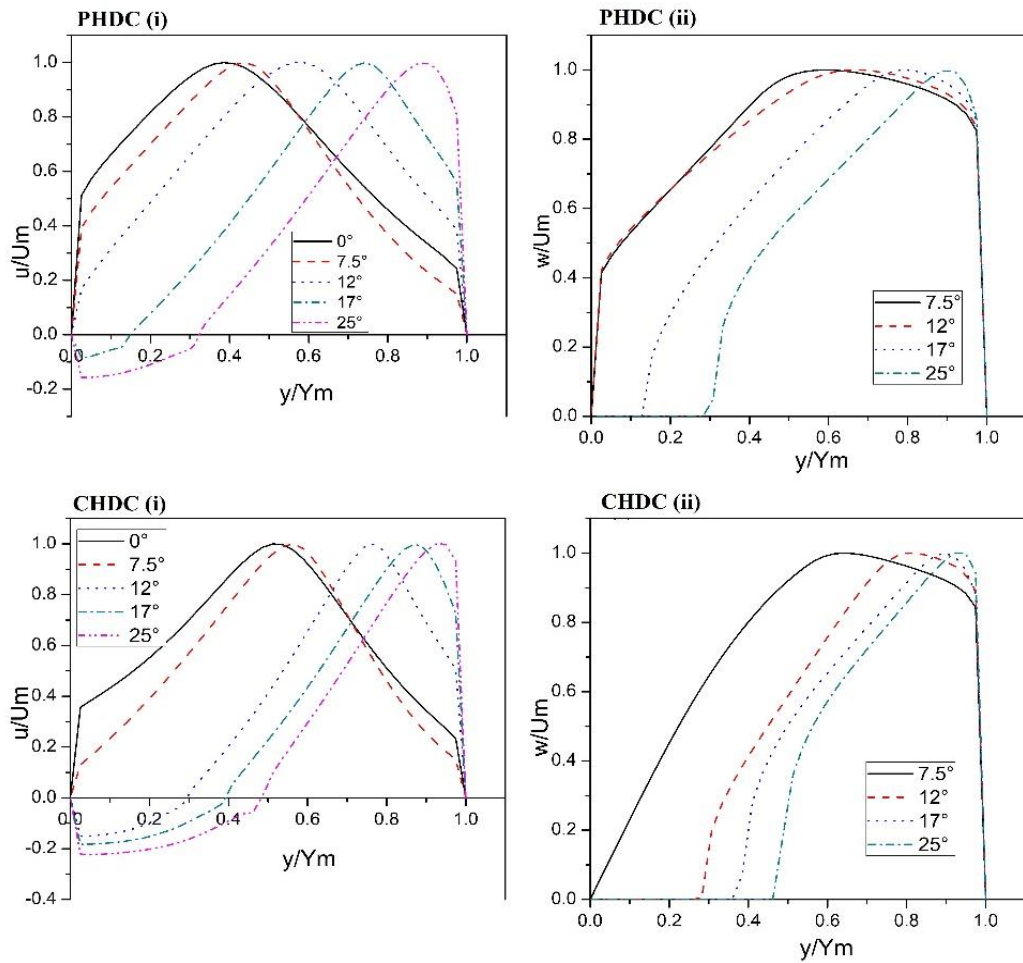


Figure 8.5: (i) Longitudinal velocity profiles at the exit of PHDC and CHDC diffusers; (ii) swirl velocity profiles at the exit of PHDC and CHDC diffusers.

The swirl velocity profile also reveals flow separation at 17° and 25° swirl angles. Due to the forced vortex nature, the remaining velocity profile follows the same patterns as the previous situations. Due to the negative hub wall angle in the CHDC diffuser, the RZ exists at the hub wall at swirl angles of 12° to 25° , and the swirl pushes the flow towards the outer surface, which is the same as observed in the PHDC diffuser. Figure 8.5 (ii) depicts the reversal of flow at swirl angles of 12° to 25° in the swirl velocity profile distribution. The flow reversal is caused by an increase in swirl velocity and the forced vortex phenomenon.

The velocity profile distribution shows the formation of the swirl flow component by the centrifugal force, which energizes the casing wall region and delays the boundary layer separation. The other imperative feature is that the enrichment of flow in the casing surface area results in a flow drop in the core region. The stabilized longitudinal velocity profile of EHDC, UHDC, PHDC, and CHDC diffusers is observed at swirl angles of 17° , 12° , 12° , and 0° , respectively.

8.2.3 Static Pressure Recovery Coefficient

The amount of static pressure recovered in four different geometric models of annular diffusers with equivalent cone angles of 10° and area ratios of 3 for swirling and non-swirling flow were studied quantitatively. Figure 8.6 depicts the pressure recovery graphs for the EHDC, UHDC, PHDC, and CHDC diffusers. When swirl flow in diffusers is compared to non-swirl flow, pressure recovery is found to be slightly higher in swirl flow. With a swirl angle of 0° to 17° , the pressure coefficient variation along the casing wall increases continually in the EHDC diffuser. At a 17° swirl angle, there is a significant improvement in pressure recovery. In comparison to non-swirl flow, pressure recovery reduces after the distance $x/L = 0.4$ to the diffuser exit with a 25° swirl angle. The trends in pressure recovery of the UHDC diffuser are similar to that of the EHDC diffuser as the growth in pressure recovery continues from 0° to 17° swirl angle. A sudden fall in C_p is observed for the 25° swirl angle after $x/L = 0.32$ due to the sharp change in the velocity profile. In the PHDC diffuser, the pressure recovery coefficient improves from 0° to 12° swirl angles, but when the whirl angle increases further, the pressure recovery decreases, as illustrated in Figure 8.6. For 17° to 25° swirl angles, there is a drop in C_p due to RZ's existence at the hub wall. The maximum improvement in C_p is observed for swirl angles of 7.5° , 12° , 17° , and 25° as compared to non-swirl flow is up to $x/L = 0.64$, 0.72 , 0.28 , and 0.16 , respectively, for the CHDC

diffuser. The performance then degrades due to the flow separation and the presence of the RZ at the hub wall. In a CHDC diffuser with no swirl conditions, the best performance is observed.

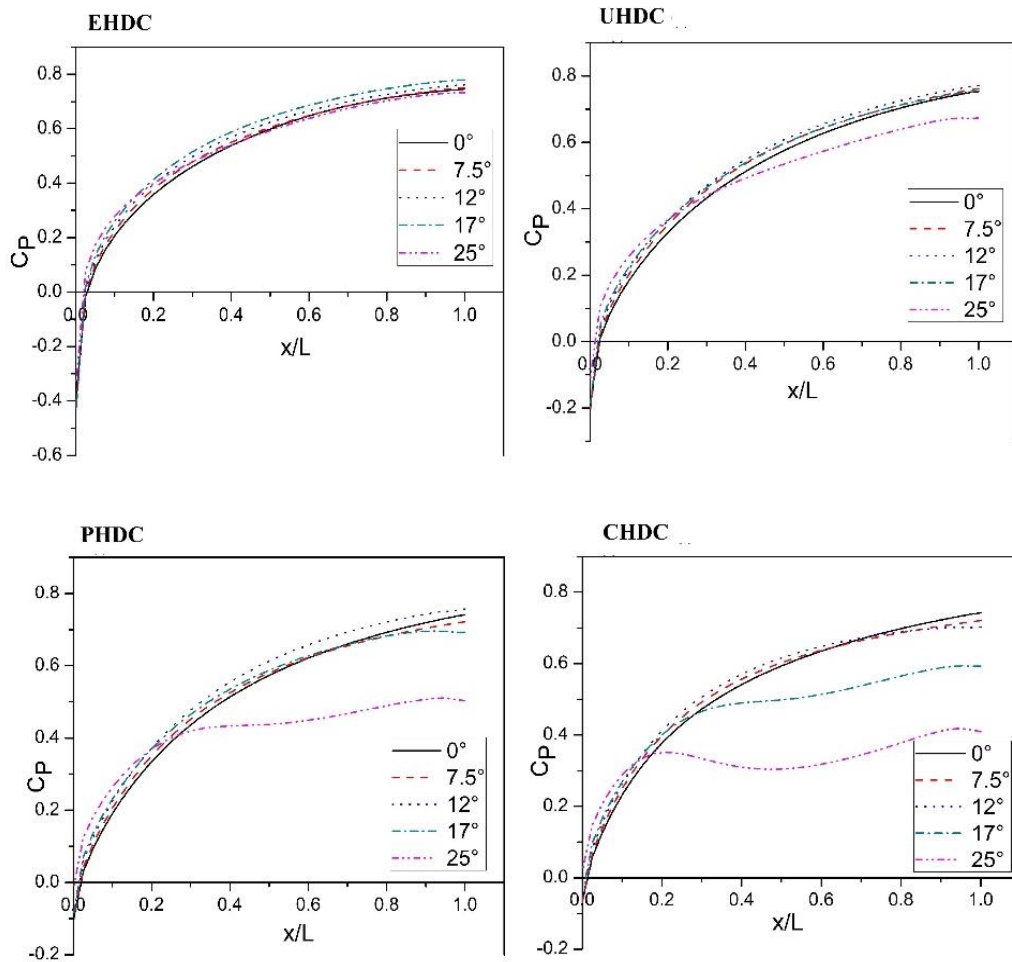


Figure 8.6: Pressure recovery coefficient at the casing wall of EHDC, UHDC, PHDC, and CHDC diffusers.

The highest pressure recovery is attained in the EHDC diffuser at a 17° swirl angle and no separation of the fluid flow from the walls, according to the observations of pressure recovery on the casing wall. The EHDC diffuser has a higher percentage of pressure recovery ($C_p = 0.76$), which corresponds with Coladipietro et al (1975). They discovered that when diffusers have a lower equivalent cone angle, the swirl effect is more pronounced. The most insufficient pressure recovery is attributed to a higher inlet

swirl angle in the diffusers, resulting in more growth of the boundary layer and a high adverse pressure gradient on the wall. When swirl flow is compared to non-swirling flow, a maximum of 5% pressure recovery improvement is observed during analysis. The diffuser's best performance is expected based on the geometric design and the choice of the optimum swirl angle.

8.2.4 Total Pressure Loss Coefficient

The variation of C_L is evaluated with swirl and non-swirl flow of EHDC, UHDC, PHDC, and CHDC diffusers as shown in Figure 8.7. With the diffuser's axial length, the C_L gradually increases. The maximum loss coefficient is observed at a swirl angle of 25° due to the high swirl intensity and bulk fluid accumulation on the casing wall in EHDC and UHDC diffusers. Due to the presence of uniform fluid flow between the hub and casing wall, pressure loss at swirl angles ranging from 7.5° to 17° in EHDC and UHDC diffusers is less than non-swirl flow. These findings suggest that the optimal swirl angle selection leads to impressive swirl intensity suppression with minimal pressure loss. The loss coefficient in PHDC and CHDC diffusers is maximum at a swirl angle of 25° due to distorted velocity distribution and the separation of flow on the hub surface. The instability of flow and reversal of stream can lead to an increment in the C_L along the longitudinal length. The minimum C_L values are 12, 11.15, 10.23, and 9 percent at 17° , 12° , 12° , and 7.5° swirl angles for EHDC, UHDC, PHDC, and CHDC diffusers, respectively. The loss coefficient value is much more dependent upon the casing wall angle and the inlet swirl angle. The least value of the C_L gives the stable value of static pressure distribution and shows no presence of RZ at the annulus region's inner wall.

The performance comparison of the four shaped annular diffusers with swirl and non-swirl flow of the C_p and C_L coefficient are shown in Figures 8.6 and 8.7,

respectively. The maximum performance $C_p = 0.76$ and $C_L = 0.12$ is achieved in the EHDC diffuser with an inlet swirl angle of 17° . The UHDC and PHDC diffusers perform best when the inlet swirl angle is 12° and there is no flow separation. The maximum performance of $C_p = 0.73$ and $C_L = 0.09$ are observed at a 0° inlet swirl angle in the CHDC diffuser.

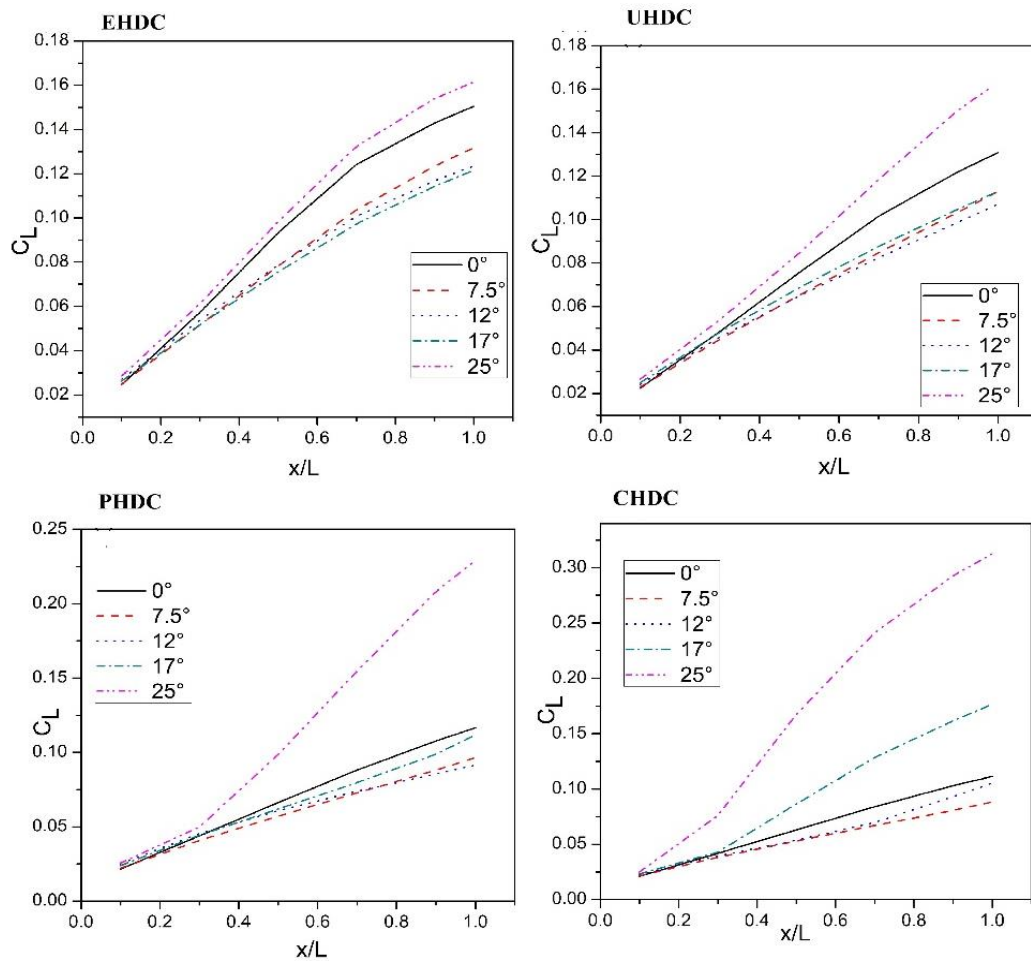


Figure 8.7: Total pressure loss coefficient of the EHDC, UHDC, PHDC, and CHDC diffusers.

8.3 Concluding Remarks

The numerical studies were performed on four different types of annular diffusers, all of which had the same cone angle of 10° , axial length ($L = 56.52$ cm), and area ratio

($AR = 3$). The significant conclusions which have been made about the annular diffusers are summarized below.

1. It is observed that EHDC and UHDC diffusers show the best performance at swirl angles of 17° and 12° respectively. Moreover, no recirculation zone (RZ) is found on the walls at a swirl angle of 25° in the EHDC and UHDC diffusers.
2. The findings of the PHDC diffuser show maximum pressure recovery achievement at a swirl angle of 12° . However, its performance declined at the inlet swirl angles of 17° and 25° due to the recirculation zone (RZ) on the hub wall.
3. The outcomes obtained through the CHDC diffuser show the worse effect of swirl flow between swirl angles of 12° to 25° , which is demonstrated by the non-dimensional velocity distribution at the diffuser's exit.
4. It is found that the EHDC diffuser shows the best performance and minimum pressure loss coefficient at a swirl angle of 17° .

Chapter-9

9 Conclusion and Scope for Future Work

The current research was performed to investigate the flow through annular diffusers with and without inlet swirl flow. Experimental and numerical studies were conducted with a variety of inlet conditions and geometric configurations. From this study, it is apparent that defining the optimum parameters such as geometry design, area ratio (AR), wall angle, inlet velocity profile, inlet Reynolds number, inlet swirl, experimental and computational studies with respect to velocity profiles, static pressure recovery coefficient (C_p), total pressure loss coefficient (C_L), and effectiveness (η) are fairly well established for two-dimensional annular diffusers. The broad conclusions which can be drawn as a result of the present analysis, along with the scope for future work, are presented.

9.1 Conclusion

1. Non-dimensional longitudinal and swirl velocity profiles have been computed at various heights along the diffuser length with swirling and non-swirling flow. Whether the flow is swirling or non-swirling, the velocity profile continuously decreases on the downstream side from the diffuser's inlet.
3. The shape of the velocity profiles is changed due to the swirl flow and the boundary layer development in the velocity profile has a very distinct shape.
4. The longitudinal velocity profile is not symmetrical about the center at any cross-section of the diffusers. Non-swirl flow accumulates at the hub wall and is moved towards the outer wall by an inlet swirl flow.

5. The swirl improves the performance of diffusers at particular swirl intensities for different geometries of the diffuser. It also shows that performance decreases with an increase in cone angle.
5. It is observed that the inlet swirl flow shifts the main flow from the inner surface to the outer surface of the diffuser, due to which no stall is present on the outer surface.
6. It is found that inlet swirl flow rises the C_p up to a certain length; thereafter, the performance is degraded due to the existence of a separation zone on the walls.
7. The C_p increases across the diffuser passage as the fluid flow develops downstream; the rate of increase in pressure recovery depends upon the distance from the inlet.
8. Diffuser performance is enhanced with the introduction of the inlet swirl. The core flow is moved from the hub surface to the diffuser's casing surface, and no reversal flow is observed on the casing surface.
9. The effect of area ratios on the longitudinal velocity profiles reveals that as the AR increases, the peak velocity profile is moved toward the hub side, and flow separation occurs on the casing side.
10. In the non-swirl flow, it is found that there is no reversal of flow and no separation of flow on the hub surface in the case of a parallel hub diverging casing annular diffuser.
11. The highest C_p is observed as high as 0.76 of the area ratio 3 at the 12° inlet swirl angle for a cone angle of 15° .

12. The C_p increases initially at the 25° inlet swirl angle, then decreases due to flow separation on the diffuser's casing wall.
13. The effectiveness of the diffuser and the total pressure loss coefficient value increase as the area ratio increases for a given equivalent cone angle and degree of inlet swirl.
14. The highest values of the static pressure recovery coefficient and the diffuser's effectiveness are observed at the optimum value of the inlet swirl angle.
15. The numerical results of the simulations reasonably agree with the experimental results.

9.2 Scope for Future Work

The current research work has been carried out with and without inlet swirl flow of various geometric configurations. Future research work may be carried out in the following areas:

1. The diffuser's performance can also be intensified by introducing a strut at the hub wall of the annular diffuser.
2. The diffuser's geometrical parameters are area ratios and cone angle that show the overall diffusion across the length. Further, it can be extended to vary these parameters and the curved wall of the diffuser.
3. The current work for the annular diffuser is carried out on incompressible subsonic flow only. There is scope to investigate annular diffuser performance using compressible flow, sonic flow, and hypersonic flow.
4. The current problem solves the uniform velocity profile at the diffuser's inlet. But in actual practical conditions, the velocity profile is not uniform. For further study, it is an excellent area of interest.

5. The current research work was performed on the stationary walls of the annular diffuser. The additional work can be done on the rotating walls of the annular diffuser.
6. There is a scope to expand the current study to entropy generation for the different shapes of the annular diffuser geometry and area ratios.

Bibliography

Abdalla H. A., Mayit M. M. El, Hamid A. A. Abd El and Shazly A. M. El. (2006). study of swirling turbulent flow and heat transfer characteristics in conical diffusers. *Eighth International Congress of Fluid Dynamics & Propulsion*, Egypt.

Adenubi, S. O. (1976). Performance and flow regime of annular diffusers with axial turbomachine discharge inlet conditions. *Journal of Fluids Engineering*, 98(2), 236-242.

Adkins, R. C. (1975). A short diffuser with low-pressure loss. *Journal of Fluids Engineering*, 97(3), 297-302.

Adkins, R. C., & Wardle, M. H. (1990, June). A method for the design of optimum annular diffusers of canted configuration. In *ASME 1990 International Gas Turbine and Aeroengine Congress and Exposition* (pp. V003T06A015-V003T06A015). American Society of Mechanical Engineers.

Al-Mudhafar, M. M., Ilyas, M., & Bhinder, F. S. (1982, April). Investigation of flows in rectangular diffusers with inlet flow distortion. In *ASME 1982 International Gas Turbine Conference and Exhibit* (pp. V001T01A025-V001T01A025). American Society of Mechanical Engineers.

Applied Fluid Dynamics Handbook by R.D. Blevins (1984).

Armfield, S. W., Cho, N. H., & Fletcher, C. A. (1990). Prediction of turbulence quantities for swirling flow in conical diffusers. *AIAA Journal*, 28(3), 453-460.

Arora, B.B. (2007). Aerodynamic analysis of diffuser, PhD thesis. Delhi: DU.

Arora, B. B. (2014). Performance analysis of parallel hub diverging casing axial annular diffuser with 20 equivalent cone angle. *Australian Journal of Mechanical Engineering*, 12(2), 179-194.

Arora, B. B., & Pathak, B. D. (2009). Effect of geometry on the performance of annular diffuser. *Int. J. Appl. Eng. Res.*, 4(12), 2639-2652.

Arora, B. B., & Pathak, B. D. (2011). CFD analysis of axial annular diffuser with both hub and casing diverging at unequal angles. *International Journal of Dynamics of Fluids*, 7(1), 109-122.

Azad, R. S. (1996). Turbulent flow in a conical diffuser: A review. *Experimental Thermal and Fluid Science*, 13(4), 318-337.

Barbosa, D. L., Vaz, J. R., Figueiredo, S. W., SILVA, M. D. O. E., Lins, E. F., & Mesquita, A. L. (2015). An investigation of a mathematical model for the internal velocity profile of conical diffusers applied to DAWTs. *Anais da Academia Brasileira de Ciências*, 87(2), 1133-1148.

Bryer, D. W., & Pankhurst, R. C. (1971). Pressure-probe methods for determining wind speed and flow direction. HM Stationery Office.

Bryer, D., Walshe, D., & Garner, H. (1955). Pressure probes selected for three-dimensional flow measurement.

Cerantola, D. J., & Birk, A. M. (2015). Experimental validation of numerically optimized short annular diffusers. *Journal of Engineering for Gas Turbines and Power*, 137(5), 052604.

Cerantola, D. J., & Birk, A. M. (2015). Investigation of Tabs in Short Annular Diffusers with Swirling Flow. *Journal of Engineering for Gas Turbines and Power*, 137(9), 092601.

- Cho, N. H., & Fletcher, C. A. J. (1991). Computation of turbulent conical diffuser flows using a non-orthogonal grid system. *Computers & Fluids*, 19(3-4), 347-361.
- Chong, T. P., Joseph, P. F., & Davies, P. O. A. L. (2008). A parametric study of passive flow control for a short, high area ratio 90deg curved diffuser. *Journal of Fluids Engineering*, 130(11), 111104.
- Clausen, P. D., Koh, S. G., & Wood, D. H. (1993). Measurements of a swirling turbulent boundary layer developing in a conical diffuser. *Experimental Thermal and Fluid Science*, 6(1), 39-48.
- Coladipietro, R., Schneider, J. H., & Sridhar, K. (1975). Effects of inlet flow conditions on the performance of equiangular annular diffusers. *Transactions of the Canadian Society for Mechanical Engineering*, 3(2), 75-82.
- Coladipietro, R. M. (1974). Effect of inlet swirl and wall layer thickness on the performance of equiangular annular diffusers.
- Crane, C. M., & Burley, D. M. (1974). Numerical studies for viscous swirling flow through annular diffusers. *Journal of Engineering Mathematics*, 8(3), 193-207.
- Dau, K., McLeod, M., & Surry, D. (1968). Two probes for the measurement of the complete velocity vector in subsonic flow. *The Aeronautical Journal*, 72(696), 1066-1068.
- Dean Jr, R. C., & Runstadler Jr, P. W. (1969). Straight channel diffuser performance at high inlet Mach numbers. *Journal of Fluids Engineering*, 91(3), 397-412 .
- Dellenback, P. A., Metzger, D. E., & Neitzel, G. (1988). Measurements in turbulent swirling flow through an abrupt axisymmetric expansion. *AIAA Journal*, 26(6), 669-681.

Dominy, R. G., Kirkham, D. A., & Smith, A. D. (1998). Flow development through interturbine diffusers. *Journal of turbomachinery*, 120(2), 298-304.

Duggins, R. K. (1970). The Performance of Conical Diffusers Discharging through Tailpipes: A continuation of earlier work on conical diffuser performance instigated by Cockrell and Markland at Nottingham University. *Aircraft Engineering and Aerospace Technology*, 42(8), 28-32.

Dunn JJ, Ricklick M, Kapat JS. (2009). Flow characterization of a three-dimensional separated annular diffuser. *In ASME International Mechanical Engineering Congress and Exposition 2009 Jan 1* (Vol. 43826, pp. 859-865).

El-Askary, W. A., Ibrahim, K. A., El-Behery, S. M., Hamed, M. H., & Al-Agha, M. S. (2015). Performance of vertical diffusers carrying Gas-solid flow: experimental and numerical studies. *Powder Technology*, 273, 19-32.

Fluent user's guide (2014). (Fluent Inc., USA).

Fox, R. W., & McDonald, A. T. (1966). An experimental investigation of incompressible flow in the conical diffuser. *Int. d. Mech. Sci. Pergamon Press Ltd.*,8,125-139.

Fox, R. W., & McDonald, A. T. (1971). Effects of swirling inlet flow on pressure recovery in conical diffusers. *AIAA Journal*, 9(10), 2014-2018.

Fox, R.W., & Kline, S.J. (1962). Flow Regimes in Curves Subsonic Diffuser, *Trans ASME. Journal of Basic Engineering*, 84(3), 303-316.

Ganesan, V. (1980). Flow and boundary layer development in straight core annular diffusers. *International Journal of Engineering Science*, 18(2), 287-304.

- Gartner, J., & Amitay, M. (2016). Vortex generator's effectiveness compared to active flow control techniques in a transonic diffuser. In the *8th AIAA Flow Control Conference* (pp. 3770).
- Ghose, P., Datta, A., & Mukhopadhyay, A. (2013). Effect of dome shape on static pressure recovery in a dump diffuser at different inlet swirl. *Int. J. Emerging Technol. Adv. Eng*, 3(3), 465-471.
- Goebel, J. H., & Japikse, D. (1981). The Performance of an Annular Diffuser Subject to Various Inlet Blockage and Rotor Discharge Effects. *Consortium Final Report, Creare TN-325*.
- Gorman, J. M., Sparrow, E. M., Abraham, J. P., & Minkowycz, W. J. (2016). Evaluation of the efficacy of turbulence models for swirling flows and the effect of turbulence intensity on heat transfer. *Numerical Heat Transfer, Part B: Fundamentals*, 70(6), 485-502.
- Gupta, A., Lilley, D., Syred, N., 1984. Swirl Flows. Abacus Press, New York.
- Hah, C. (1983). Calculation of various diffuser flows with inlet swirl and inlet distortion effects. *AIAA Journal*, 21(8), 1127-1133.
- Hoadley, D., (1970). Three-dimensional turbulent boundary layers in an annular diffuser (Doctoral dissertation, University of Cambridge).
- Japikse, D. (2002, July). Correlation of annular diffuser performance with geometry, swirl, and blockage. In *Proceedings of the 11th NASA/OSU Thermal and Fluids Analysis Workshop* (pp. 107-118).
- Japikse, D., & Pampreen, R. (1979). Annular diffuser performance for an automotive gas turbine. *Journal of Engineering for Power*, 101(3), 358-372.

- Ji-jun, Y., Zhao-gang, Y., & Ming-de, W. (1992). On the throughflow with swirling inflow in the annular diffuser. *Applied Mathematics and Mechanics*, 13(3), 241-254.
- Johnston, I. H. (1953). The effect of inlet conditions on the flow in annular diffusers. *National Gas Turbine Establishment Farnborough (United Kingdom)*.
- Kanemoto Toshiaki, Toyokuri Tomitaro and Kurokawa Junichi, (1982). Flow in the annular diffuser. *Bulletin of JSME*, 25(204).
- Kanemoto, T., & Toyokura, T. (1983). Flow in Annular Diffusers: 2nd Report, Flow Analysis, and Effect of Inlet Boundary Layer Thickness. *Bulletin of JSME*, 26(218), 1323-1329.
- Keerthana, R., & Jamuna Rani, G. (2012). Flow analysis of annular diffusers. *International Journal of Engineering Research and Applications (IJERA)*, 2(3), 2348-2351.
- Kibicho Karanja and Sayers Anthony. (2008). Experimental Measurements of the Mean Flow Field in Wide-Angled Diffusers: A Data Bank Contribution. *International Journal of Mechanical, Aerospace, Industrial, Mechatronic and Manufacturing Engineering*, Vol: 2, No: 7.
- Kline, A. (1981). Effects of inlet conditions on conical-diffuser performance. *Journal of Fluids Engineering*, 103(2), 250-257.
- Kline, S. J., Abbott, D. E., & Fox, R. W. (1959). Optimum design of straight-walled diffusers. *Journal of Basic Engineering*, 81(3), 321-329.
- Kochevsky, A. N. (2001). Numerical investigation of swirling flow in Annular Diffusers with a rotating hub installed at the exit of hydraulic machines. *Journal of fluids engineering*, 123(3), 484-489.

- Kumar, D. S. (1977). *Effect of swirl on flow through annular diffusers* (Doctoral dissertation).
- Kumar, D. S., & Kumar, K. L. (1980). Effect of swirl on pressure recovery in annular diffusers. *Journal of Mechanical Engineering Science*, 22(6), 305-313.
- Kumar, M., Arora, B. B., Maji, S., & Maji, S. (2011). Effect of inlet swirl on the flow behavior inside the annular diffuser. *International Journal of Dynamics of Fluids*, 7(2), 181-188.
- Kumar, M., Arora, B., Maji, S., & Maji, S. (2012). Effect of area ratio and inlet swirl on the performance of annular diffuser. *International Journal of Applied Engineering Research*, 7(13), 1493-1506.
- Kurokawa, J., Imamura, H., & Choi, Y. D. (2010). Effect of j-Groove on the Suppression of Swirl Flow in a Conical Diffuser. *Journal of Fluids Engineering*, 132(7), 071101.
- Lipeng, Lu., Zhong, Luyang and Yangwei, Liu, (2016). *Turbulence model assessment for separated flows in a rectangular asymmetric three-dimensional diffuser*. Emerald Insight, 33(4).
- Little B. H., JR. and Wilbur Stafford W.,(1950). Performance area ratio and boundary-layer data from 12° and 23° conical diffusers 2.0 at Mach numbers up to choking and Reynolds numbers up to 7.5×10^6 , *National advisory committee for aeronautics*.
- Livesey, J.L. and Odukewe, A.O., (1973).Some effects of pipe flow generated entry conditions on the performance of straight walled conical diffusers with high subsonic entry Mach number. *Israel Journal of Technology*, 11(4), 217-222.

- Lo, K. P., Elkins, C. J., & Eaton, J. K. (2012). Separation control in a conical diffuser with an annular inlet: center body wake separation. *Experiments in Fluids*, 53(5), 1317-1326.
- Lohmann, R. P., Markowski, S. J., & Brookman, E. T. (1979). Swirling flow through annular diffusers with conical walls. *Journal of Fluids Engineering*, 101(2), 224-229.
- Mansour N. N., Kim J., and Moin P. (1987). Near-Wall k-e Turbulence Modelling. *AIAA Journal*, 27(8), 1068-1073.
- Marsan, A., Trébinjac, I., Coste, S., & Leroy, G. (2015). Influence of unsteadiness on the control of a hub-corner separation within a radial vaned diffuser. *Journal of Turbomachinery*, 137(2), 021008.
- McMillan O.J and Johnston J. P.(1973).Performance of Low-Aspect-Ratio Diffusers with fully Developed Turbulent Inlet Flows Part 1-Some Experimental Results. *Journal of Fluids Engineering*, 95(3), 385-392.
- Mehta, R. D. (1979). The aerodynamic design of blower tunnels with wide-angle diffusers. *Progress in Aerospace Sciences*, 18, 59-120.
- Mohan, R., Singh, S. N., & Agrawal, D. P. (1998). Optimum inlet swirl for annular diffuser performance using CFD. *IJEMS*, 5(1), 15-21.
- Moller, P. S. (1966). A radial diffuser using incompressible flow between narrowly spaced disks. *Journal of Basic Engineering*, 88(1), 155-162.
- Narayana, A., Chandrasekhara, N. V., & Chithambaran, V. K. (1984). Turbulence characteristics of a plane diffuser flow with inlet velocity distortion. *Indian Institute of Science Journal*, 65, 57-70.

- Nordin, N., Karim, A., Ambri, Z., Othman, S., & Raghavan, V. R. (2015). Effect of varying inflow Reynolds number on pressure recovery and flow uniformity of 3-D turning diffuser. In *Applied Mechanics and Materials*, 699, 422-428.
- Nordin, N., Karim, Z. A. A., Othman, S., Raghavan, V. R., Batcha, M. F. M., Hariri, A., & Basharie, S. M. (2017, April). Flow characteristics of 3-D turning diffuser using particle image velocimetry. In *AIP Conference Proceedings* (Vol. 1831, No. 1, pp. 020021). AIP Publishing.
- Noui-Mehidi, M. N., Wu, J., & Sutalo, I. (2004, December). Velocity distribution in an asymmetric diffuser with perforated plates. In *Proceedings of 15th Australasian Fluid Mechanics Conference, the University of Sydney, Australia* (pp. 13-17).
- Obi, S., Aoki, K., & Masuda, S. (1993). Experimental and computational study of turbulent separating flow in an asymmetric plane diffuser. In *the Ninth Symposium on Turbulent Shear Flows, Hyoto, Japan* (vol. 305).
- Padilla, A. M., Elkins, C. J., & Eaton, J. K. (2011). The effect of inlet distortion on 3D annular diffusers. In *TSFP Digital Library Online*. Begel House Inc.
- Perry, J. H. (1974). Calibration and Comparison of Cobra Probe and Hot Wire Anemometer for Flow Measurements in Turbomachinery. *Commonwealth Scientific and Industrial Research Organization*.
- Prakash, R., Karthiek, N., Ashwath, P., Anand, H., & Adithya, G. (2016). Numerical Study on a Conical Diffuser with Inlet Swirl. In *Applied Mechanics and Materials* (Vol. 852, pp. 688-692). Trans Tech Publications.
- Pramod B A, Gowda B Sadashive, (2014). *3D flow analysis of an annular diffuser with and without struts*. International journal of mechanical engineering and technology, 5(9), 222-231.

- Redha Wahidi Semih M. Ölçmen Wing Lai, (2015). Volumetric three component measurement of air jet flow of different diffuser designs. *53rd AIAA Aerospace Sciences Meeting*.
- Reneau, L. R., Johnston, J. P., & Kline, S. J. (1967). Performance and design of straight, two-dimensional diffusers. *Journal of Basic Engineering*, 89(1), 141-150.
- Sajben, M., KROUTIL, J., SEDRICK, A., & HOFFMAN, G. (1974). Experiment on conical diffusers with distorted inflow. In *7th Fluid and Plasma Dynamics Conference* (pp. 529).
- Salim, B. (2013). Effect of geometrical parameters on the performance of wide-angle diffusers. *Int. J. Innov. Res. Sci. Eng. Technol*, 2, 4178-4191.
- Selvakar thick, C., Ajith, S., Nagaraju Doddi, H., Sanal Kumar, V. R., Rangaraj, V., & Allen, J. K. (2016). Parametrical Optimization of a three-dimensional Dump Diffuser with Aerodynamically-shaped Flame Tube for Modern Aircraft Engines. In *52nd AIAA/SAE/ASEE Joint Propulsion Conference* (pp. 5009).
- Senoo, Y., & Nishi, M. (1977). Prediction of flow separation in a diffuser by a boundary layer calculation. *Journal of Fluids Engineering*, 99(2), 379-386.
- Senoo, Y., Kawaguchi, N., & Nagata, T. (1978). Swirl flow in conical diffusers. *Bulletin of JSME*, 21(151), 112-119.
- Sharan, V.K., (1976). Factors influencing the performance of a diffuser. *Indian journal of technology*, 14(2), 63-66.
- Sheeba, A., & Ganesan, V. (2005). Modelling of Annular Prediffuser for Marine Gas Turbine Combustor using CFD-A Study on the Effect of Strut Configuration. *Journal of Naval Architecture and Marine Engineering*, 2(2), 41-52.

- Shimizu, Y., Nagafusa, M., & Kuzuhara, S. (1982). Effects of approaching flow types on the performances of straight conical diffusers. *Bulletin of JSME*, 25(208), 1506-1512.
- Singh, H., & Arora, B. B. (2019). Effect of Area Ratio on Flow Separation in Annular Diffuser. In *Advances in Fluid and Thermal Engineering* (pp. 297-305). Springer, Singapore.
- Singh, S. N., Agrawal, D. P., Sapre, R. N., & Malhotra, R. C. (1994). Effect of inlet swirl on the performance of wide-angled annular diffusers, *IJEMS*, 01(2), 63-69.
- Singh, S. N., Seshadri, V., Saha, K., Vempati, K. K., & Bharani, S. (2006). Effect of inlet swirl on the performance of annular diffusers having the same equivalent cone angle. *Proceedings of the Institution of Mechanical Engineers, Part G: Journal of Aerospace Engineering*, 220(2), 129-143.
- Sovran, G. (1967). Experimentally Determined Optimum Geometries for Rectilinear Diffusers with Rectangular, Conical or Annular Cross Section. *Fluid mechanics of internal flow*, 270-319.
- Sovran, G., & Cocanower, A. B. (1967). Discussion: "A Performance Prediction Method for Unstalled, Two-Dimensional Diffusers"(Reneau, LR, and Johnston, JP, 1967, ASME J. Basic Eng., 89, pp. 643–652). *Journal of Basic Engineering*, 89(3), 652-654.
- Sparrow, E. M., Abraham, J. P., & Minkowycz, W. J. (2009). Flow separation in a diverging conical duct: Effect of Reynolds number and divergence angle. *International Journal of Heat and Mass Transfer*, 52(13-14), 3079-3083.

- Stevens, S. J. (1967, September). Paper 16: The Performance of Annular Diffusers. In *Proceedings of the Institution of Mechanical Engineers, Conference Proceedings* (Vol. 182, No. 4, pp. 58-70). Sage UK: London, England: SAGE Publications.
- Stevens, S. J., & Fry, P. (1973). Measurements of the boundary-layer growth in annular diffusers. *Journal of Aircraft*, 10(2), 73-80.
- Stevens, S. J., & Williams, G. J. (1980). The influence of inlet conditions on the performance of annular diffusers. *Journal of Fluids Engineering*, 102(3), 357-363.
- Tyler, R. A., & Williamson, R. G. (1973). Conical diffusers with inflow distortion: Estimated peak local velocity at exit. *National Research Council of Canada*.
- Tyler, R.A. and Williamson, R.G., (1968). Diffuser performance with the distorted flow. *Proceedings Institution of Mechanical Engineers* 182(3D), 115-125.
- Van Dewoestine, R. V., & Fox, R. W. (1966). An experimental investigation on the effect of subsonic inlet Mach number on the performance of conical diffusers (No. FMTR-66-1). Purdue Research Foundation Lafayette In.
- Vassiliev, V., Irmisch, S., & Florjancic, S. (2002, January). CFD analysis of industrial gas turbine exhausts diffusers. In *ASME Turbo Expo 2002: Power for Land, Sea, and Air* (pp. 995-1013). American Society of Mechanical Engineers.
- Vlahostergios, Z., & Yakinthos, K. (2015). Modelling the Flow in a Transonic Diffuser with One Reynolds-Stress and Two Eddy-Viscosity Models. *Flow, Turbulence and Combustion*, 94(3), 619-642.

Waitman, B. A., Reneau, L. R., & Kline, S. J. (1961). Effects of inlet conditions on the performance of two-dimensional subsonic diffusers. *Journal of Basic Engineering*, 83(3), 349-360.

Walker, A. D., Denman, P. A., & McGuirk, J. J. (2003, January). Experimental and computational study of hybrid diffusers for gas turbine combustors. In *ASME Turbo Expo 2003, collocated with the 2003 International Joint Power Generation Conference* (pp. 311-320). American Society of Mechanical Engineers.

Wen, C., Cao, X., Yang, Y., & Li, W. (2012). Numerical simulation of natural gas flows in diffusers for supersonic separators. *Energy*, 37(1), 195-200.

Yongsen He, Kobayashi Toshio, and Morinishi Youhei. (1992). Numerical prediction of turbulent flow in a conical diffuser using k- ϵ model. *Acta Mechanica Sinica*, 8(2), 117-126.

Publications from Current Work

Based on the present study, the following papers has been published/communicated:

Journal Papers

1. Singh H, Arora BB. Effects of casing angle on the performance of parallel hub axial annular diffuser. *International Journal of Turbo & Jet-Engines*. 2020 Aug 19.
2. Singh H, Arora BB. Performance characteristics of flow in annular diffuser using CFD. *International Journal of Turbo & Jet-Engines*. 2021 Feb 15.
3. Singh H, Arora BB. Effect of swirl flow on the performance of parallel hub axial annular diffuser. *Journal of Engineering Research (JER)*.
4. Singh H, Arora BB. Effects of inlet conditions on diffuser performance. *International journal*. 2019; 9 (5):813-32.

Conferences

1. Singh H, Arora BB. Effect of area ratio on flow separation in annular diffuser. In *Advances in fluid and thermal engineering 2019* (pp. 297-305). Springer, Singapore.
2. Singh H, Arora BB. Optimization of Inlet Swirl for Flow Separation in Annular Diffuser. In *Advances in Electromechanical Technologies 2021* (pp. 409-419). Springer, Singapore.
3. Singh H, Arora BB. Effect of swirl flow on characteristics of the annular diffuser. In *international conference on cutting edge in mechanical engineering (CEME-2020)*.

Brief Bio-Data of the Author

Name Hardial Singh

Date of Birth 01/11/1984

Academic Background:

B.Tech (Mechanical Engineering): 2005-2008 Chaudhary Devi Lal
Memorial Government
Engineering College,
Panniwala Mota, Sirsa,
Haryana.

M.Tech (Machine Design): 2009-2011 National Institute of
Technology, Kurukshetra,
Haryana.

Experience:

Assistant Professor 2011-2012 Ganga Institute of
Technology and
Management, Kablana,
Jhajjar.

Assistant Professor 2012-Till date Amity University
Gurgaon, Haryana

Field of Interest:

Annular Diffusers, CFD, Stress Analysis, FEM

Research Papers/Conferences:

Journal Papers: 10

Conferences: 5